

CALCULATION OF THE EFFICIENCY OF PWM
INVERTER-FED INDUCTION MOTOR DRIVES

by

Roy Geoffrey Cann B.Sc.(Eng.)

Thesis submitted to the University of London
for the degree of Doctor of Philosophy

Department of Electrical Engineering
Imperial College of Science and Technology

August 1983

ABSTRACT

This thesis describes the development of a simple model for pulse width modulated (PWM) inverter-fed induction motor drives. Several PWM strategies are compared on the basis of overall drive efficiency.

Chapter Two presents the derivation of a model for a dc chopper. The circuit semiconductors are represented by a forward resistance in series with a reverse connected voltage source. This simple representation, together with detailed knowledge of the circuit waveforms, enables accurate prediction of the chopper power losses. The inverter model is then realised using the dc chopper as the basic building block.

The induction motor model is developed in Chapter Three. It employs the standard equivalent circuit of an induction motor, with superposition of time harmonics but neglecting space harmonics. The motor used in the experimental work has closed rotor slots and exhibits saturation effects which necessitate extending the model to include saturation characteristics for the magnetising and rotor leakage inductances.

In Chapter Four, the inverter and motor models are combined to enable drive system power losses, and consequently the system efficiency, to be calculated.

All the theoretical work is verified experimentally using a commercially designed PWM inverter drive system. In addition the motor model is verified for operation from a 50 Hz sine wave supply.

In Chapter Five, the system model is used to compare four of the most common PWM switching strategies on the basis of system efficiency, for varying numbers of commutations per cycle.

ACKNOWLEDGEMENTS

I would like to thank my supervisor, Dr S Williamson, for his constant interest and encouragement throughout the project. I would also like to extend my gratitude to all members of the academic and technical staff at Imperial College who advised or assisted me in any way. Special thanks are extended to Dr B Williams and Mr R B Owen. Finally, I wish to thank the Science and Engineering Research Council for their financial support.

CONTENTS

	<u>Page</u>
ABSTRACT	2
ACKNOWLEDGEMENTS	3
LIST OF SYMBOLS	7
CHAPTER ONE: <u>INTRODUCTION</u>	14
CHAPTER TWO: <u>DEVELOPMENT OF THE INVERTER MODEL</u>	19
2.1 Choice of Modelling Technique	19
2.2 Analysis of the DC Chopper	22
2.2.1 Calculating the Time Integrals	24
2.2.2 Conduction Loss Calculations	27
2.2.3 Switching Loss Calculations	34
2.3 Experimental Verification of the DC Chopper Simulation	34
2.4 Analysis of the Three Phase Inverter	39
2.4.1 Power Losses due to Commutation	51
2.4.2 Power Losses due to Forward Conduction	51
2.5 Experimental Verification of the Three Phase Inverter Simulation	54
2.6 Discussion on Device Switching Losses	55
CHAPTER THREE: <u>DEVELOPMENT OF THE INDUCTION MOTOR MODEL</u>	59
3.1 Introduction	59
3.2 Induction Motor Modelling Techniques	59
3.2.1 Analysis using a Generalised Machine	59
3.3.2 Analysis using Equivalent Circuits	63
3.2.3 Choice of Modelling Technique	67

	<u>Page</u>
3.3 The Induction Motor Equivalent Circuit	69
3.3.1 Test Motor Details	69
3.3.2 Magnetising Inductance	69
3.3.3 Iron Loss Resistance	72
3.3.4 Stator Resistance	74
3.3.5 Stator Leakage Inductance	74
3.3.6 Rotor Resistance	77
3.3.7 Rotor Leakage Inductance	78
3.3.8 Effect of Rotor Skew	83
3.4 Use of the Equivalent Circuit	84
3.5 Experimental Verification of the Equivalent Circuit on a Sinusoidal Supply	84
CHAPTER FOUR: DEVELOPMENT OF THE SYSTEM MODEL	93
4.1 Introduction	93
4.2 Simulating the Induction Motor Operating from the Three Phase Inverter	93
4.2.1 Number of Harmonics Considered	93
4.2.2 Non-linear Effects	94
4.2.3 Calculation of the Motor Line Current	98
4.2.4 Calculation of the Motor Power Losses	100
4.3 Experimental Verification of the Motor Simulation for Operation from the Three Phase Inverter	101
4.4 Development of the System Model	108
4.5 Experimental Verification of the System Model	109
CHAPTER FIVE: COMPARISON OF PWM SWITCHING STRATEGIES	115
5.1 Introduction	115
5.2 The Chosen PWM Switching Strategies	115

	<u>Page</u>
5.2.1 Analogue-generated PWM Switching Strategies	116
5.2.2 Digitally-generated PWM Switching Strategies	118
5.3 Comparison of Strategies	119
5.3.1 Comparison of PWM Strategies for the 4 kW Drive	122
(i) analogue-generated strategies	130
(ii) digitally-generated strategies	131
5.3.2 Comparison of PWM Strategies for the 30 kW Drive	134
5.4 Discussion and Conclusions on Chapter 5	141
CHAPTER SIX: <u>CONCLUSIONS AND RECOMMENDATIONS FOR FURTHER WORK</u>	143
CHAPTER SEVEN: <u>REFERENCES</u>	146
CHAPTER EIGHT: <u>APPENDICES</u>	153
8.1 Fourier Analysis of a Generalised 3-Level Waveform	153
8.2 Derivation of Parameters for Rotor Slot Top Leakage Inductance Calculations	155
8.3 Calculation of PWM Strategy Switching Angles	157
8.3.1 Duty Ratio Modulation	157
8.3.2 Naturally Sampled Modulation	159
8.3.3 Harmonic Elimination	162
8.3.4 Distortion Minimisation	168
8.4 Simulating the 30 kW Drive	172
8.4.1 Simulating the 30 kW Inverter	173
8.4.2 Simulating the 30 kW Induction Motor	173
(i) Calculation of Rotor Resistance and Rotor Leakage Inductance	173

LIST OF SYMBOLS

a_n	area of rotor slot bridge at n^{th} section
A_n	magnetic potential at n^{th} section of rotor slot bridge
A_N	average magnetic potential of n^{th} strip
a_s	area of rotor slot
A_S	rotor slot m.m.f.
A_{SN}	average magnetic potential of n^{th} strip on the rotor slot centre line
a_y	area of rotor slot below height y
B	flux density
B_n	flux density at the n^{th} section of rotor slot bridge
B_0	flux density at the rotor slot bridge centre line
C	capacitance
C_{SA}, C_{SM}	auxiliary and main thyristor snubber capacitors
d	rotor slot depth
d	mean diameter of airgap
DD	voltage clamping diode
DF	flywheel diode
$D1$	commutation path diode
$D2$	anti-parallel diode
f	friction coefficient
f	frequency
f_c	carrier frequency
f_H	harmonic frequency

f_R	reference frequency
f_{sn}	n^{th} time harmonic frequency
F_{GN}	average m.m.f. across the n^{th} strip airgap length
F_{SN}	average m.m.f. across the n^{th} strip slot top length
g'	Carter'd airgap length
H	magnetic field strength
H_n	magnetising force at n^{th} section of rotor slot bridge
H_N	average magnetising force in n^{th} strip
i	time varying current
i_A, i_B, i_C	stator phase currents
i_c	commutation capacitor current
i_d, i_q, i_D, i_Q	d,q axis rotor and stator currents
i_{line}	line current
i_L	load current
i_m	magnetising current
i_n	n^{th} time harmonic current
i_{phase}	phase current
i_B, i_R, i_Y	load phase currents
i_1	equivalent circuit stator current
i_2	equivalent circuit referred rotor current
I_{bar}	rotor bar current
\hat{I}_n	n^{th} time harmonic peak current
\bar{I}_n	n^{th} time harmonic rms complex current
I_0	initial current
I_1	final current
I_0	summation of rms current harmonics

[it]	time integral of current
[i ² t]	time integral of current squared
j	square root of -1
J	inertia
k _{pa}	pitch factor as given by Alger (50)
k _{ps}	pitch factor as given by Say (52)
k _{SK}	skew factor
k _{wn}	n th harmonic winding factor
k _{WT}	equivalent circuit winding factor
L	inductance
L _{EW}	end winding leakage inductance
L _{HARM}	harmonic leakage inductance
L _L	commutation choke
L _{LOAD}	load inductance
L _m	magnetising inductance
L _{SB}	slot bottom leakage inductance
L _{SKEW}	skew leakage inductance
L _{SLOT}	slot leakage inductance
L _{ST}	slot top leakage inductance
L ₁	stator leakage inductance
L ₂	rotor leakage inductance
L ₂ '	equivalent circuit referred rotor leakage inductance
L _{2DIFF}	differential leakage inductance
m	number of stator phases
M	modulation depth
M	number of waveform switching angles per cycle
M	magnetising inductance

N_{ph}	number of turns per phase
N_R	number of rotor bars
N_S	number of stator slots
p, P	number of pole pairs
p	differential operator
P_{IN}	input power
P_{LOSS}	power loss
P_{OUT}	output power
R	resistance
R	frequency ratio
R_{bar}	rotor bar resistance
R_D	voltage discharge resistor
R_f	semiconductor forward resistance
R_I	iron loss resistance
R_L	dc resistance of commutation choke
R_{LOAD}	load resistance
R_{ring}	rotor end-ring resistance
R_1	stator resistance
R_2	rotor resistance
R_2'	equivalent circuit referred rotor resistance
s	skew (as a fraction of a rotor slot pitch)
s	slip
s_n	n^{th} time harmonic slip
s_n^*	n^{th} space harmonic slip

t	time
t_{ON}	thyristor turn-on time
T_e	electrical torque
T_m	mechanical torque
T_n	n^{th} time harmonic torque
T_{total}	total torque
TA	auxiliary thyristor
TM	main thyristor
v	time varying voltage
v_f	semiconductor series reverse voltage
V	voltage
V_A, V_B, V_C	line voltages
V_{AB}	voltage across lines A and B
V_C	commutation capacitor voltage
V_{C0}	initial capacitor voltage
V_{C1}	final capacitor voltage
V_E	dc supply voltage
\hat{V}_n	n^{th} time harmonic peak voltage
\bar{V}_n	n^{th} time harmonic rms complex voltage
V_{ph}, V_{phase}	phase voltage
V_q, V_d, V_Q, V_D	d,q axis rotor and stator voltages
V_{SN}, V_{CN}	Fourier voltage coefficients
w'	effective machine length
W	power loss
Y	stator slot pitch

α_k	k^{th} waveform switching angle
α_{min}	minimum pulse width
α_t	temperature coefficient
$\delta\alpha$	angle increment
δx	width of rotor slot top strip in x direction
δy	width of rotor slot top strip in y direction
ξ	damping coefficient
θ_n	phase angle of the n^{th} time harmonic waveform
λ_{GN}	specific permeance of n^{th} airgap strip
λ_s	specific permeance of stator slot
λ_{SN}	specific permeance of n^{th} slot top strip
λ_{SB}	specific permeance of rotor slot bottom
μ_0	permeability of free space
ρ	resistivity
ρ	rotor bar resistivity
σ	distortion factor
σ'	approximated distortion factor
ϕ_{GN}	flux crossing the airgap at the n^{th} strip
ϕ_n	phase angle of n^{th} time harmonic waveform
ϕ_n	flux crossing the n^{th} section in rotor slot bridge
ϕ_{SN}	flux crossing the rotor slot top for the n^{th} strip
ϕ_1	flux entering the complete rotor slot bridge

Φ	Liwschitz-Garik correction factor for resistance
ψ	Liwschitz-Garik correction factor for inductance
ψ	waveform angle
ω_d	damped natural frequency
ω_0	supply frequency
ω_r	rotor speed (rad/s)
ω_{sn}	supply n^{th} time harmonic frequency

CHAPTER ONE

INTRODUCTION

Many industrial processes are dependent on variable speed electrical machines and indeed, some existing processes which use fixed speed drives may well benefit from the application of variable speed (1). The provision of variable speed has, in the past, been provided largely by dc machines because of the ease with which their speed may be controlled. DC machines are however expensive to produce and their brushes and commutators, which involve rubbing contact and wear, require regular maintenance. The cage induction motor, on the other hand, has a robust construction and is relatively cheap to produce. Unfortunately, the induction machine is essentially a fixed speed device when fed from a constant frequency ac supply.

The speed of a cage induction motor can be changed using several methods, which may be broadly classified as slip control or synchronous speed control. Slip control (2) is achieved by varying the motor supply voltage, using an autotransformer, tapped windings, or more recently, a solid-state phase angle controller. Rotor efficiency is given by $(1-SLIP)$, so controlling speed by increasing slip incurs an unavoidable penalty of reduced efficiency. Slip controllers are therefore confined largely to low power motors where low capital cost and simplicity outweigh the considerations of increased running cost.

The synchronous speed of a cage motor may be controlled by changing the supply frequency or the pole number. Pole changing involves the use of special windings, which may be reconfigured through the use of switches, to give different pole numbers. Alternatively, the motor may be wound with two separate windings giving two synchronous speeds;

one winding being excited whilst the other is held open circuit. In either case, a fixed number of speeds will result rather than a continuous variation. Continuous speed control may be achieved, either by using special machines such as spherical (3) and log motors (4) (which have proved commercially less attractive than originally hoped) or by continuously varying the motor's supply frequency (frequency control).

Frequency control of induction motors became a viable proposition through the use of static frequency converters employing thyristors. The most effective of these is the inverter which synthesises ac waveforms using a dc source. Early inverters were expensive and unreliable so their widespread use was not adopted. This trend has changed, largely because of the improved cost, reliability and power ratings of present day semiconductors and, in addition, because of the availability of inexpensive control circuitry based on LSI and microprocessor technology (5).

There are many types of power semiconductor available, these being the thyristor, bipolar transistor, field effect transistor (FET) and the gate turn-off thyristor (GTO). Of these devices, the thyristor is the most popular because of the high power ratings available, its relatively low cost and its ability to withstand reasonable fault currents. Their principal disadvantage, is that in dc excited converter circuits they must be force-commutated, with attendant expensive circuitry and increased probability of failure. For this reason, other devices, particularly the bipolar transistor, are gaining ascendancy at the power ratings for which they are viable.

The early type of inverter produced quasi-square-wave output and operated from variable-voltage dc supplies (to comply with the need to keep the motor fully fluxed). This type of inverter has two disadvantages.

Firstly, a separate dc supply is required to maintain commutation capability at low output frequencies. Secondly, the presence of large harmonics in the quasi-square wave output causes adverse harmonic effects in the motor. To obviate the need for a variable voltage dc supply, the technique of pulse width modulation (PWM) was developed. Here, the inverter, fed from a fixed dc supply, is controlled in such a way as to produce an output line waveform consisting of a number of pulses, lying within the usual square wave outline. The inverter output voltage is controlled by varying the widths of these pulses. Many different methods of producing this type of waveform have been developed which are referred to as PWM switching strategies. The simpler PWM strategies may be produced using analogue control circuitry. More recently the decrease in the cost of digital technology has led to the implementation of complex strategies.

At present, much attention is being paid to the improvement of inverter/motor drive efficiencies because of the rapidly increasing cost of energy. Little work appears to have been undertaken to improve inverter efficiency, as it is generally regarded as being high (of the order of 97% at rated output). Possible means of improving motor efficiency through changes in motor design have been investigated by several authors (6,7,8). Increased efficiency is shown to be achievable but at the expense of costly modifications to existing motor fabrication processes which would reduce the low cost advantages of mass produced induction motors.

Alternative means of improving drive efficiency are available which require no changes to existing hardware. Assuming fixed losses in the inverter, drive efficiency may be increased through improvement of the motor efficiency. An induction motor is usually operated according to

a fixed v, f characteristic so that the motor is always operating at its rated flux level. However, at low output torque, the flux level produced according to the v, f characteristic is higher than necessary, therefore extra losses are incurred. By suitably altering the supply voltage, an optimum flux level may be attained and so the efficiency of the motor improved. This technique of "optimum voltage control" has been investigated in the literature, where the efficiency increases to be gained are shown to be substantial, especially at lower output torques (1,9,10). The practical implementation of this method requires a more complex inverter controller which is capable of adaptive control, in that the inverter output voltage must be capable of being adjusted according to the loading conditions on the motor. The inverter controller needed to achieve this is expensive but, if the motor is to be run frequently on light load, the extra expense is justified (11).

An alternative to optimum voltage control is to operate the drive using an optimum PWM switching strategy; i.e. the strategy which produces the maximum drive efficiency. An extra complication arises here because a PWM switching strategy may be realised using many different numbers of switches (commutations) per cycle. The number of switches per cycle to adopt is a major consideration as each switch causes losses in the inverter due to commutation. Previous comparisons of PWM strategies undertaken in the literature have recognized the importance of this, but have been unable to predict the losses in the inverter, (12,13,14). These comparisons have therefore been restricted to one particular number of switches per cycle so that the inverter losses remain constant for each strategy considered. The PWM switching strategies are then compared on the basis of total rms current distortion in the motor.

In all the PWM strategies, increasing the number of switches per cycle reduces the harmonic content of the inverter output thereby increasing the motor efficiency. As the number of switches per cycle increases, the losses due to commutation increase, and so the inverter efficiency decreases. The drive (system) efficiency is the product of inverter and motor efficiency. This indicates that a number of switches per cycle must logically exist, which leads to maximum system efficiency. Consequently, the optimum PWM switching strategy must be derived, not only by comparison of the strategies, but also through comparison of the number of switches per cycle. The previous comparisons are therefore ineffectual in the derivation of a strategy which optimises system efficiency, as they are restricted to one particular number of switches per cycle.

This thesis is concerned with comparing four of the most popular PWM strategies for varying numbers of switches per cycle to derive that strategy which maximises system efficiency. To facilitate this, a method of predicting the total power losses in an inverter/induction motor drive is developed. The inverter simulation, which utilises the simple V,R model for a conducting semiconductor, together with analytical expressions describing the inverter operation is developed in Chapter Two. The model for the induction motor, based on the harmonic equivalent circuit method (15), is described in Chapter Three. These two models are combined in Chapter Four to produce the system model. The comparison of the PWM strategies is undertaken using this model and the results are presented and discussed in Chapter Five.

CHAPTER TWO

DEVELOPMENT OF THE INVERTER MODEL

2.1 Choice of Modelling Technique

The calculation of system efficiency requires that an accurate method of predicting the power loss in the three phase inverter is developed. To this end, a simple model for the circuit semiconductors and a suitable simulation method have to be obtained.

Thyristor models of varying complexity have been proposed in the literature (16,17,18). The simplest model, presented by Revankar (19), represents the thyristor as an ideal switch; which is a short circuit when the thyristor is conducting and an open switch when blocking. This representation is adequate for simulating circuit operation but is unsatisfactory when the power losses in the drive are to be derived.

The most complex models, of the type proposed by Browne (20), are based on the solution of the mathematical equations describing the physical behaviour of the semiconductor regions and their junctions. These models suffer from two features which make them unsuitable for use in circuit simulations. Firstly, they depend on precise knowledge of the geometry of the device and its properties. Such information is generally unavailable and this limits the model to design studies of the devices themselves. Secondly, they are unsuitable for interfacing with the rest of the circuit in which the thyristor is contained.

This limitation is partly overcome by using commercially available circuit simulation packages such as SPICE, ASTAPS and SUPER-SCEPTRE.

Although such packages do not directly model thyristors, alternative representations for the thyristor can be used. Williams (21) proposed using a two transistor equivalent which models accurately all thyristor properties including high frequency effects such as reverse recovery. Ghani (22) adopted a much simpler representation using standard circuit elements, these being controlled by current-dependent switches. Both representations model the thyristor accurately but because of the difficulty in deriving model parameters, and because the representations are, in effect, too complex for use in the present study, it was consequently decided to seek a much simpler method of solution.

The method chosen was based on the model proposed by Kutman (23). The semiconductor devices are represented by a resistance in series with an ideal reverse-connected voltage source, as shown in Fig. 2.1. The values of the components used are determined from the manufactures published conduction characteristics, as illustrated in Fig. 2.2. R_f is given by the reciprocal of the tangent to the conduction characteristic at the rated operating point, and V_f is the intercept made by this tangent on the voltage axis. A blocking thyristor is modelled as an ideal open switch, as are reverse biased diodes. The conducting power loss in a device carrying a current $i(t)$ is calculated from $i^2(t)R_f + i(t)V_f$. This model takes no account of device switching losses, which are discussed later (section 2.6).

A suitable means of applying the model to the circuit has to be found. Two methods of simulating circuits containing switching devices are commonly used. The first of these is an analytical technique (24,25,26) which involves deriving the physical equations describing the circuit operation. The nature of these circuits is such that more than one set of equations is necessary to define the circuit operation. Therefore, the function of the circuit is segmented into regions where

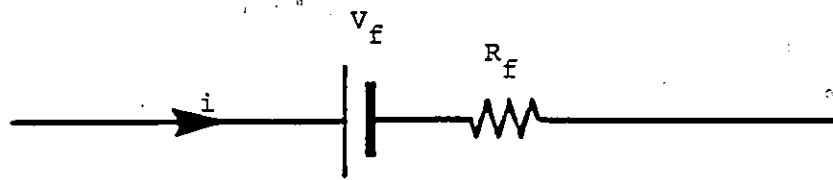


Fig. 2.1 V-R model for thyristors and diodes

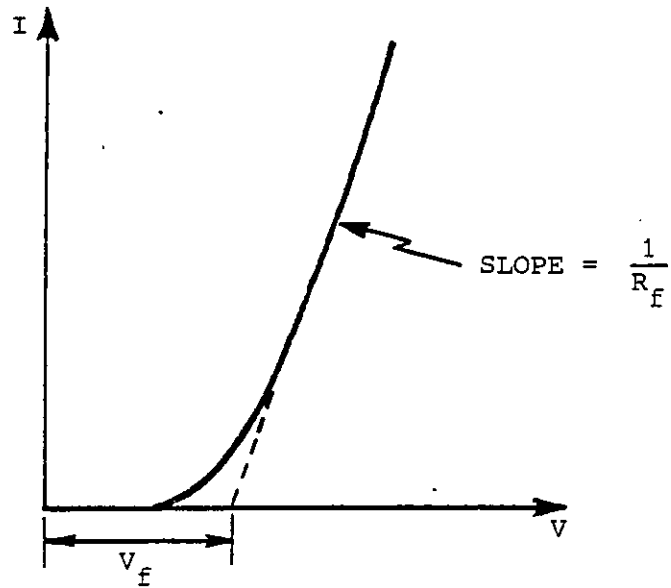


Fig. 2.2 Determination of model components from device characteristics

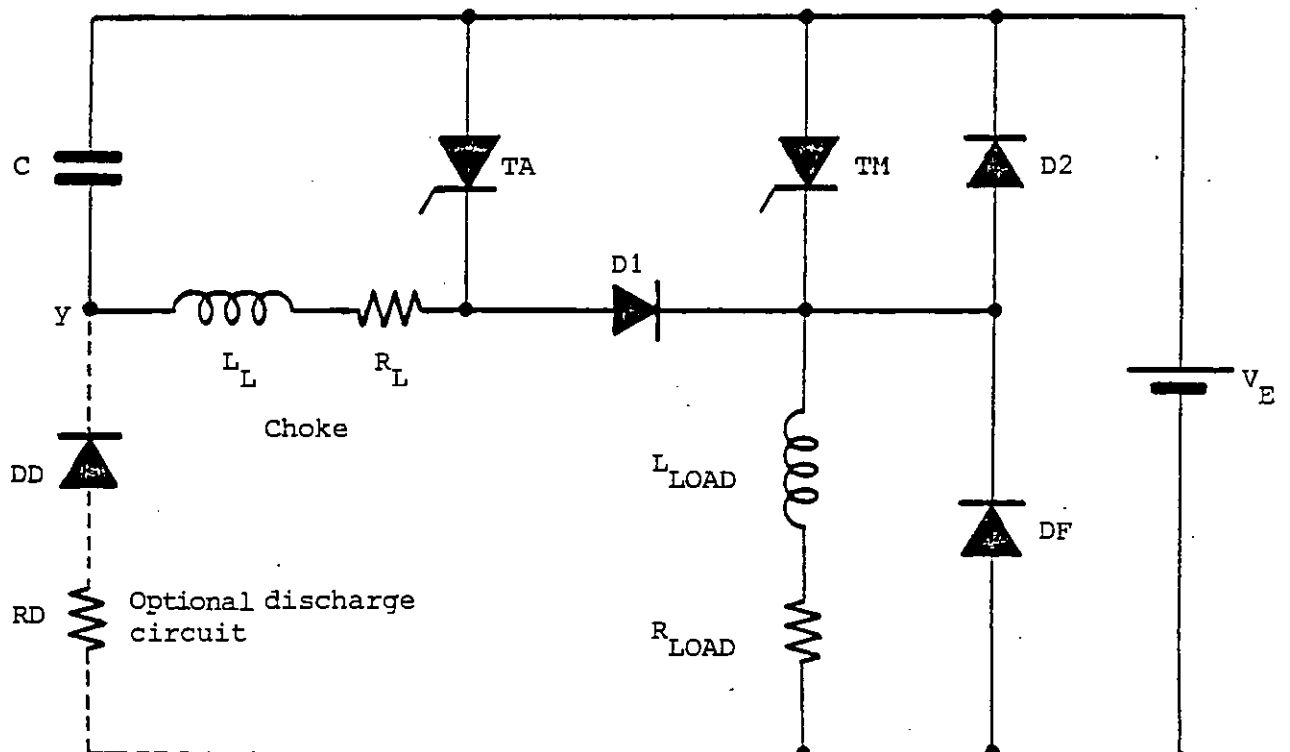


Fig. 2.3 Impulse commutated chopper used in experimental work

the current paths are constant. This necessitates detailed knowledge of the circuit operation.

The second method involves the use of numerical techniques (27,28,29,30) to simplify the simulation procedure with no prerequisite understanding of the circuit operation. This technique involves the numerical solution of the state equations describing the circuit. Network theory, in conjunction with a time-step mode of simulation, is used to modify the network topology - and the associated state equations - as the circuit devices change their conduction state.

In this study the analytical approach was adopted. Firstly, because the operation of most switching circuits is usually well defined. Secondly, because this study requires repetitive calculation of the circuit losses, the problem of understanding the circuit operation was far outweighed by the substantial reductions in computer time.

2.2 Analysis of the DC Chopper

A current impulse commutated DC chopper, illustrated in Fig. 2.3, was chosen to verify the suitability of the V,R model and the simulation method adopted. The control logic, gate drives, and snubber components have been omitted for clarity. The values for the circuit components are given in Table 2.1. The optional discharge circuit indicated by the dashed lines in Fig. 2.3 was disconnected for the work in this section to enable accurate experimental verification of the theory to be presented. This is further referred to in section 2.3.

The energy dissipated in the chopper during one complete operation cycle, or pulse, is calculated and compared with measurement to verify

$$V_{TM} = 1.8 \text{ V}$$

$$V_{TA} = 1.8 \text{ V}$$

$$\left. \begin{array}{l} V_{D1} \\ V_{D2} \\ V_{DF} \\ V_{DD} \end{array} \right\} = 0.6 \text{ V}$$

$$\left. \begin{array}{l} R_{TM} \\ R_{TA} \\ R_{D1} \\ R_{D2} \\ R_{DF} \\ R_{DD} \end{array} \right\} = 0.02 \text{ } \Omega$$

$$C = 0.5 \text{ } \mu\text{F}$$

$$L_L = 60 \text{ } \mu\text{F}$$

$$R_L = 0.025 \text{ } \Omega$$

$$R_D = 5.6 \text{ } \Omega$$

$$\left. \begin{array}{l} C_{SM} \\ C_{SA} \end{array} \right\} = 33 \text{ nF}$$

$$V_E = 31 \text{ V}$$

$$\text{Thyristor rating: } V_{DRM_{\max}} = 800 \text{ V} \quad I_{T(av)_{\max}} = 9.5 \text{ A}$$

$$\text{Diode rating: } V_{RRM_{\max}} = 800 \text{ V} \quad I_{F(av)_{\max}} = 7.0 \text{ A}$$

Table 2.1 Chopper circuit component values

the simulation theory.

A pulse is defined as the period from the triggering of the main thyristor to the point at which the circuit reaches steady state after the auxiliary thyristor has been fired.

The circuit losses can be separated into two components, those due to the forward conduction of current - known as the conduction losses - and those due to changes in state of the semiconductor devices - known as switching losses.

To calculate the conduction losses the circuit operation has to be resolved into intervals in which unique current paths exist. The energy dissipated in a device can be calculated from $\int [i(t)V_f + i^2(t)R_f]dt$ over the interval. R_f and V_f are assumed to be constant so that the energy loss can be calculated as $[it]V_f + [i^2t]R_f$, where $[it]$ and $[i^2t]$ represent the time integrals of current and current squared over the interval.

2.2.1 Calculating the Time Integrals: The time integrals can be calculated by analysing the action of the circuit almost entirely using series RLC circuits. For the general circuit shown in Fig. 2.4

$$i(t) = e^{-\xi t} (A \sin \omega_d t + B \cos \omega_d t) \quad (2.1)$$

By considering the initial conditions at $t = 0$, $i = I_0$, $V_C = V_{C0}$ then

$$B = I_0 \quad (2.3)$$

$$A = \frac{2(V - V_{C0}) - I_0 R}{2\omega_d L} \quad (2.3)$$

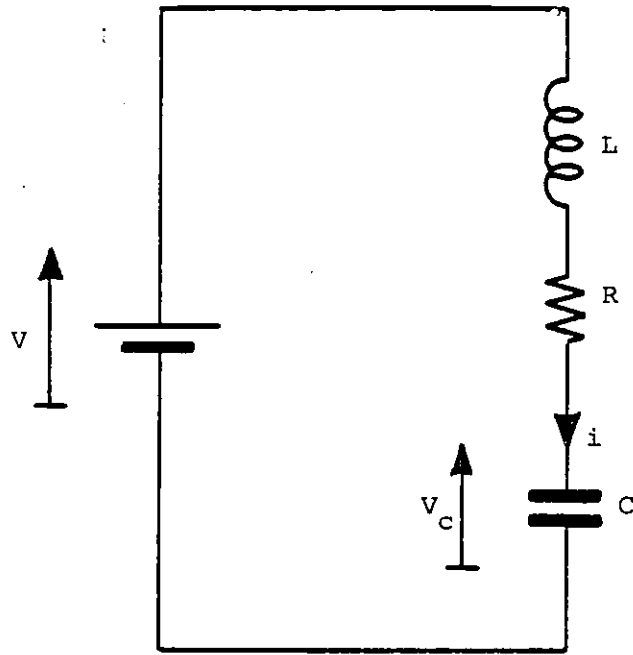


Fig. 2.4 Series RLC circuit for $[it]$ and $[i^2t]$ calculations

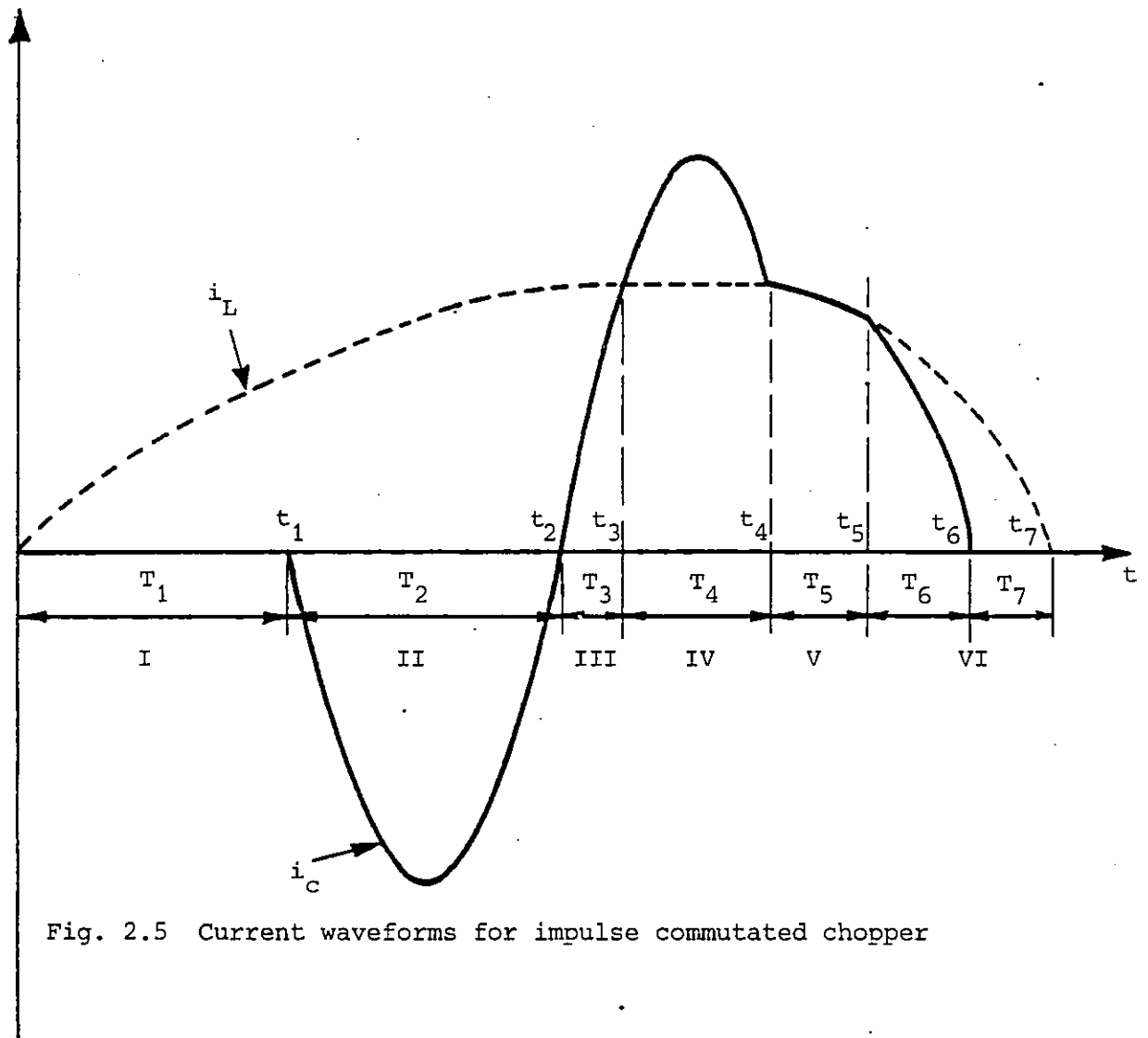


Fig. 2.5 Current waveforms for impulse commutated chopper

where ω_d is given by

$$\omega_d = \sqrt{\frac{1}{LC} - \frac{R^2}{4L^2}} \quad (2.4)$$

and ξ by

$$\xi = \frac{R}{2L} \quad (2.5)$$

The final conditions at $t = T$, $i = I_1$, $V_C = V_{C1}$ can now be calculated as

$$I_1 = e^{-\xi T} (A \sin \omega_d T + B \cos \omega_d T) \quad (2.6)$$

and from

$$V = V_{C1} + I_1 R + L \frac{dI_1}{dt} \quad (2.7)$$

$$V_{C1} = V - \frac{I_1 R}{2} - \omega_d L e^{-\xi T} (A \cos \omega_d T - B \sin \omega_d T) \quad (2.8)$$

Furthermore, since

$$i = C \frac{dv}{dt} \quad (2.9)$$

then

$$[it] = \int_0^T i dt = C[V_{C1} - V_{C0}] \quad (2.10)$$

Also, by writing an energy balance

$$\begin{array}{lcl} \text{Energy input} & & \text{Increase in stored} \\ \text{from source} & = & \text{energy in L and C} \\ & & + \text{Energy dissipated} \\ & & \text{in R} \end{array}$$

$$\int_0^T i^2 dt = \frac{C}{2} [V_{C1}^2 - V_{C0}^2] + \frac{L}{2} [I_1^2 - I_0^2] + \int_0^T i^2 R dt \quad (2.11)$$

which gives

$$[i^2 t] = \int_0^T i^2 dt = \frac{1}{R} \left\{ CV(V_{C1} - V_{C0}) - \frac{C}{2} (V_{C1}^2 - V_{C0}^2) - \frac{L}{2} (I_1^2 - I_0^2) \right\} \dots \dots (2.12)$$

In general, therefore, A and B are calculated using Equations 2.2 and 2.3, with the initial values of current and capacitor voltage (I_0 and V_{C0}). The final values, I_1 and V_{C1} , are then determined for the desired time period T, using Equations 2.6 and 2.8. The initial and final values may now be substituted into Equations 2.10 and 2.12 to give the required integrals. I_1 and V_{C1} then become the respective initial values I_0 and V_{C0} for the next time period.

2.2.2 Conduction Loss Calculations: The procedure for calculating the circuit semiconductor conduction losses using the above technique is presented below. The energy loss in the circuit commutation choke is calculated as $[i^2 t] R_L$, where R_L is the dc resistance of the choke. The commutation capacitor is assumed to be lossless. Although the circuit operation is adequately described in most undergraduate texts, a brief description of each period is given. As a further aid, typical load and commutation current waveforms are given in Fig. 2.5, with Figs 2.6(a) to 2.6(f) showing the current paths followed during the separate periods.

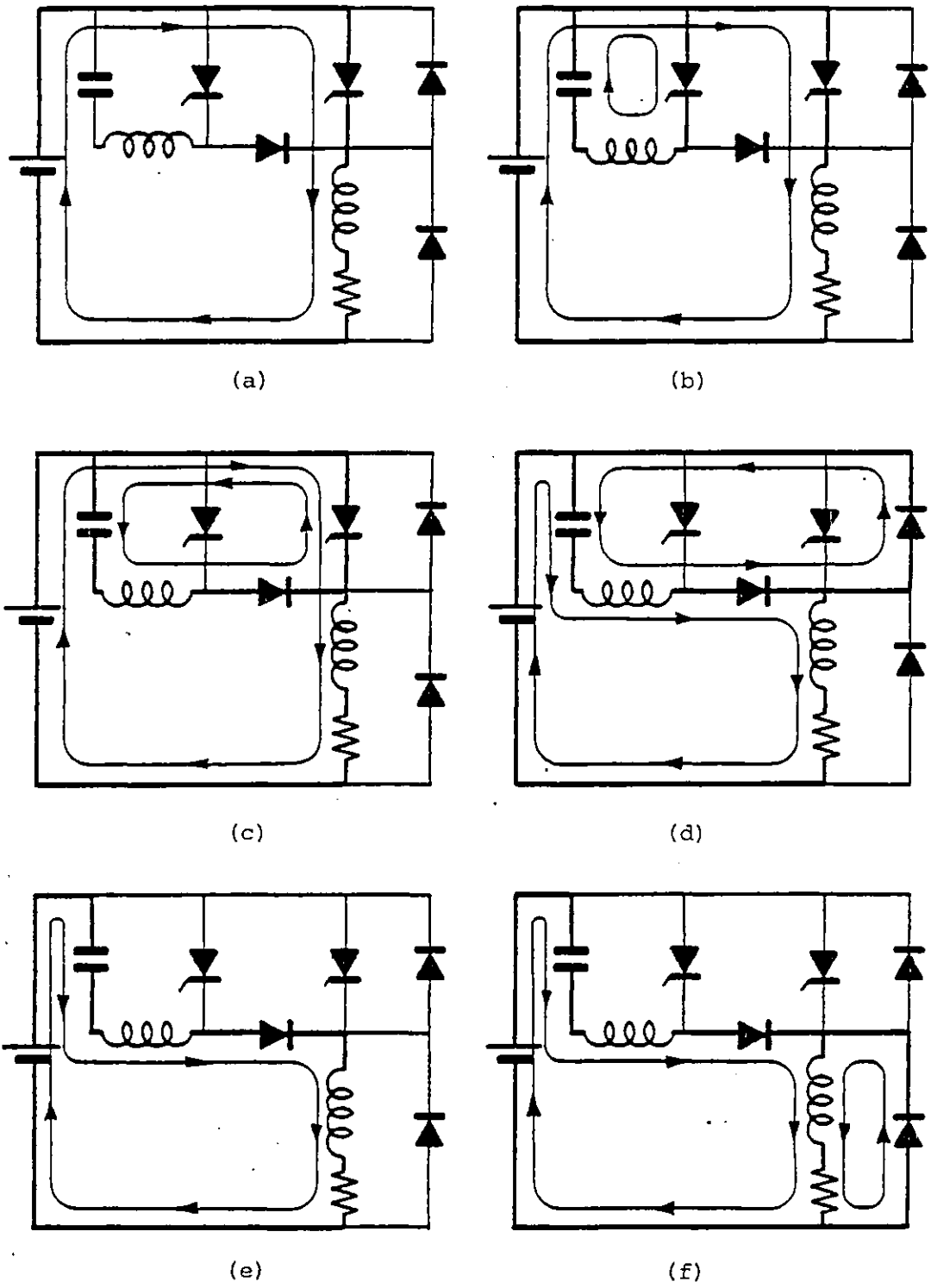


Fig. 2.6 Current flow paths during turn-on and commutation

2.2.2(i) Initial Conditions: Initially, it is assumed that both thyristors are blocking and that the capacitor is charged to voltage V_0 as a result of the previous cycle. If the discharge circuit is present then $V_0 = V_E$. If no discharge circuit is used then V_0 will be somewhat higher. In order to determine the value of V_0 , it is assumed to be equal to V_E for the first pulse. The procedure set out below is used to calculate the capacitor voltage at the end of each pulse, with this becoming the new value for V_0 at the start of the next. This process is repeated until initial and final values of capacitor voltage are found to correspond, giving the steady value for V_0 .

2.2.2(ii) Periods I and II: At time $t = 0$ the main thyristor (TM) is gated and load current flows along the path indicated in Fig. 2.6(a), increasing at a rate governed by the time constant of the load. After the required on-time, T_1 , the auxiliary thyristor (TA) is triggered and the capacitor reverses its charge via the choke and TA (Fig. 2.6(b)). The oscillatory nature of the discharge path causes the capacitor current to reverse direction, and TA becomes reverse-biased, turning off. The instant at which the capacitor current falls to zero defines the end of period II (i.e. at $t = t_2$ on Fig. 2.5).

For the main thyristor loss

$$[i_L t] = \frac{1}{R} \{V_T - L I_L\} \quad (2.13)$$

$$[i_L^2 t] = \frac{V}{R} [i_L t] - \frac{L I_L^2}{2R} \quad (2.14)$$

where

$$\left. \begin{aligned} V &= V_E - V_{TM} \\ R &= R_{LOAD} + R_{TM} \\ L &= L_{LOAD} \\ T &= T_1 + T_2 \end{aligned} \right\} \quad (2.15)$$

T_1 is the required on-time.

T_2 is given by Equation 2.17 below.

I_L is the final value of load current at the end of period II.

$$I_L = \frac{V}{R} \left\{ 1 - e^{-\frac{RT}{L}} \right\} \quad (2.16)$$

It is assumed that the load current remains constant at this value until the end of period IV.

For the losses in the choke and auxiliary thyristor, $[it]$ and $[i^2t]$ are determined as in section 2.2.1. The relevant component values are

$$\left. \begin{aligned} V &= V_{TA} & R &= R_L + R_{TA} \\ L &= L_L & T &= T_2 = \frac{\pi}{\omega_d} \end{aligned} \right\} \quad (2.17)$$

The initial conditions are $I_0 = 0$, $V_{C0} = V_0$.

The auxiliary thyristor conduction current flows in the direction opposite to that assumed for positive current flow in Section 2.2.1, so that the auxiliary thyristor loss is given by

$$W_{TA} = R_{TA} [i^2t] - V_{TA} [it] \quad (2.18)$$

2.2.2(iii) Period III: After reversal, the capacitor current flows via D1 and TM as shown in Fig. 2.6(c). TM continues to conduct until the capacitor current and load current are equal (i.e. at time $t = t_3$).

For the losses in the choke and diode D1, $[it]$ and $[i^2t]$ are determined as in section 2.2.1. The relevant component values are

$$\left. \begin{aligned} V &= V_{TM} - V_{D1} \\ R &= R_L + R_{TM} + R_{D1} \\ L &= L_L \\ T &= T_3 \approx \frac{1}{\omega_d} \sin^{-1} \left\{ \frac{I_L \omega_d L}{V_{CO} - V} \right\} \end{aligned} \right\} \quad (2.19)$$

For the losses in the main thyristor, use $[it]'$ and $[i^2t]'$ defined by

$$[it]' = I_L T_3 - [it] \quad (2.20)$$

$$[i^2t]' = I_L^2 T_3 + [i^2t] - 2I_L [it] \quad (2.21)$$

2.2.2(iv) Period IV: The capacitor current continues to increase and its excess over the load current flows via D1 and D2 (Fig. 2.6(d)). The forward voltage drop across D2 reverse-biases TM, turning it off. Current continues to flow through D2 until the capacitor current falls to a value equal to the load current (at $t = t_4$).

For the losses in the choke and diode D1, $[it]$ and $[i^2t]$ are determined using the general formulae given in section 2.2.1, together with

$$\left. \begin{aligned} V &= -V_{D1} - V_{D2} \\ R &= R_L + R_{D1} + R_{D2} \\ L &= L_L \\ T &= T_4 \approx T_2 - 2T_3 \end{aligned} \right\} \quad (2.22)$$

For the losses in diode D2, use $[it]'$ and $[i^2t]'$

$$[it]' = [it] - I_L T_4 \quad (2.23)$$

$$[i^2t]' = [i^2t] + I_L^2 T_4 - 2I_L [it] \quad (2.24)$$

2.2.2(v) Period V: The capacitor current flowing via D1 has fallen to be equal to the load current, so the current via D2 is zero. The voltage of point X (Fig. 2.3) falls below that of the positive rail. Both load and capacitor current now flow through D1 and the supply (Fig. 2.6(e)). Provided no capacitor discharge circuit is present, this mode of current flow continues until the load voltage falls to zero.

For the losses in the choke and diode D1, $[it]$ and $[i^2t]$ are determined in section 2.2.1 with

$$\left. \begin{aligned} V &= V_E - V_{D1} \\ R &= R_L + R_{D1} + R_{LOAD} \\ L &= L_L + L_{LOAD} \\ T &= T_5 \end{aligned} \right\} \quad (2.25)$$

T_5 is the time required for the load voltage to fall to zero, given by

$$T_5 = \frac{\pi - \phi}{\omega_d} \quad (2.26)$$

where

$$\phi = \tan^{-1} \left\{ \frac{\omega_d A L_{LOAD} + B R_{LOAD} - \zeta B L_{LOAD}}{A R_{LOAD} - \omega_d B L_{LOAD} - \zeta A L_{LOAD}} \right\} \quad (2.27)$$

2.2.2(vi) Period VI: The load voltage is now clamped to zero via DF, so that the energy stored in the load inductance is dissipated in DF and in the load resistance (Fig. 2.6(f)). The energy stored in the commutation choke is in part transferred to the over-charging commutation capacitor and in part dissipated in the choke's own resistance and D1. The load and capacitor current now look as shown for period VI on Fig. 2.5, assuming no discharge circuit is connected.

For losses in the choke and diode D1, $[it]$ and $[i^2t]$ are determined as in section 2.2.1 with

$$\left. \begin{aligned} V &= V_E - V_{D1} \\ R &= R_L + R_{D1} \\ L &= L_L \\ T &= T_6 = \frac{\pi - \tan^{-1} \left(\frac{B}{A} \right)}{\omega_d} \end{aligned} \right\} \quad (2.28)$$

For losses in the flywheel diode DF

$$[it]' = \frac{I_0 L_{LOAD}}{R_{LOAD}} - [it] \quad (2.29)$$

$$\begin{aligned} [i^2t]' &= \frac{I_0}{2} [it]' + [i^2t] - \\ &2I_0 C \left\{ v - v_{C0} - e^{-\left(\zeta + \frac{R_{LOAD}}{L_{LOAD}} \right) T} \left(\left(\frac{AR}{2} - \omega_d LB \right) \sin \omega_d T \right. \right. \\ &\quad \left. \left. + \left(\frac{BR}{2} + \omega_d LA \right) \cos \omega_d T \right) \right\} \end{aligned} \quad (2.30)$$

If a discharge circuit is used, then all the energy stored in the commutation choke at the start of period VI is dissipated. It may be calculated as $\frac{1}{2} L_L i_L^2$ where i_L is the load current at $t = t_5$. This energy loss replaces the expressions for the loss in diode D1 and the choke, obtained using Equation 2.28 above.

2.2.3 Switching Loss Calculations: The energy loss due to the thyristor snubbers (Fig. 2.7) is the only switching loss considered in this section. A more detailed discussion on switching loss is presented later in section 2.6.

When the main thyristor blocks, its snubber capacitor charges to the supply voltage, V_E . During charging the energy loss in the snubber resistance is equal to the energy stored in the snubber capacitor, $\frac{1}{2} C_{SM} V_E^2$. When the thyristor turns on, the snubber capacitor discharges and dissipates all its stored energy in the resistance. The total energy loss in the main thyristor snubber is therefore $C_{SM} V_E^2$ joules per cycle. The snubber loss for the auxiliary thyristor is similarly given by $C_{SA} V_C^2$, where V_C is the voltage on the commutation capacitor, calculated as shown in section 2.2.2(i).

The snubber energy losses are added to the accumulated sum of conduction losses to give the total energy loss during one pulse.

2.3 Experimental Verification of the DC Chopper Simulation

The high power levels and fast transients inherent in power electronic circuits make measurements on these circuits difficult. Most standard laboratory instruments have neither the bandwidth, nor the input rating, to enable accurate measurement. As a consequence, special measurement

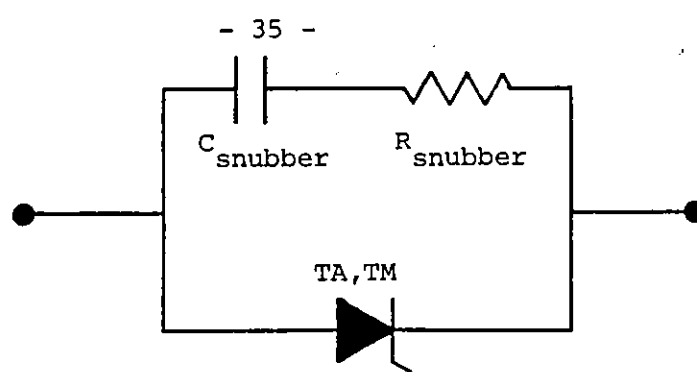


Fig. 2.7 Configuration of the thyristor snubbers

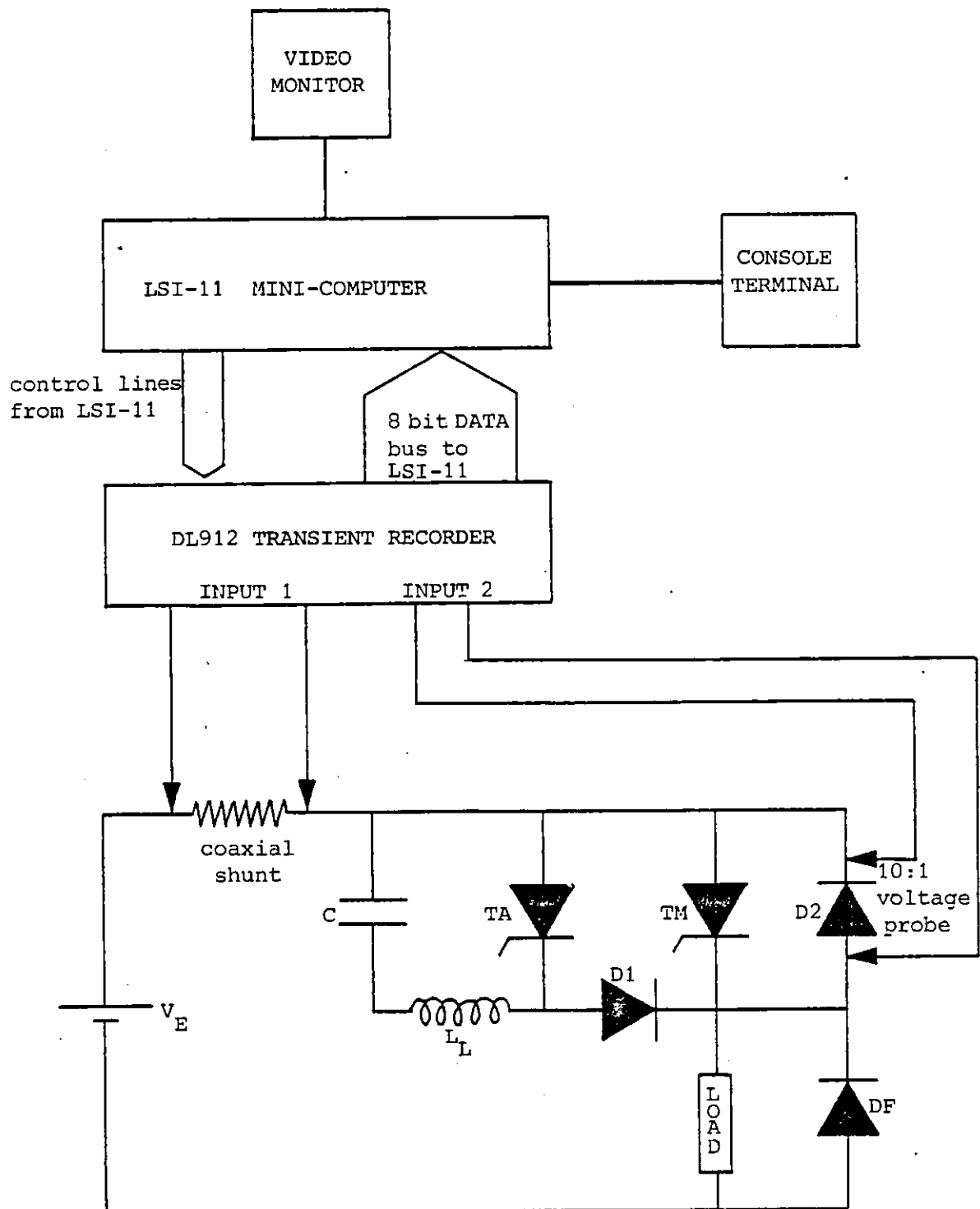


Fig. 2.8 Experimental set-up for verification of the DC chopper model

techniques have had to be developed. Lindsay (31) suggested a method which uses low bandwidth equipment. The correct readings are obtained by multiplying those observed by a factor calculated for the wave-shape being measured. This method is only suitable for use with waveforms which are well defined and relatively simple.

The calorific method (32) utilises the principle that energy dissipated in a device will cause a temperature rise which can be monitored. From this the power loss can be calculated. This technique is slow, requires careful control of ambient conditions, and is more suited to the measurement of power losses in single devices rather than the losses in a complete circuit.

In the most common method, known as power integration (33,34,35), voltage and current waveforms are multiplied to produce an instantaneous power loss curve. The area under this curve is determined to give the VIt product (the energy dissipated). This procedure can be performed manually using oscilloscope traces but it is then capable of only limited accuracy. The digital method adopted in this experimental work is both accurate and rapid.

The voltage and current waveforms were digitised and stored using a Datalab DL912 twin channel transient recorder. The voltage waveform was obtained using a 10:1 compensated voltage probe; the current waveform via a good quality coaxial shunt. Each channel of the DL912 consists of a 4 kbyte memory and an 8 bit analogue to digit converter (A/d). The sample time of the A/d was adjustable down to a minimum of 50 ns. In all the tests the sample time was chosen to produce the largest number of samples per pulse. This led to a bandwidth of 2.5 MHz or better.

The digitised waveforms stored in the recorder memories were transferred under program control to an LSI-11 mini-computer, where they were multiplied to give the instantaneous power loss curve which was then numerically integrated to determine the energy loss per pulse.

Energy losses in the chopper can be measured directly, or indirectly using this technique. Indirect measurement involves measuring the power flowing into the circuit and comparing it with that flowing out. This method has disadvantages when the load power is large compared to the converter power loss, because the accuracy with which the loss can be determined is consequently low. As it was the author's intention to test the chopper with resistive loads, with which this poor accuracy condition would arise, a direct measurement technique was chosen.

The direct method requires the chopper circuit to be configured as a single port network. This necessitated the removal of the discharge circuit and the separate measurement of the energy loss in the freewheel diode DF. The energy loss in the rest of the circuit was measured by considering the voltage across TM and the supply current. A block diagram of the experimental set-up is shown in Fig. 2.8 and an example of a measured instantaneous power loss curve is shown in Fig. 2.9.

The use of 8 bit converters results in a conversion resolution of 0.4% which is well within the accuracy of most measuring instruments. The rated operating voltage of the chopper used in this test is 570 V giving a resolution of ± 1.1 V. As the forward voltage measured across TM is approximately 1.8 V, the accuracy of measurement would be poor.

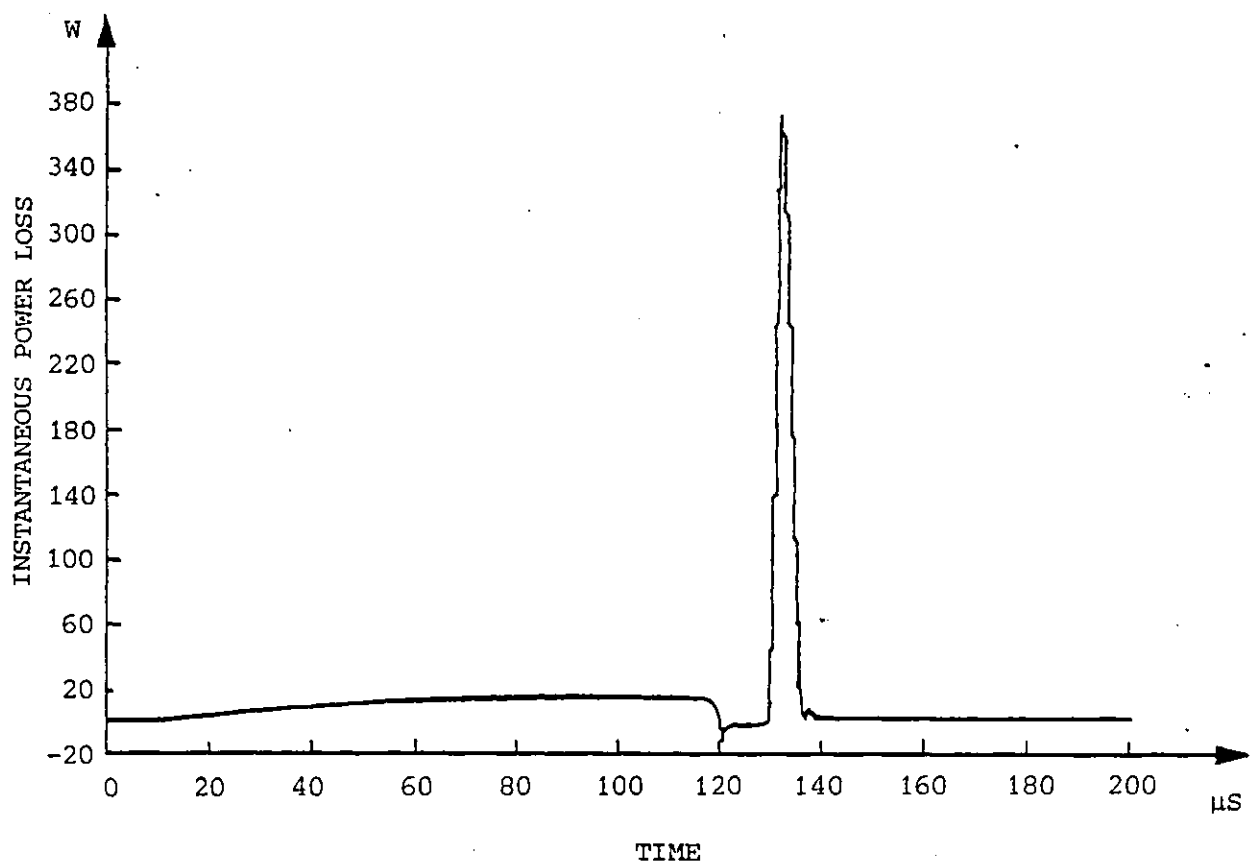


Fig. 2.9 Typical measured curve of instantaneous power loss against time for the dc chopper

To overcome this problem the operating voltage was reduced to 31 V giving a conversion resolution of ± 0.06 V. Operation of the chopper up to the rated current was possible because the commutation capacitor exhibited voltage boosting as a result of the discharge circuit being removed.

The energy loss in the chopper was measured for a variety of pulse widths, with both pure resistive and mixed resistive-inductive loads. The tests were carried out at reduced voltage but with load currents up to full rated design current for the chopper. The experimental results are shown in Figs. 2.10 to 2.13 along with their computed counterparts. The agreement between experiment and calculation will be seen to be good.

2.4 Analysis of the Three Phase Inverter

The model derived for the dc chopper can now be modified to calculate the power loss in the three phase inverter. One phase of the inverter is shown in Fig. 2.14 with the two constituent dc choppers being enclosed by dashed lines. A simplified representation of the full inverter is presented in Fig. 2.15, showing only the main thyristors and their associated freewheel diodes. The principle of operation of the inverter will not be discussed here as it is adequately described in a number of texts (36,37,38).

The model developed for the dc chopper model cannot be used in the inverter simulation without some modification. Firstly, the configuration of the inverter uses the reverse connected diodes across the main thyristors as the load freewheel diodes so that DF can no longer be included in the chopper model. Secondly, the current in the

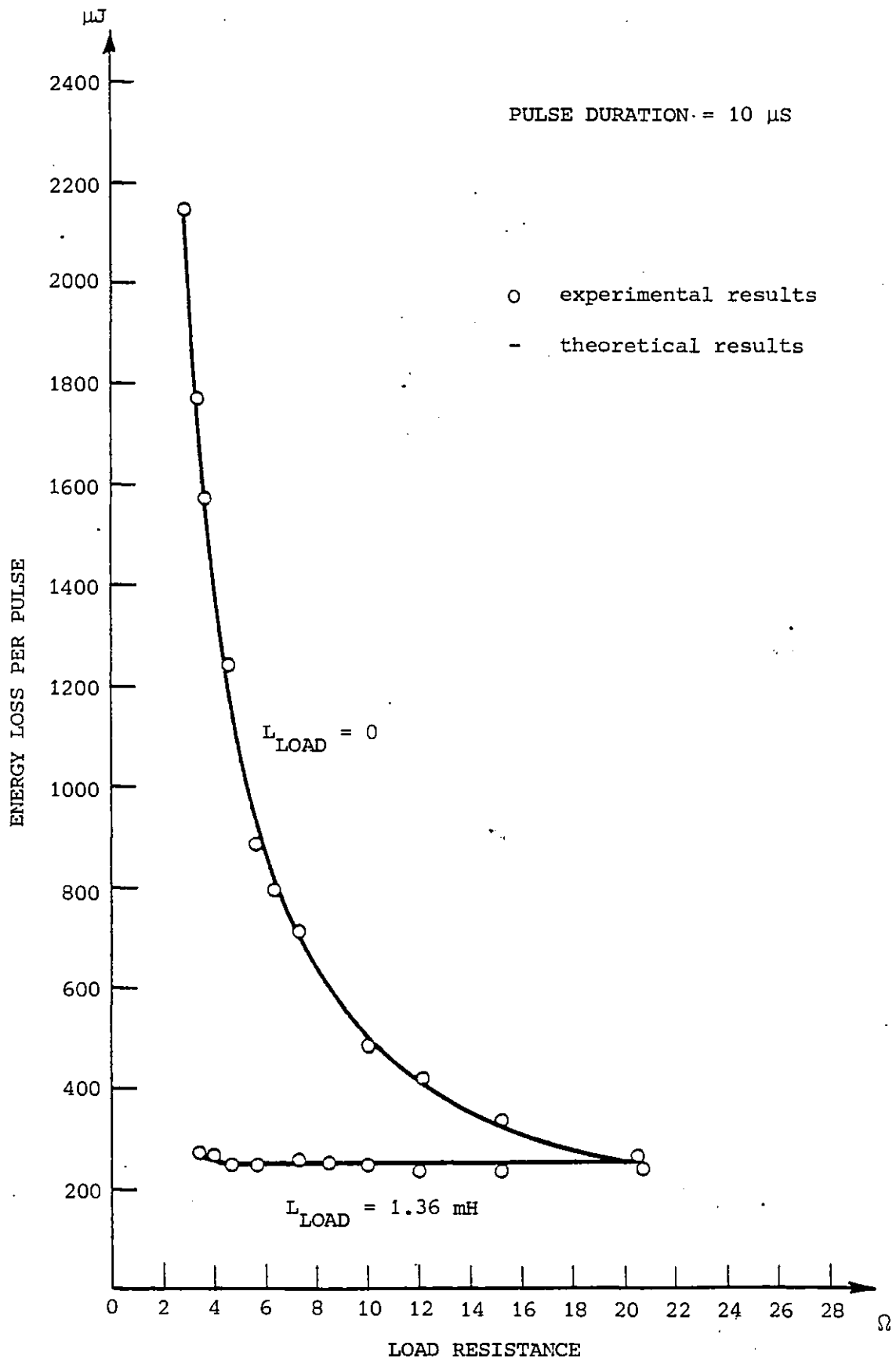


Fig. 2.10 Energy loss per pulse for 10 μ S on-time

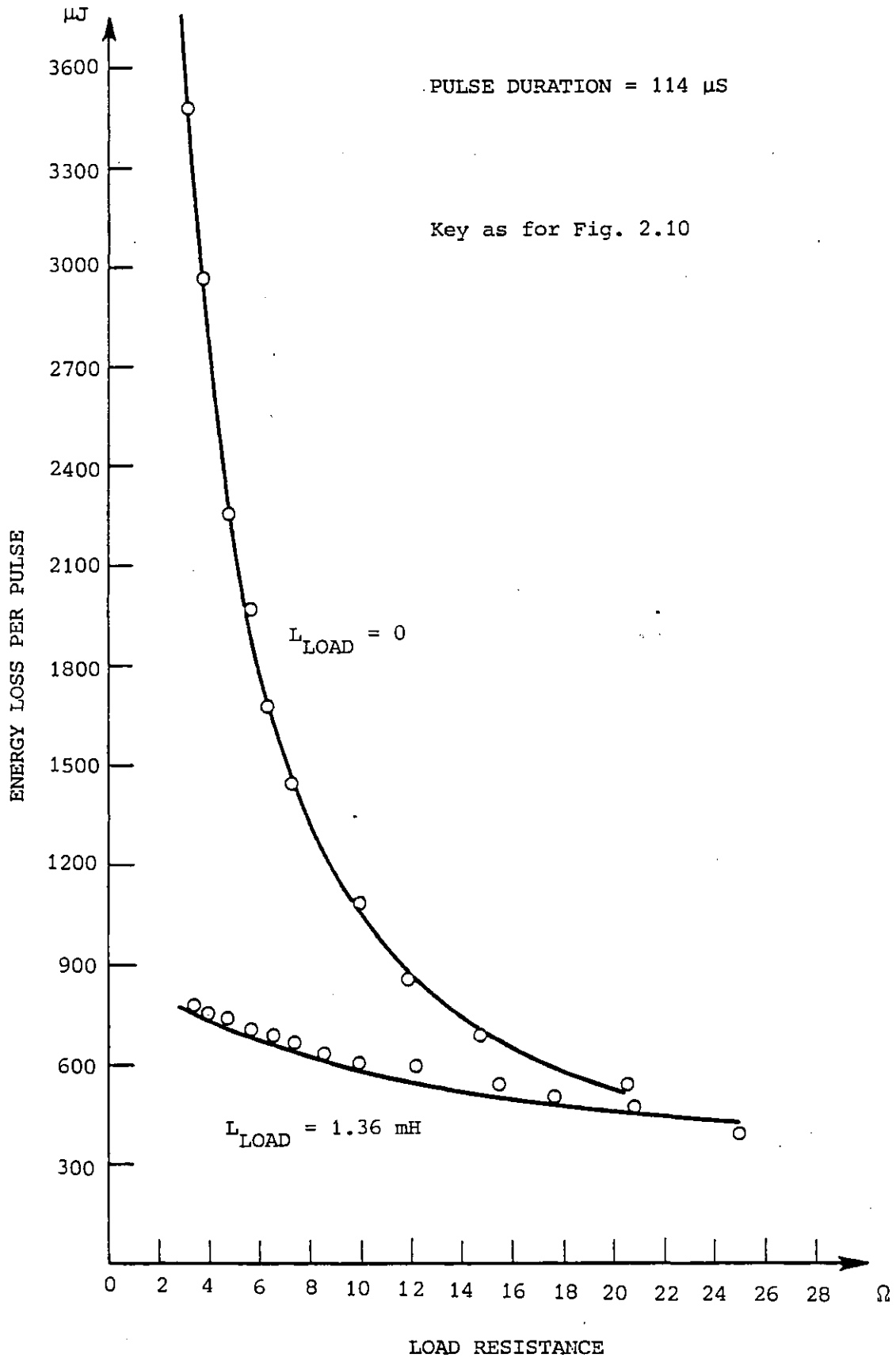


Fig. 2.11 Energy loss per pulse for 114 μ S on-time

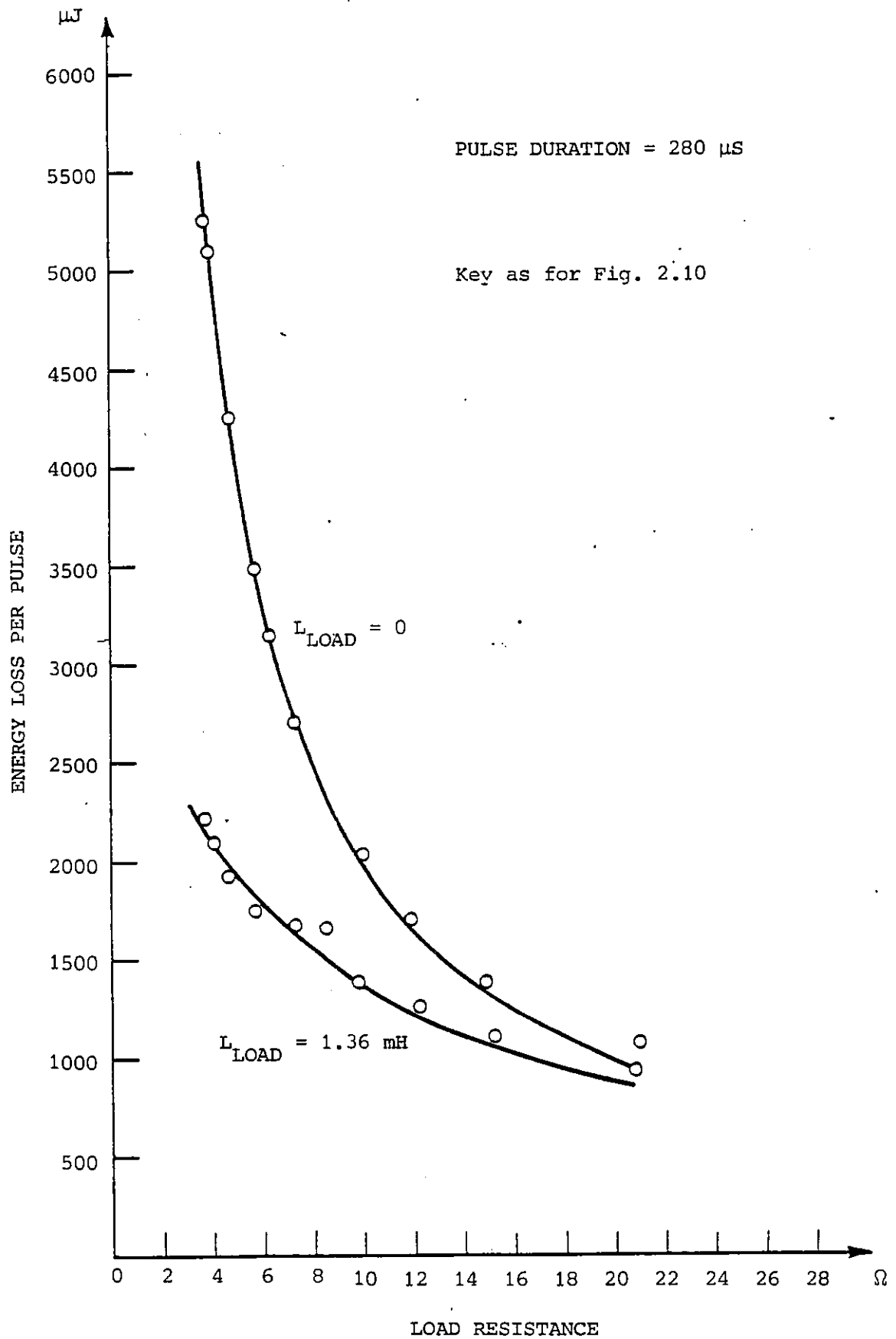


Fig. 2.12 Energy loss per pulse for 280 μ S on-time

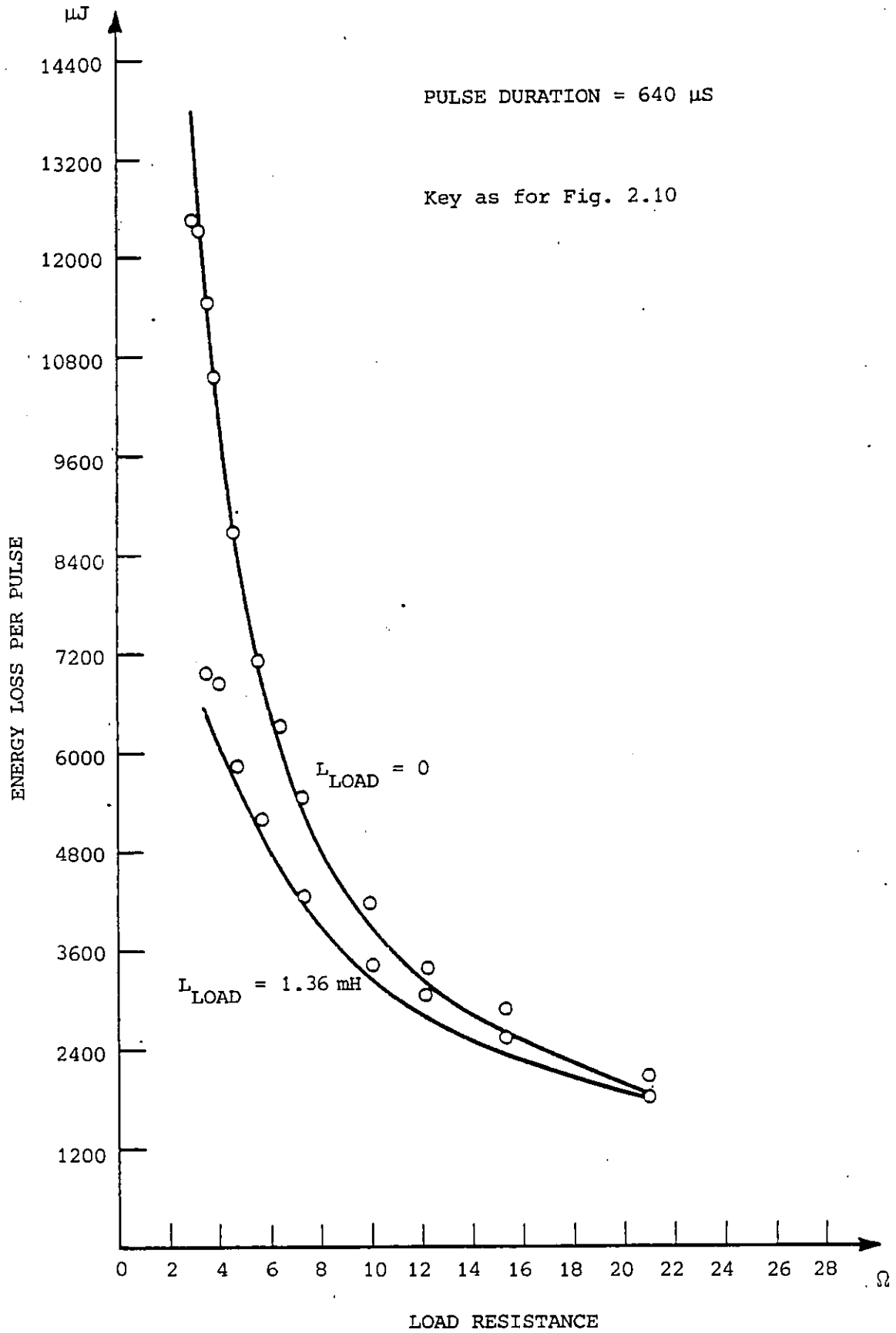


Fig. 2.13 Energy loss per pulse for 640 μ S on-time

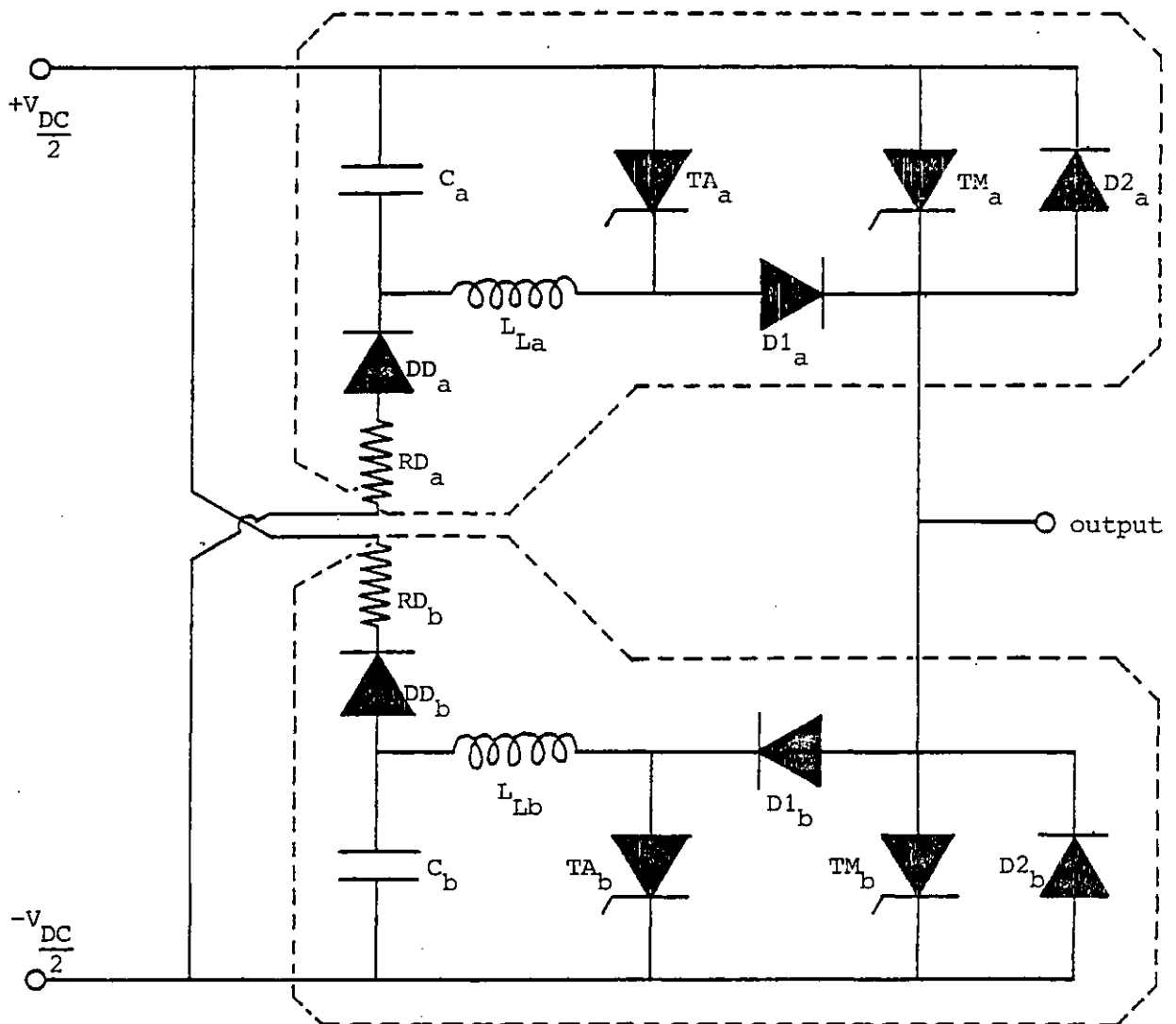


Fig. 2.14 Circuit diagram for 1 phase of the 3 phase inverter, showing constituent DC choppers enclosed by dashed lines

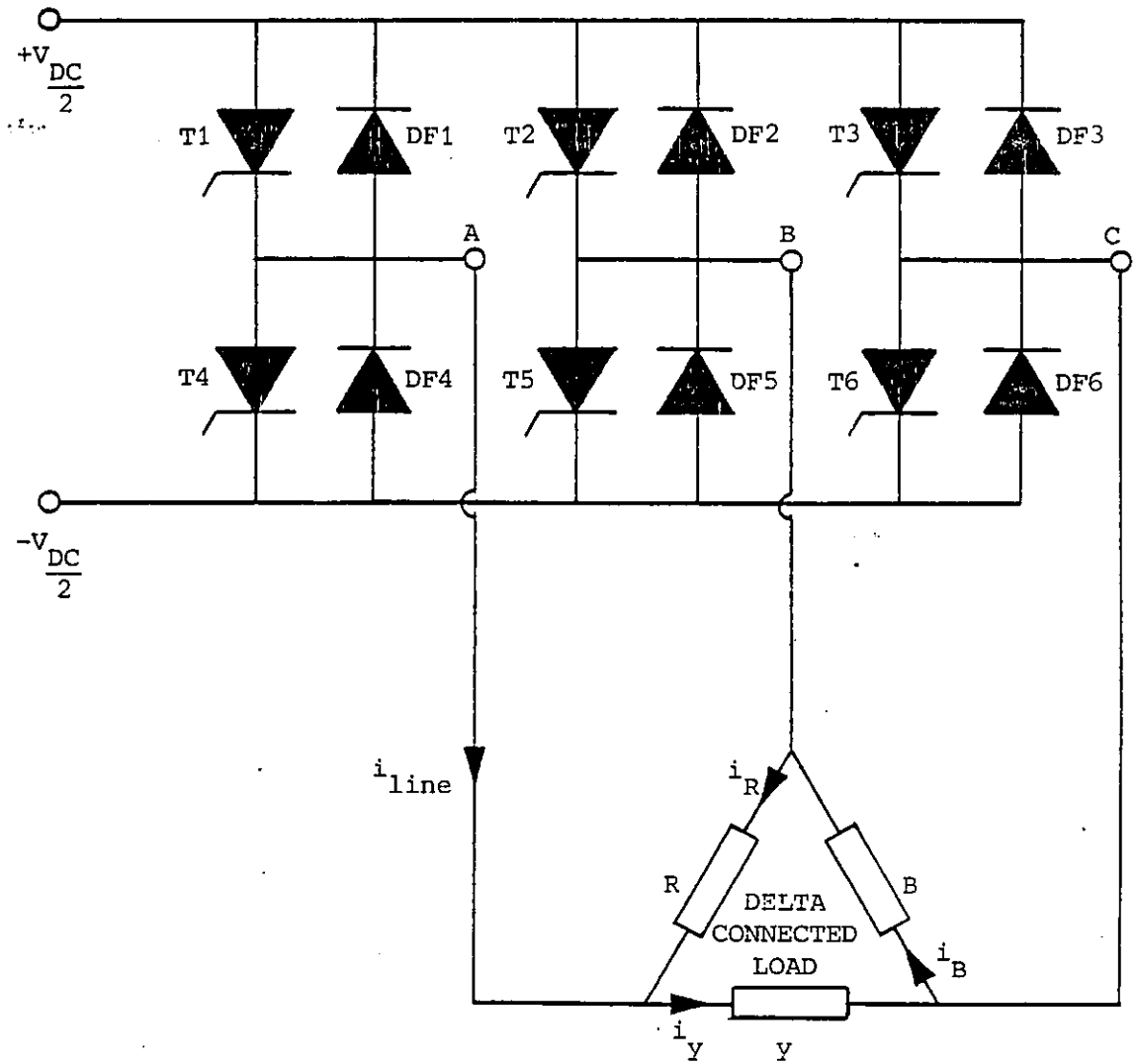


Fig. 2.15 Representation of the 3 phase inverter plus load, showing the main load current carrying devices

main thyristor is now more complicated to calculate; therefore the conduction losses in TM are also excluded from the chopper simulation. With the separation of these two devices, the dc chopper simulation becomes solely a means of determining the energy loss in the commutation circuitry when a thyristor is commutated. The calculation of the conduction losses in the load current carrying devices is examined later in this section.

To further simplify the commutation energy loss calculations, the current in the main thyristor is assumed to remain constant during the commutation process. This is a commonly used assumption and is justified as the time constants of inductive loads, and especially motor loads, are very large compared to the commutation interval. The commutation loss calculations are now independent of the load constants; hence a unique curve, relating energy lost during one commutation cycle to the main thyristor current being commutated, can be derived. The resulting characteristic is shown in Fig. 2.16.

A method must now be developed to calculate the inverter conduction losses. To determine these losses the currents flowing in the devices have to be derived. This can only be achieved if the gating information for one phase can be directly compared with the calculated current flowing through that phase. Only one phase needs to be considered as the power losses in the three phases are assumed to be identical.

The calculation procedure is most easily understood if it is described in the same sequence as it is carried out in the simulation program. A flowchart of the program is given in Fig. 2.17 as a further aid.

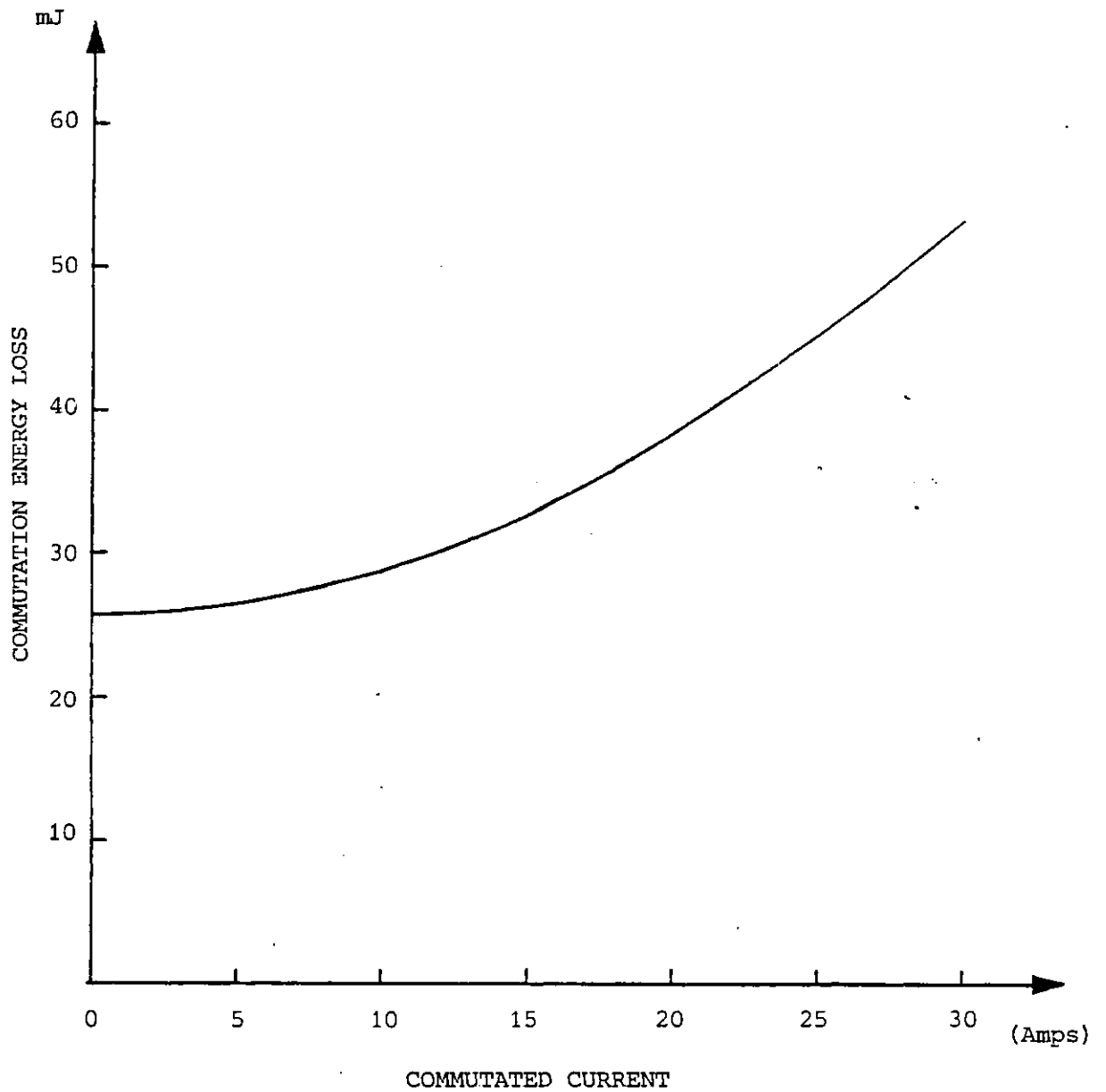


Fig. 2.16 Calculated characteristic relating commutation energy loss to the current being commutated

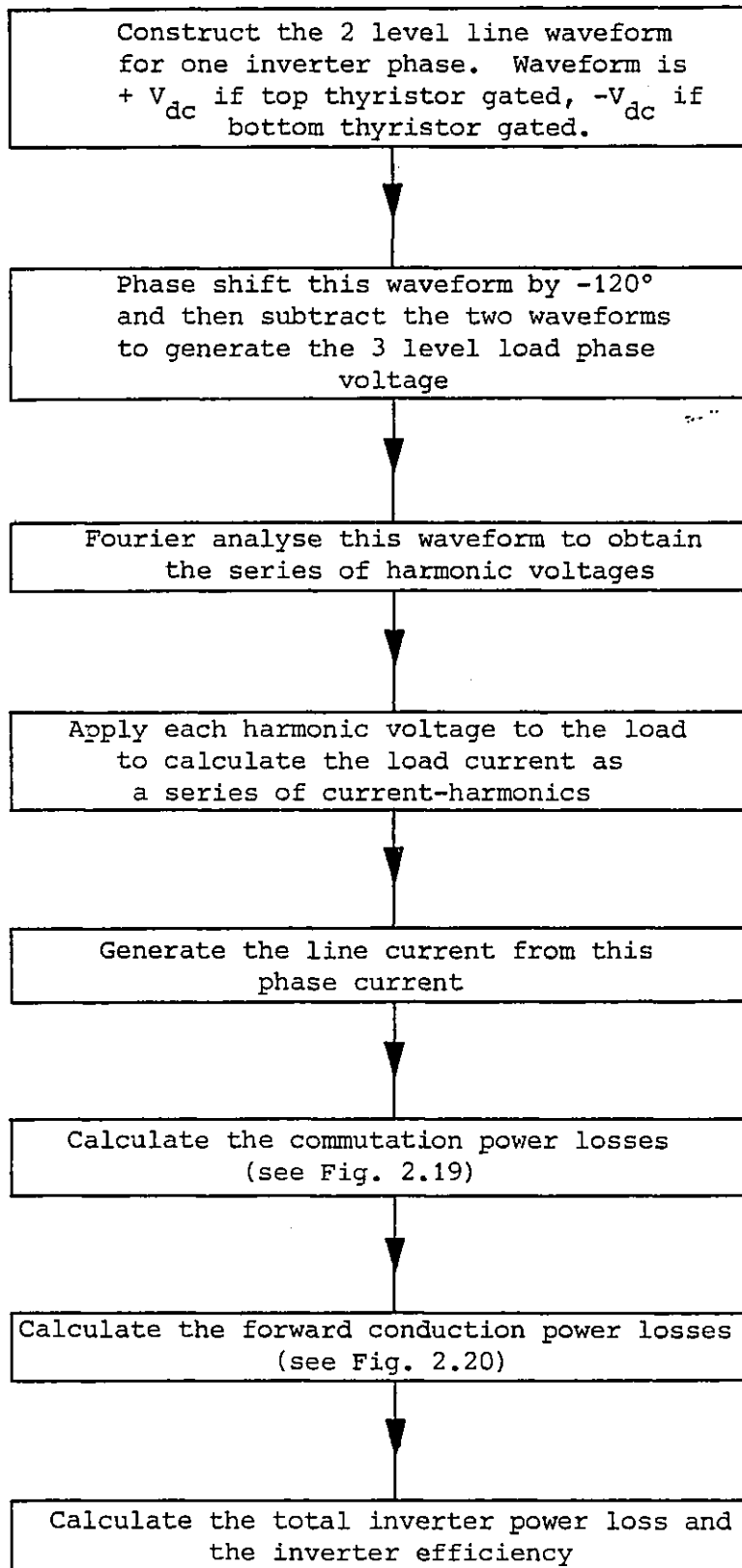


Fig. 2.17 Flow chart outlining the inverter simulation procedure

To calculate the current in one phase of the load, the voltage across the load has to be defined. The thyristor gating information can be used to derive the 2-level line voltage of one phase; a positive level indicating that the top thyristor is being fired, a negative level indicating triggering of the bottom thyristor. By phase shifting this waveform by 120° and subtracting the two waveforms, the load phase voltage can be defined. This procedure is illustrated in Fig. 2.18. The phase current is calculated using a harmonic-series approach because the inverter model will later be used with an induction motor load which is simulated using this technique. The load voltage is expressed as a Fourier Series, using the procedure presented in section 8.1 as:

$$v_{\text{phase}}(t) = \sum_n \hat{V}_n \cos(n\omega t + \theta_n) \quad (2.31)$$

The individual current harmonics are calculated and the principle of superposition used to express the phase current as

$$i_{\text{phase}}(t) = \sum_n \hat{I}_n \cos(n\omega t + \phi_n) \quad (2.32)$$

The inverter line current is then calculated by subtracting the two relevant phase currents to give

$$i_{\text{line}}(t) = \sum_n \hat{I}_n \cos(n\omega t + \phi_n) - \sum_n \hat{I}_n \cos(n(\omega t + \frac{2\pi}{3}) + \phi_n) \quad (2.33)$$

which simplifies to

$$i_{\text{line}}(t) = 2 \sum_n \hat{I}_n \sin(n\pi/3) \sin(n\omega t + \phi_n + n\pi/3) \quad (2.34)$$

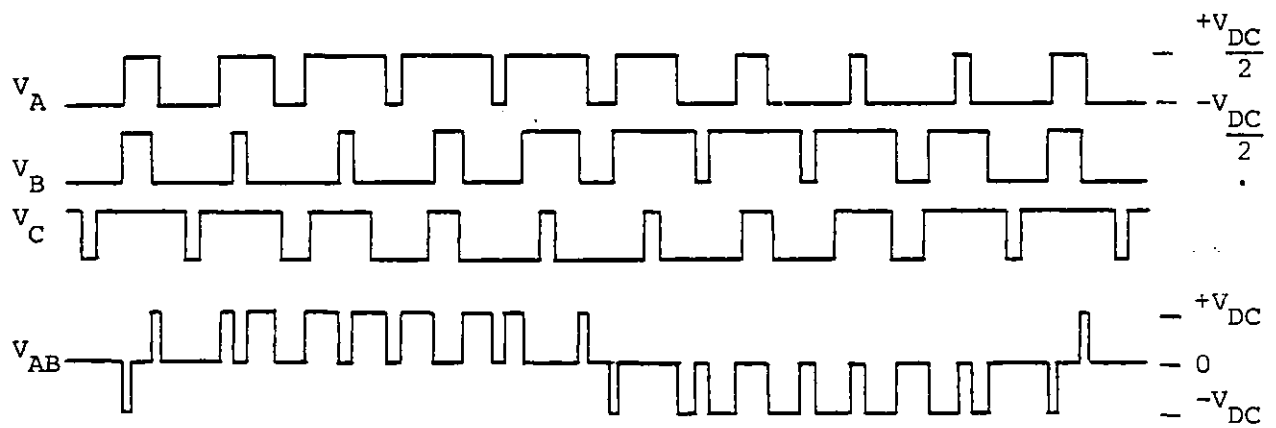


Fig. 2.18 Derivation of load phase voltage from inverter line voltages

The inverter power losses are calculated using this equation in conjunction with the 2-level waveform.

2.4.1 Power Losses due to Commutation: The power losses in the inverter due to commutation are derived by considering the energy loss during one output cycle of one phase. The changes in level in the inverter line waveform correspond to the commutation of one thyristor and the triggering of the complementary thyristor. By substituting these "switching angles" for ωt in Equation 2.34, the current flowing out of an inverter phase at the instant of commutation may be calculated. By considering the direction of current flow at these instants the device in conduction can be ascertained. If the freewheel diode is carrying the current, the current being commutated is assumed to be zero. In this way, the commutation loss at each switching point can be derived from the curve in Fig. 2.16; and so the power loss due to commutation calculated. A flowchart describing this procedure is presented in Fig. 2.19.

2.4.2 Power Losses due to Forward Conduction: The conduction losses are calculated in a similar way. The output cycle is divided into intervals of 0.1 degrees or less and over each interval the energy loss is calculated as $(iV_f + i^2R_f)\Delta t$ where Δt is the interval time. The device carrying the current (either the thyristor or its associated freewheel diode) as determined in section 2.4.1 dictates the values for V_f and R_f . This procedure is carried out over the full 360 degrees of the inverter output cycle to yield a value for the conduction power losses in the inverter. A flowchart of this procedure is shown in Fig. 2.20.

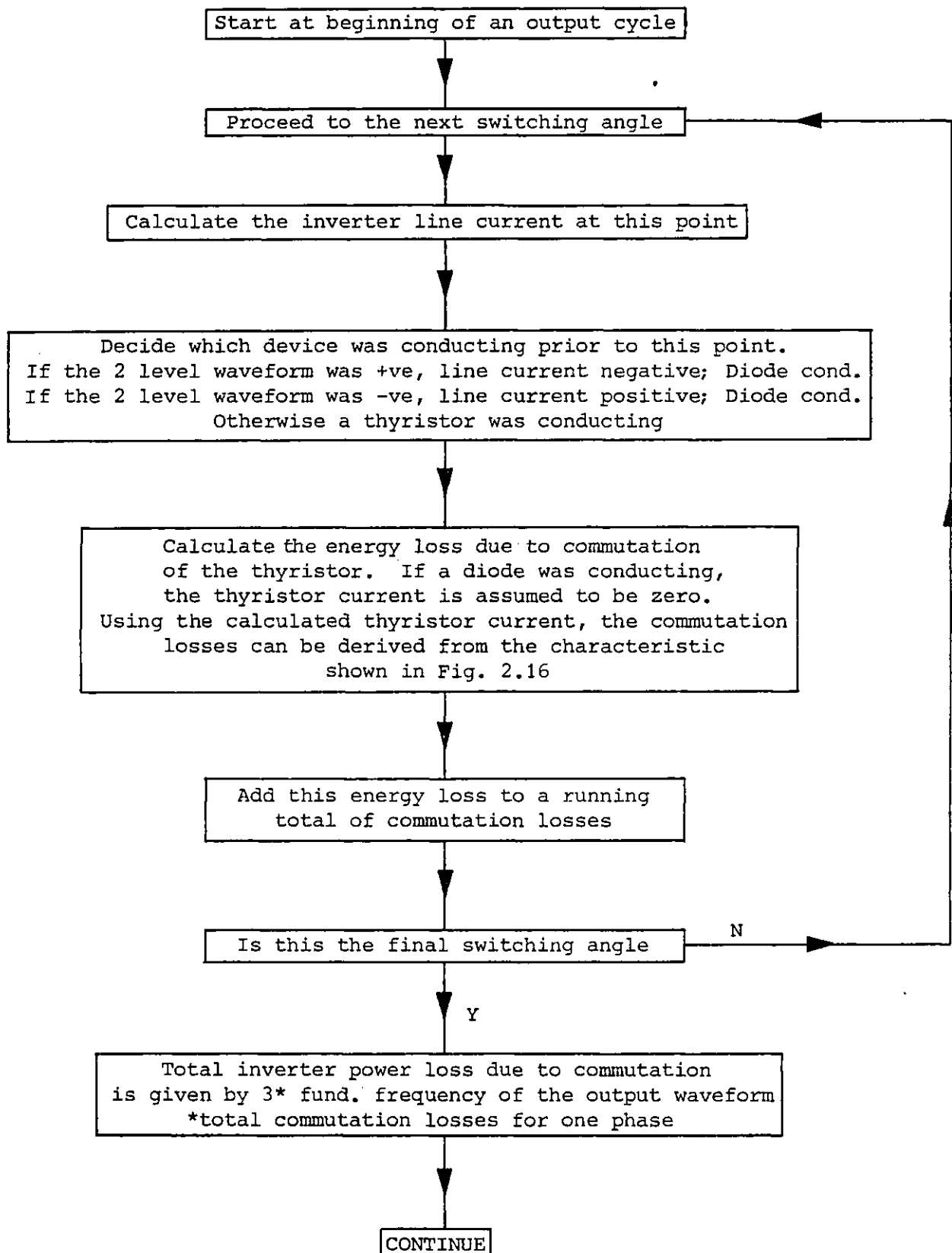


Fig. 2.19 Flow chart outlining the procedure for calculating the inverter losses due to commutation

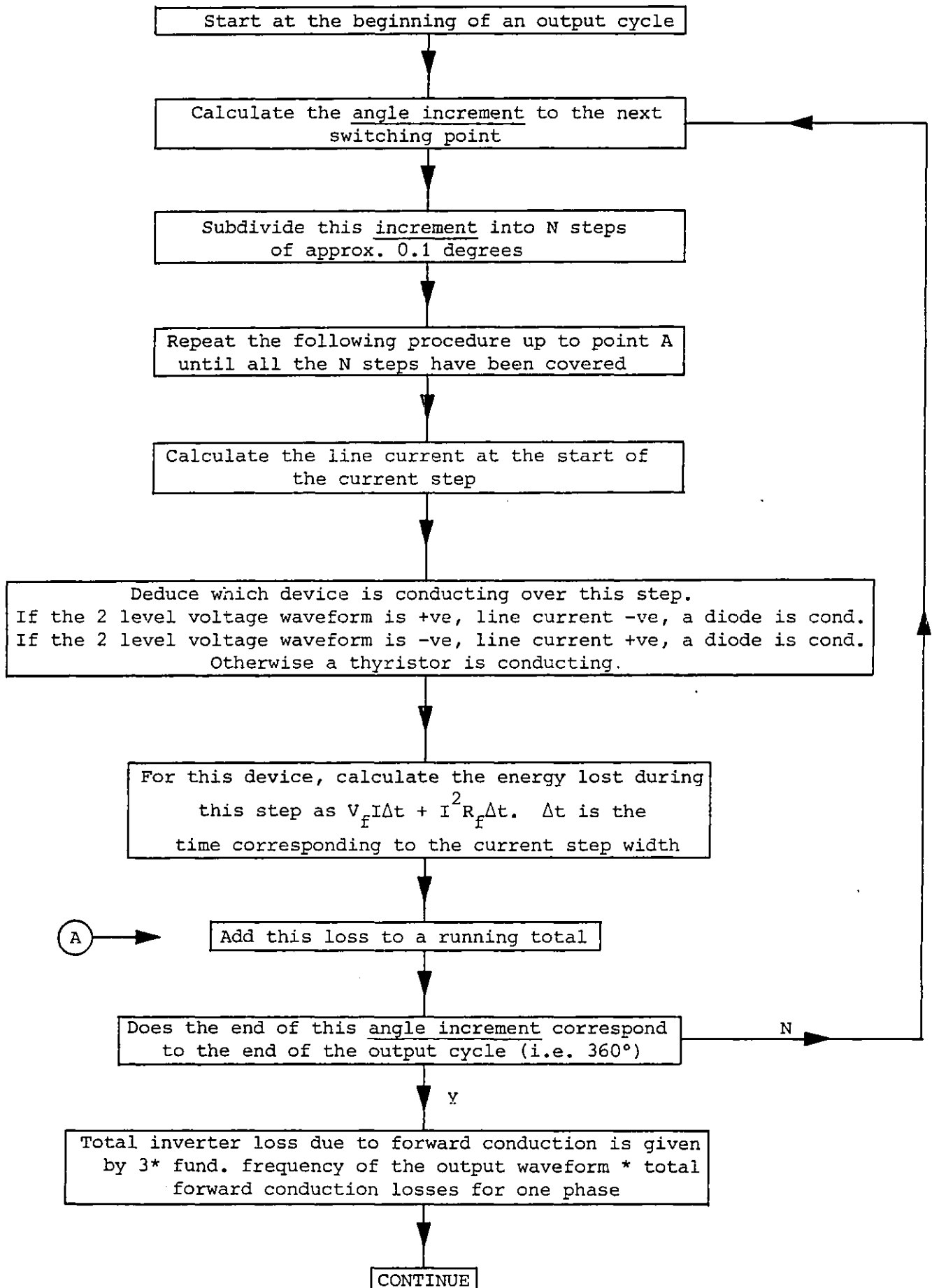


Fig. 2.20 Flow chart outlining the procedure for calculating the inverter losses due to forward conduction

The total power loss in the inverter is calculated as the sum of the conduction losses and the commutation losses.

2.5 Experimental Verification of the Three Phase Inverter Simulation

A direct method of measurement was used in the dc chopper verification which required the operating voltage to be reduced. To verify fully the three phase inverter simulation it was thought important that the operating voltage should be the specified value of 570 V so that the devices could be fully stressed and the losses due to device switching maximised. An indirect method of measurement was adopted for this purpose.

To enable the power losses to be measured accurately at the rated operating point of the inverter, a load of nearly zero power factor was used. The experiments were carried out with the inverter feeding a delta-connected load consisting of three air-cored chokes. The power flowing into the load was derived by separating out the individual load current harmonics and summing the harmonic i^2R losses. The current harmonics were measured using a Hall-effect current probe in conjunction with a microprocessor-based spectrum analyser. The individual choke resistances were measured at the operating temperature using standard techniques. Typically, only harmonics up to the 7th had to be considered, as the inverter controller used a PWM strategy which produced output waveforms of low harmonic content. The load inductance also rapidly attenuated any harmonics.

The power flowing into the inverter was obtained by simply multiplying the dc source voltage and the dc input current. This was a valid method as the dc voltage was found to be sensibly ripple-free when investigated using the spectrum analyser. The dc current was measured

using the current probe together with the spectrum analyser.

Measurements were made at or close to rated kVA at 5 Hz intervals over most of the working range of the inverter. The experimental and computed results are compared in Table 2.2. Again good agreement between experimental and theoretical results is shown.

The experimental measurements did not proceed lower than 10 Hz because the gating information, which had to be obtained experimentally, was not reliable for frequencies below this point. The gating information was obtained using the experimental set-up as shown in Fig..2.21. The two level voltage waveform, measured between the output of an inverter phase and the artificial zero point created by the potential divider, was digitised and stored in the full 8 kbyte memory of the DL912 transient recorder. The digitised waveform was subsequently passed to the LSI-11 computer where the phase gating sequence was calculated.

2.6 Discussion on Device Switching Losses

The experimental results presented in section 2.5 show good agreement with the values calculated using the V-R model. This suggests that the thyristor switching losses and diode reverse-recovery losses in the circuit used for the experimental work were negligible. To a certain extent this result arises from the configuration of the converter circuit used. Diodes D1 and D2 prevent the application of reverse bias to either TA or TM and therefore eliminate turn-off losses in both these thyristors. In addition all diodes used are of the fast-recovery type, with small reverse-recovery losses. Whilst this may be regarded as fortuitous, the converter circuit was of industrial design, using the

OUTPUT FREQUENCY (Hz)	PEAK LINE FUNDAMENTAL COMPONENT OF CURRENT (A)	INVERTER SWITCHING FREQUENCY (kHz)	MEASURED POWER LOSS (W)	CALCULATED POWER LOSS (W) (ignoring turn-on losses)	% ERROR	CALCULATED POWER LOSS (W) (including turn-on losses)	% ERROR
50	9.1	0.9	82.6	80.2	2.9	82.3	0.36
45	9.5	1.17	104.0	101.7	2.2	104.0	0.0
40	10.1	1.36	117.6	117.7	-0.001	120.6	-2.55
35	10.0	1.47	128.7	123.1	4.4	125.8	2.25
30	10.1	1.80	144.6	152.0	-5.1	155.2	-7.33
25	10.1	1.50	131.3	127.4	3.0	130.1	0.91
20	9.9	1.68	143.0	141.0	1.4	144.0	-0.7
15	9.8	1.80	159.0	149.8	5.8	153.2	3.65
10	9.3	1.68	144.5	139.0	3.8	142.5	1.38

Table 2.2 Calculated and measured power losses in a three-phase bridge inverter operating at rated voltage with an inductive load

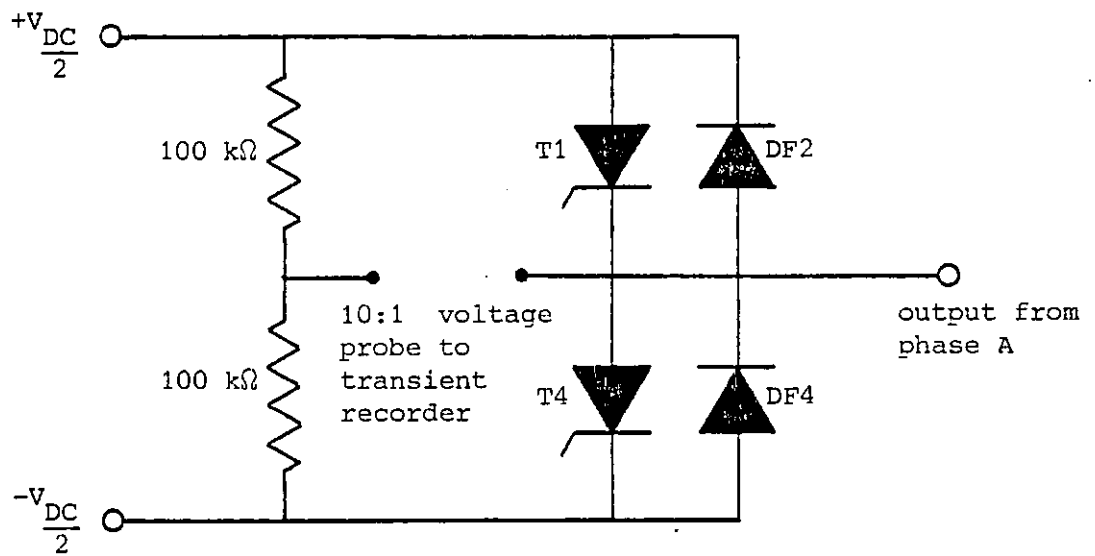


Fig. 2.21 Experimental set-up for deriving the inverter gating information

specified devices and components. Furthermore, reverse-connected diodes and fast-recovery devices are commonly found in other converter circuits, so that the findings are believed to be applicable for a wide range of circuits.

Turn-on losses occur in a thyristor when it is switching on to a current that is rising sharply. The turn-on losses for the auxiliary thyristor TA in the circuit used are small, because the rate of rise of conduction current is here determined by the period of oscillation for the charge-reversal circuit, which is 35 μ s, whilst the turn-on time for TA is of the order of 1 μ s. The main thyristor, on the other hand, turns on to the load current which may be diverted almost instantly from the freewheel diode. An approximate formula for calculating the turn-on energy loss is $\frac{V I t_{ON}}{2}$ (38), where V is the voltage being blocked before turn-on, I is the current at the end of turn-on and t_{ON} is the manufacturer's specified turn-on time. Using the V-R model, it is assumed that switching is instantaneous, but as the blocking voltage before turn-on is known, and the current being diverted from the freewheel diode is also known, the calculation of turn-on loss according to the above prescription is relatively straightforward. The procedure for the prediction of loss in the inverter circuit was accordingly modified to include the turn-on loss approximation, and the power-loss re-calculated. The results of this exercise are included in Table 2.2, in which improved accuracy is seen to have resulted in seven of the nine frequency points examined. It is therefore believed that the simple turn-on loss approximation should be incorporated in the inverter loss calculation wherever appropriate.

CHAPTER THREE

DEVELOPMENT OF THE INDUCTION MOTOR MODEL

3.1 Introduction

In the previous chapter a simulation technique was developed for the three phase inverter. The simulation of the induction motor is described in the present chapter.

In section 3.2, two alternative methods of simulating induction motors operating from non-sinusoidal supplies, the generalised machine, and equivalent circuit methods are presented. The two techniques are then compared and the reasons for choosing the equivalent circuit method for this study are given.

In section 3.3 the procedures for calculating the equivalent circuit parameters are given. Special attention is paid to the problem of saturation in the motor. This results in two characteristics being adopted which allow saturation in the magnetizing and rotor leakage inductances to be taken into account.

In section 3.4, the iterative techniques used to calculate the magnetizing and rotor leakage inductances are outlined.

Finally, in section 3.5, the calculated parameters and the application of the equivalent circuit model are verified experimentally for an induction motor operating from a sinusoidal supply.

3.2 Induction Motor Modelling Techniques

3.2.1 Analysis using a Generalised Machine: An induction motor can be modelled using the two axis representation of a generalised machine

(Fig. 3.1). This method of simulation, when used in conjunction with a time-step procedure, is capable of predicting the motor operation when fed from a non-sinusoidal supply. The two-axis model is well described in the literature (39,40) and will therefore be only briefly described here. The application of the model in the time-stepping simulation of an inverter-fed motor (41,42), however, requires further explanation. For completeness, the two axis equations are presented below.

Electrical quantities are related by

$$\begin{bmatrix} V_D \\ V_Q \\ 0 \\ 0 \end{bmatrix} = \begin{bmatrix} R_1 + L_1 p & 0 & M p & 0 \\ 0 & R_1 + L_1 p & 0 & M p \\ M p & -M \omega_r & R_2 + L_2 p & -L_2 \omega_r \\ M \omega_r & M p & L_2 \omega_r & R_2 + L_2 p \end{bmatrix} \begin{bmatrix} i_D \\ i_Q \\ i_d \\ i_q \end{bmatrix} \quad (3.1)$$

The transformation, relating the d-q axis and 3 phase quantities, is

$$\begin{bmatrix} V_D \\ V_Q \\ i_A \\ i_B \\ i_C \end{bmatrix} = \begin{bmatrix} \sqrt{\frac{3}{2}} & 0 & 0 & 0 & 0 \\ 0 & -\frac{1}{\sqrt{2}} & \frac{1}{\sqrt{2}} & 0 & 0 \\ 0 & 0 & 0 & \sqrt{\frac{2}{3}} & 0 \\ 0 & 0 & 0 & -\frac{1}{\sqrt{6}} & -\frac{1}{\sqrt{2}} \\ 0 & 0 & 0 & -\frac{1}{\sqrt{6}} & \frac{1}{\sqrt{2}} \end{bmatrix} \begin{bmatrix} V_A \\ V_B \\ V_C \\ i_D \\ i_Q \end{bmatrix} \quad (3.2)$$

The electrical torque produced by the motor

$$T_e = PM(i_q i_D - i_d i_Q) \quad (3.3)$$

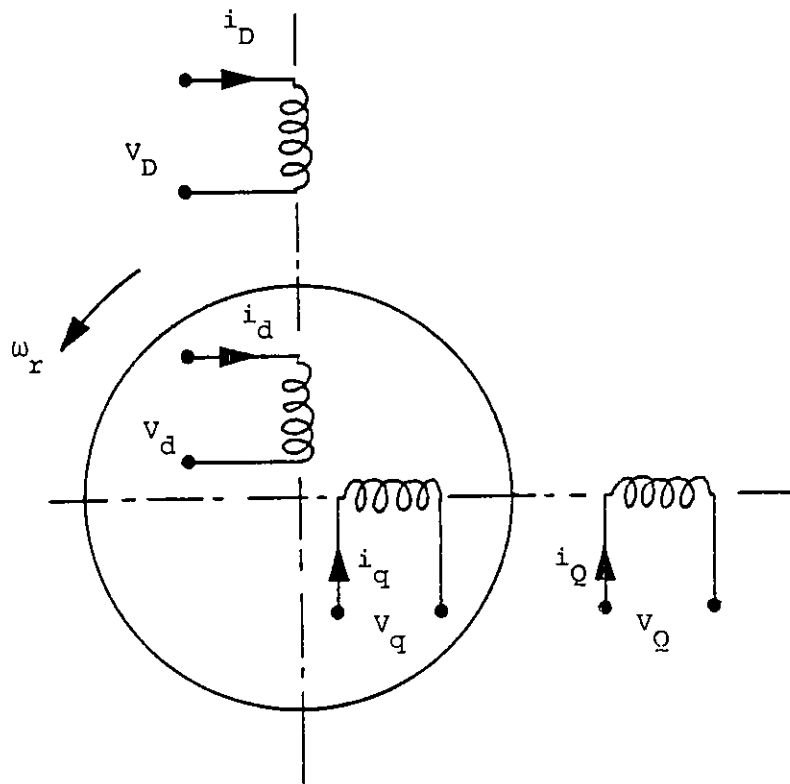


Fig. 3.1 Generalised machine representation of an induction motor

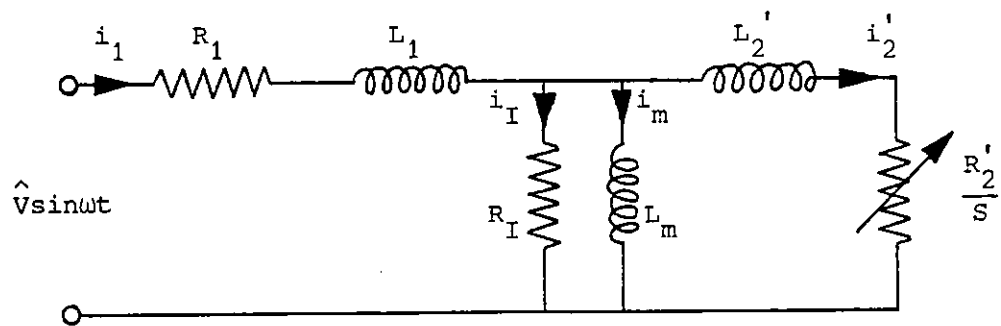


Fig. 3.2 Equivalent circuit representation of an induction motor

The mechanical attributes of the motor are given by

$$T_e = T_m + f\omega_r + J \frac{d\omega_r}{dt} \quad (3.4)$$

Equations 3.1 and 3.4 can be expressed alternatively as

$$p[I] = [L]^{-1}\{[V] - [R][I] - \omega_r[G][I]\} \quad (3.5)$$

and

$$\frac{d\omega_r}{dt} = \frac{1}{J} \{T_e - T_m - f\omega_r\} \quad (3.6)$$

Let us consider a small period of time, referred to as a time step. If the time step is far smaller than the time constant of the motor-load combination being simulated, it is reasonable to assume that the speed will remain sensibly constant over the time step. Using this assumption, together with the values for i_D , i_Q , T_e , ω_r at the beginning of the time step, the values of these same variables at the end of the interval can be obtained by numerical integration of Equations 3.5 and 3.6. The final values for one time step now become the initial values for the next. This procedure may be repeated until the desired solution period is completed.

The terminal voltages of motors fed by PWM inverters (Fig. 2.18) are never indeterminate and may be considered as a sequence of constant voltage regions. The time-step durations are allowed to vary within the limits set by the accuracy required from the numerical integration, so that the voltage is constant over each interval. Non-linear effects, such as saturation, may be included by allowing the model parameters to vary from interval to interval, the values being obtained from data stored in look-up tables. This data may be obtained experimentally or

calculated using, for example, numerical field solution techniques. Skin effect can also be incorporated in the model, at the expense of complex and time consuming additions to the basic simulation technique.

Using the procedure described above, the motor operation may be simulated during transient operations, such as direct on-line starting or step changes in load. Examples of results obtained using this method are given by Bowes (43) in a recent publication, as well as by several other authors (44,45).

Considerable savings in computer time can be made if the motor speed is assumed to remain constant throughout the entire simulation. Under this condition, the derivative of ω_r (Equation 3.6) is equated to zero enabling Equation 3.5 to be solved algebraically over a constant voltage region (46). This, in effect, extends the time-steps to intervals of constant voltage. Using this procedure, the simulation is constrained to steady-state operation of the motor.

3.2.2 Analysis using Equivalent Circuits: An alternative technique for simulating an inverter-fed motor uses the standard equivalent circuit (15,47,48,49) as shown in Fig. 3.2.

The voltage waveform produced by an inverter, as shown in Fig. 2.18, can be Fourier analysed and thus be represented as a series of voltage time harmonics. The derivation of the harmonic series is presented in section 8.1. The resulting description of the waveform is

$$v(t) = \sum_n \hat{V}_n \cos(n\omega t + \theta_n) \quad (3.7)$$

where n is the harmonic number

\hat{V}_n is the peak voltage of the n^{th} harmonic

θ_n is the phase angle of the n^{th} harmonic

In this way, the voltage can be considered as a group of series connected sinusoidal voltage sources as shown in Fig. 3.3. Each source is assumed to have zero impedance and a unique frequency, voltage amplitude and phase. As each voltage source is independent of the rest, the response to a particular harmonic frequency may be calculated by considering solely that harmonic. The single equivalent circuit of Fig. 3.3 may therefore be resolved into a set of similar circuits, one for each voltage time-harmonic produced by the inverter, as shown in Fig. 3.4.

If all non-linear effects are initially neglected, the n^{th} harmonic equivalent circuit is derived from the fundamental circuit simply by multiplying the circuit reactances by n . The n^{th} time-harmonic slip, s_n , is calculated from the fundamental-frequency slip, taking into account the direction in which the n^{th} time-harmonic field rotates. Thus,

$$s_n = \frac{(n-1) + s}{n} \quad \text{for positive sequence harmonics; (3.8)}$$

i.e..where $n = 3k+1$

$$s_n = \frac{(n+1) - s}{n} \quad \text{for negative sequence harmonics; (3.9)}$$

i.e. where $n = 3k-1$

Using this method, the input current into each individual harmonic circuit is calculated as

$$i_n(t) = \hat{I}_n \cos(n\omega t + \phi_n) \quad (3.10)$$

If saturation is temporarily ignored, the response of the motor to the time-harmonics is linear so the principle of superposition may be used

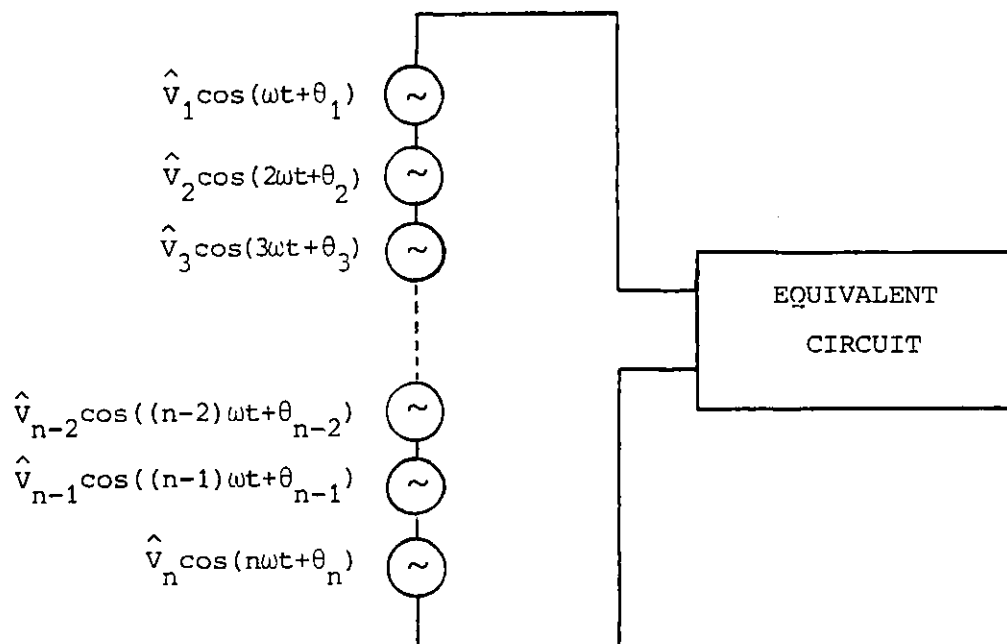


Fig. 3.3 Representation of inverter output voltage as a series of harmonic voltage sources

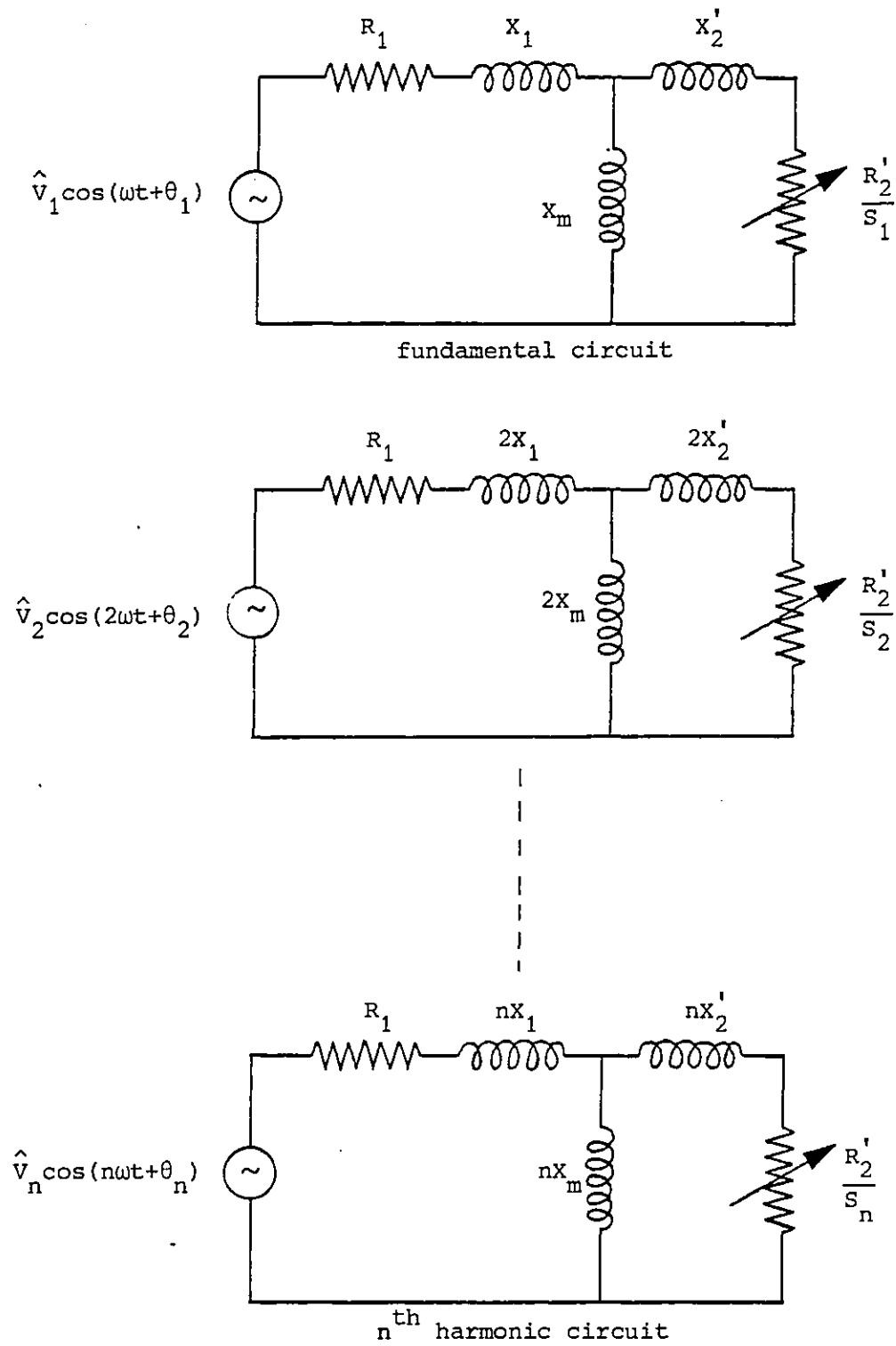


Fig. 3.4 Principle of superposition of harmonic equivalent circuits

to derive the total response of the motor as

$$i(t) = \sum_n \hat{I}_n \cos(n\omega t + \phi_n) \quad (3.11)$$

The steady-state torque produced by the motor is obtained in a similar manner from the torques calculated for the harmonic circuits

$$T_{\text{total}} = \sum_n T_n \quad (3.12)$$

This method assumes the motor speed to be constant, thereby leading to a steady-state simulation. Saturation may be included by modifying circuit parameters, as in the two-axis approach. The inclusion of saturation causes the motor response to be non-linear. However, as a simplifying assumption, the principle of superposition is still employed. Skin effect can be accounted for by multiplying the rotor parameters in each harmonic equivalent circuit by the correction factors, described by Alger (50), for that frequency.

3.2.3 Choice of Modelling Technique: The major difference between the two techniques outlined in the previous sections, is that speed transients can be dealt with using the 2-axis approach, whereas the equivalent circuit simulation is restricted to constant speed. This study involves simulating a motor operating on PWM waveforms in which the low-order harmonics are insignificant. Assuming that no low order pulsating torques occur and that the motor is driving a high inertia load, the motor speed can be considered to be reasonably constant. With the principle advantage of transient analysis using the 2-axis approach being removed, the two techniques can be compared directly.

The effects of saturation may be incorporated in either technique in much the same way via the use of look-up tables. Some advantage is

gained in the equivalent circuit approach, however, because the look-up table is accessed fewer times than in the two-axis method, where the look-up table is accessed once for every time interval calculation.

Properties of the motor which vary with frequency are more easily dealt with in the equivalent circuit method which gives a solution in the frequency domain. The two-axis method, on the other hand, operates in the time domain. A commonly included frequency dependent property is deep-bar effect, in which current becomes unevenly distributed in the rotor bars. Deep-bar effect is incorporated in an equivalent circuit solution by multiplying the rotor branch parameters in each harmonic circuit by the correction factor relevant to that frequency.

Deep-bar effect is less readily accommodated in a two-axis model. One possible technique is to calculate a slip-frequency, from the instantaneous rotor speed together with a knowledge of the fundamental supply frequency and the number of poles. Using the slip-frequency, global skin effect correction factors may be derived, as in the equivalent circuit method. The success of this approach is dependent on the relative magnitudes of time-harmonic currents in the rotor, for which the global correction factors are inappropriate.

Space harmonics, too, may be included in the equivalent circuit with comparative ease. In this instance, however, the effects of space harmonics are ignored, as the author's intention is to concentrate on standard balanced three phase machines in which space harmonic fields assume a less significant role.

To sum up, the principle advantage of two-axis theory is that it can model rotor speed transients, an advantage which is not applicable in the present constant-speed study. The equivalent circuit, on the other hand, has a more realistic approach to skin effect, is simple to program and is far quicker to execute. The equivalent circuit method was therefore adopted in this work.

3.3 The Induction Motor Equivalent Circuit

3.3.1 Test Motor Details: The experimental work in this study was carried out using a 4 kW, 3 phase cage induction motor. Details of the motor are given in Table 3.1, and dimensional drawings of the stator and rotor slots are given in Figs. 3.5 and 3.6.

The stator windings were concentrically wound to produce a 4 pole delta-connected machine with six series coils per phase. The rotor was of closed slot construction with a cast aluminium cage. The aluminium alloy used was not specified by the manufacturer, but correlation with test data suggested it was most probably pure aluminium - LM0.

3.3.2 Magnetising Inductance: The magnetising inductance of the motor was calculated using the standard formula given in Equation 3.13, together with the drawings and winding details supplied by the manufacturer. The motor is initially assumed to be unsaturated.

$$L_m = \frac{3w'\mu_0 d}{\pi g'} \left(\frac{N_{ph} k_{\omega 1}}{p} \right)^2 \quad (3.13)$$

where $k_{\omega 1}$ is the fundamental winding factor for the motor and g' is

Rated Output Power	4 kW
Rated Line Voltage	415 V _{rms}
Rated Output Torque	26 Nm
Number of Poles	4
Number of Stator Slots	36
Number of Rotor Slots	28
Number of Stator Coils/slot	1
Number of Turns/Stator Coil	57
Rotor Bar Skew (fraction of a slot pitch)	0.62
Resistivity of Rotor Bar Aluminium at 20°C	$3.0175 \times 10^{-8} \Omega\text{-m}$
Assumed Operating Temperature	75°C
Carter Corrected Airgap Width	0.518 mm
Mean Diameter of Airgap	130.0 mm
Effective Machine Length	83.5 mm

Table 3.1 Summary of Test Motor Details

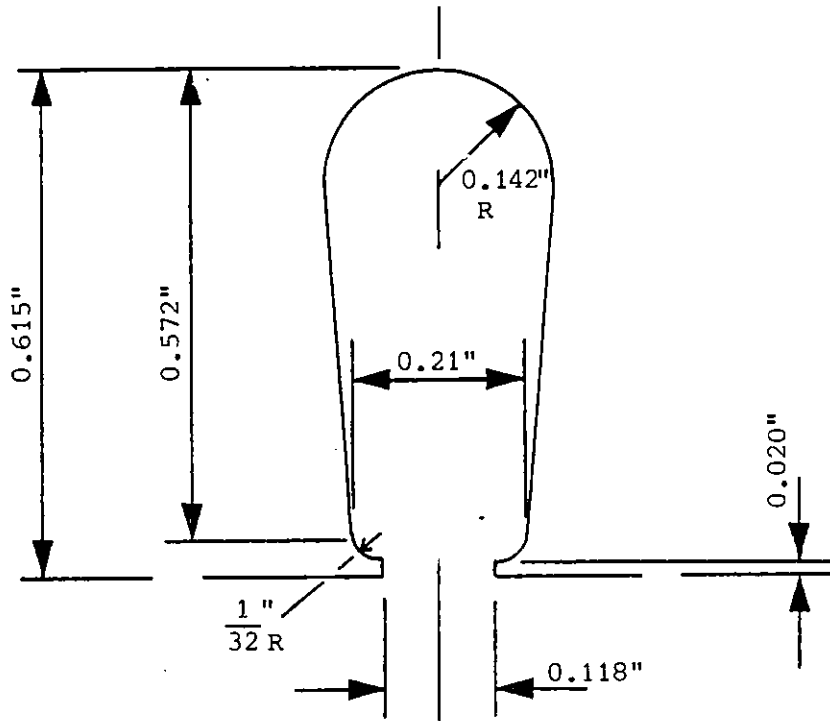


Fig. 3.5 Dimensioned drawing of the test motor stator slots

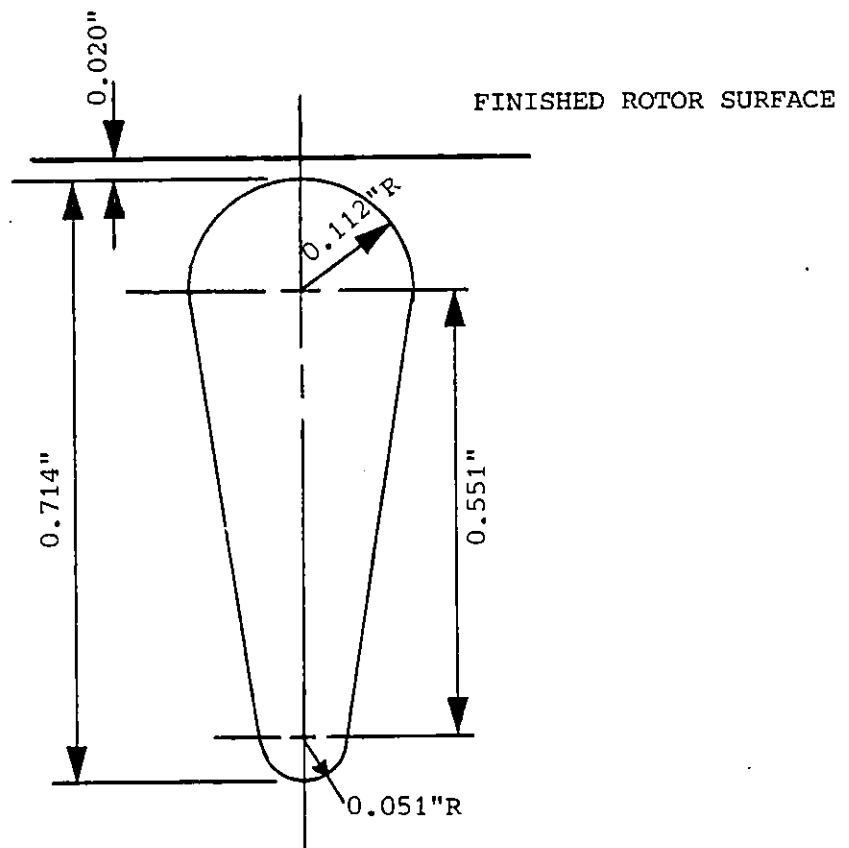


Fig. 3.6 Dimensioned drawing of the test motor rotor slots

the Carter's air gap length. The calculation of these parameters is covered in most standard tests dealing with electrical machine theory.

The calculated value of L_m for the test motor was 643 mH, which differed considerably from the measured value at rated voltage. This suggested that the motor might suffer from the effects of saturation. A series of synchronous speed tests at different line voltages was therefore carried out and the variation of magnetising inductance with magnetising current was determined. The characteristic so obtained for the test motor is shown in Fig. 3.7.

In order to include saturation effects in the equivalent circuit model, the magnetisation characteristic was linearised (Fig. 3.7) and used in an iterative procedure (section 3.4) to calculate the magnetising inductance at specific operating points.

3.3.3 Iron Loss Resistance: The iron loss resistance was also obtained from synchronous speed tests at several operating voltages. An average value of 1600 ohms was adopted. This corresponds to a fixed iron loss of 108 Watts at rated voltage and frequency, being equivalent to approximately 2.6% of the machine's rated output power.

The presence of the iron loss resistance, therefore, has little effect on the calculated operating characteristics of the motor. In Chapter 4, the inverter and motor models are combined, an operation which necessitates the accurate calculation of the waveform for the motor line current. If the iron loss resistance is ignored, the current waveforms were found to have a noticeable phase error close to synchronous speed.

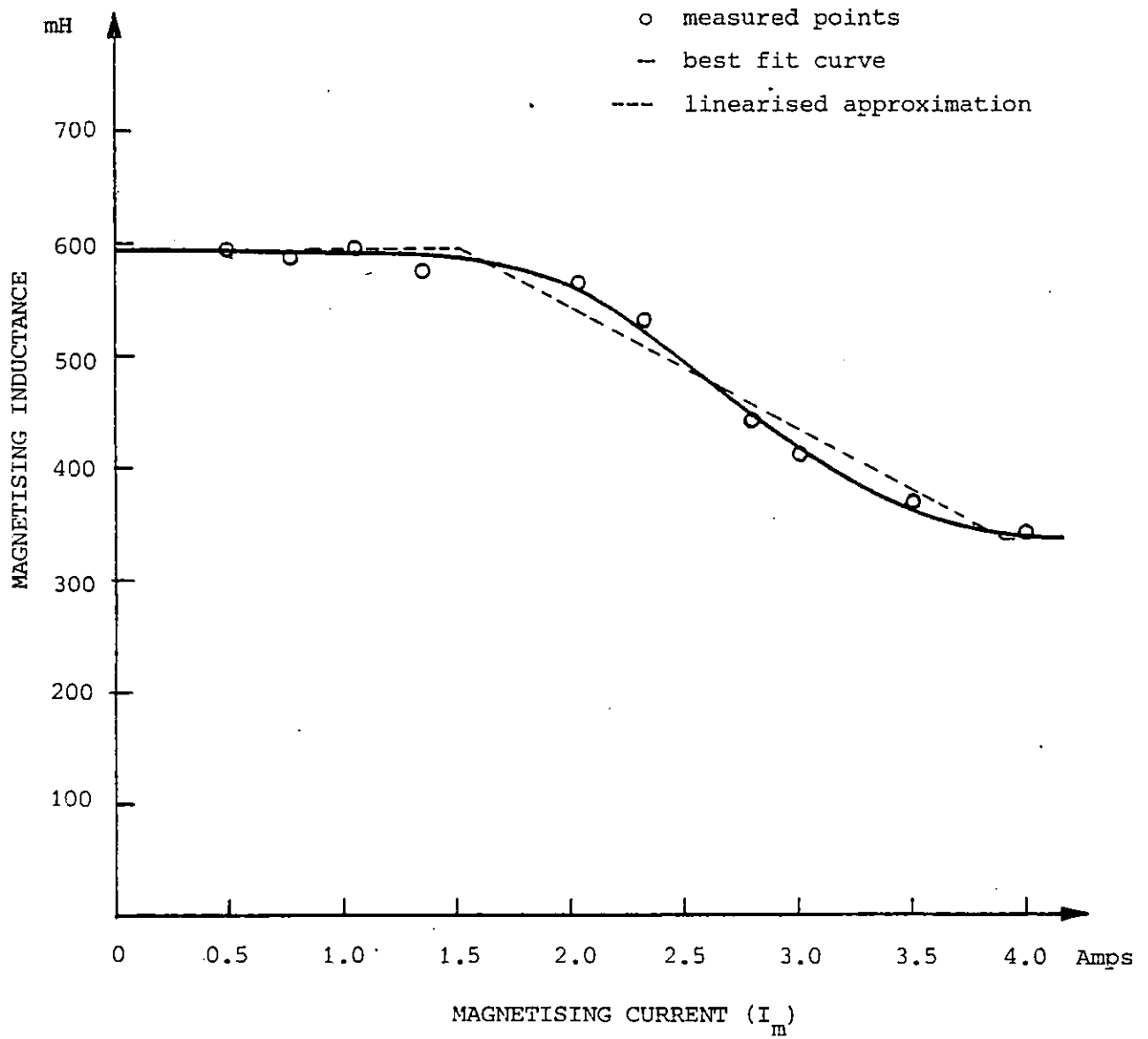


Fig. 3.7 Magnetisation characteristic for the test motor

3.3.4 Stator Resistance: The stator resistance was obtained by direct measurement using a Kelvin bridge. The measurements were made at 20°C and were converted to correspond with the assumed operating temperature of 75°C.

$$R_1(t_2) = R_1(t_1)\{1 + \alpha_t(t_2 - t_1)\} \quad (3.14)$$

where t_1 is the base temperature at which the resistance is known and t_2 is the temperature at which the resistance is required. α_t is the material temperature coefficient and is usually given as 0.0039.

The temperature corrected stator resistance was calculated to be 6.1 Ω .

3.3.5 Stator Leakage Inductance: The stator leakage inductance is notionally composed of several components, these being the slot, end winding and harmonic leakages.

The slot leakage inductance can be theoretically calculated for any shape of slot. The more common method adopted uses standard curves which relate the permeance of the slot to its geometrical properties. These curves are available for most slot types, examples of which are given by Veinott (51) and Alger (50). The value of slot permeance λ_s for the stator slot shown in Fig. 3.5, calculated using the characteristic on page 328 of Veinott (51) is 1.19. The slot leakage inductance is then given by

$$L_{\text{SLOT}} = w' \mu_0 \lambda_s \frac{12}{N_s} N_{\text{ph}}^2 \quad (3.15)$$

$$= 4.62 \text{ mH.}$$

The end winding leakage is less amenable to calculation, as it depends not only on the geometry of the end turns but also on the proximity of iron surfaces, such as those presented by the end bells. Numerical techniques may be employed to calculate the end-winding leakage inductance accurately allowing for the presence of iron. However, empirical formulae, for instance those given by Say (52) and Alger (50) are more commonly used. Because of the approximate nature of these formulae the average of the two methods was chosen.

From Alger

$$L_{EW} = \frac{7mN_{ph}^2 d}{2\pi p 10^6} (k_{pa} - 0.3) \quad (3.16)$$

$$= 9.43 \text{ mH}$$

and by Say

$$L_{EW} = \frac{12\mu_0 N_{ph}^2 k_{ps}^Y}{2\pi p} \quad (3.17)$$

$$= 15.19 \text{ mH}$$

The value for the end-winding leakage inductance adopted was 12.31 mH.

The final component of stator leakage inductance is the harmonic leakage inductance. The effect of space harmonic fields in the airgap can be represented by including harmonic branches in the equivalent circuit, as shown in Fig. 3.8. If the currents in the rotor cage are assumed to be induced solely by the fundamental field, the space harmonic branches consist solely of the magnetising reactances, which may be

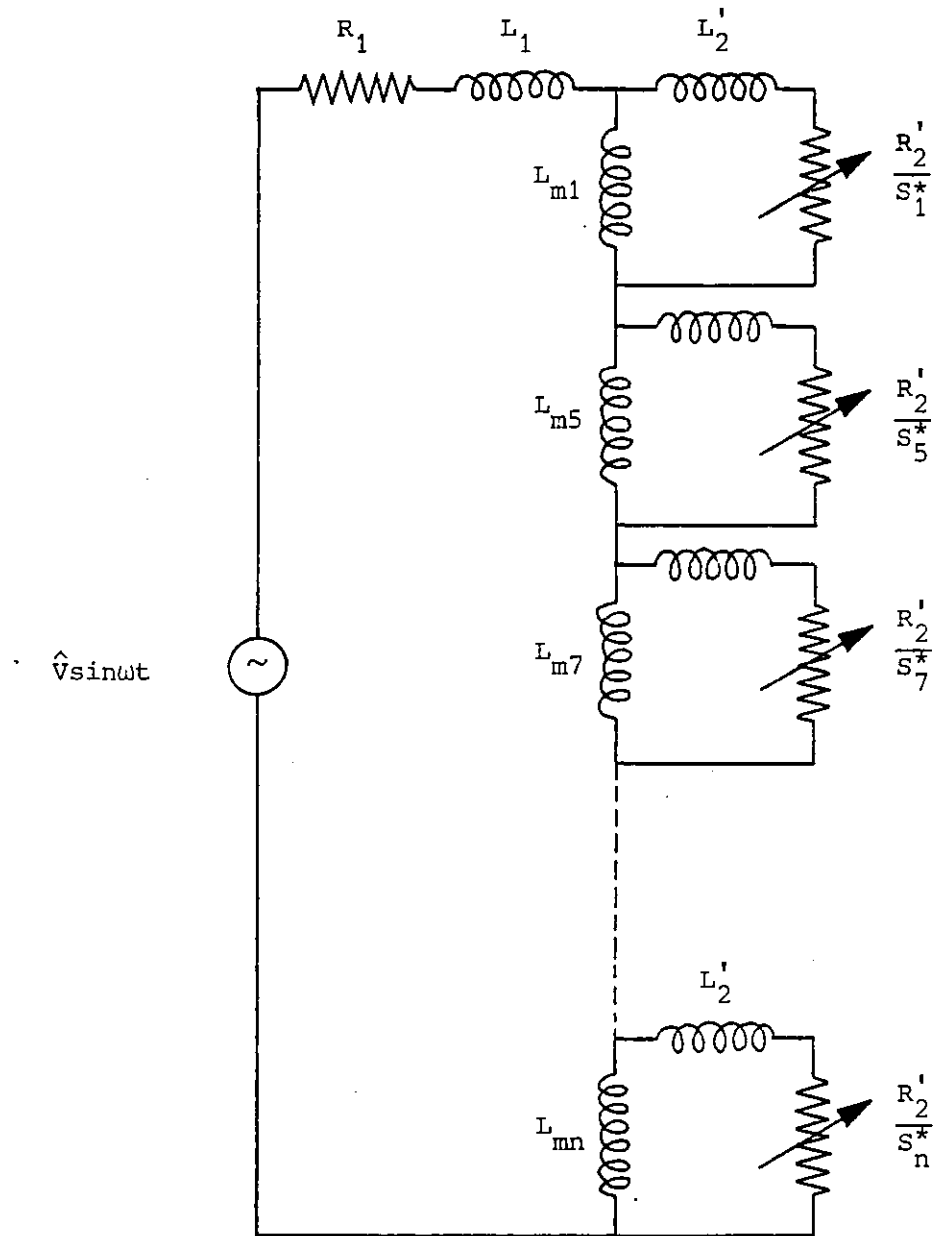


Fig. 3.8 Induction motor equivalent circuit, including space-harmonic airgap fields

summed and added to the stator leakage reactance. The harmonic leakage inductance is therefore obtained as the sum of the harmonic magnetizing inductances

$$L_{HARM} = L_m \left\{ \left[\frac{k_{\omega 5}}{5k_{\omega 1}} \right]^2 + \left[\frac{k_{\omega 7}}{7k_{\omega 1}} \right]^2 + \left[\frac{k_{\omega 11}}{11k_{\omega 1}} \right]^2 + \dots \right\} \quad (3.18)$$

$$= 2.08 \times 10^{-3} L_m.$$

As the value of L_m varies due to saturation (section 3.3.2), L_{HARM} cannot be assigned a fixed value and so the stator leakage inductance,

$$L_1 = L_{SLOT} + L_{EW} + L_{HARM} \quad (3.19)$$

is given by

$$L_1 = (16.93 + 2.08 \times 10^{-3} L_m) \text{ mH} \quad (3.20)$$

3.3.6 Rotor Resistance: The rotor resistance is dependent upon two components, rotor bar resistance (R_{bar}) and end-ring resistance (R_{ring}). The effective rotor resistance per bar is calculated as (50)

$$R_2 = R_{bar} \phi + \frac{R_{ring}}{2N_R \sin^2 \left(\frac{\pi p}{N_R} \right)} \quad (3.21)$$

The values for R_{bar} and R_{ring} , calculated from the cage dimensions and corrected for a temperature of 75°C, were 41.7 $\mu\Omega$ and 28.1 $\mu\Omega$ respectively.

The rotor slots in the test motor were of the fully closed type. The rotor slot leakage inductance is therefore dominated by the inductance due to the flux through the slot bridge. Because of this, the inductance seen by a current element may be regarded as essentially independent of its radial position in the slot. The distribution of current in the slot was therefore assumed to be independent of frequency and no deep bar effect correction was made to the rotor bar resistance or leakage reactance (section 3.3.7).

The correction factor Φ is therefore removed from Equation 3.21 which is now expressed as

$$R_2 = R_{\text{bar}} + \frac{R_{\text{ring}}}{2N_R \sin^2 \left(\frac{\pi p}{N_R} \right)} \quad (3.22)$$

The referred rotor resistance is given by

$$R_2' = \frac{12}{N_R} N_{\text{ph}}^2 k_{\omega 1}^2 R_2 \quad (3.23)$$

For the test motor, R_2' at 20°C = 3.22 Ω .

3.3.7 Rotor Leakage Inductance: The closed rotor slot construction, employed in the test motor, causes difficulty in the calculation of the rotor leakage inductance because the iron in the slot bridge is subject to saturation. The rotor leakage inductance consists of several components; namely the slot, zig-zag and bridge leakage inductances. The rotor slot may be notionally split into two section, as shown in Fig. 3.9.

The permeance of the bottom portion of the slot, λ_{SB} , is calculated in a similar manner to the stator slot permeance (section 3.3.5) using

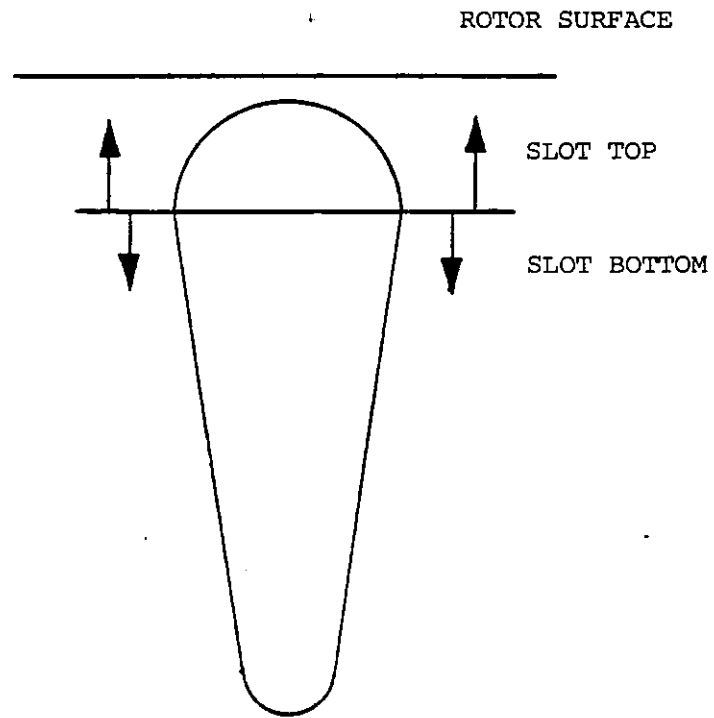


Fig. 3.9 Notional separation of the rotor slot into 2 sections

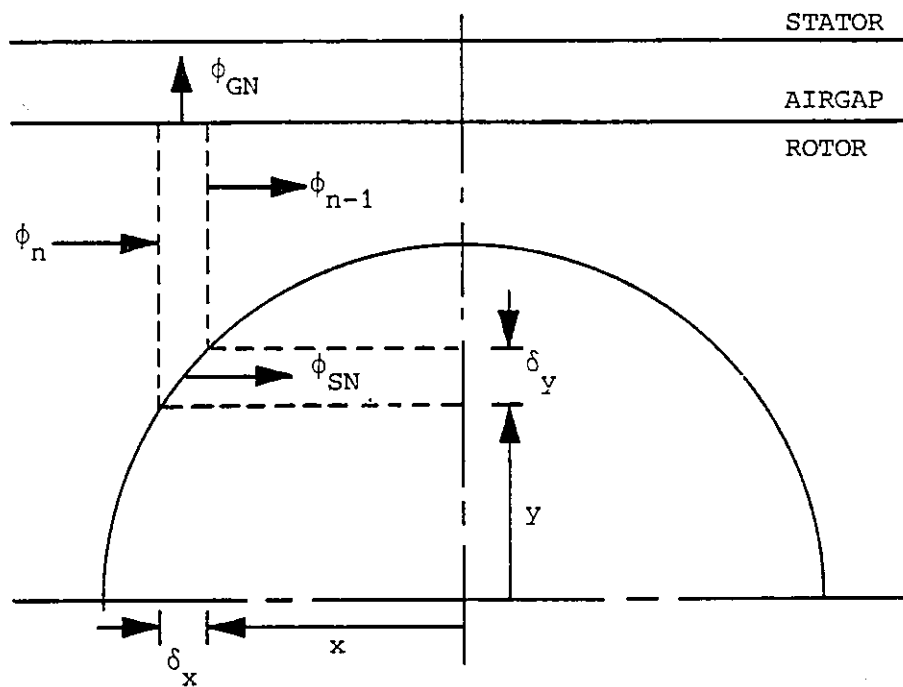


Fig. 3.10 Typical strip for the rotor slot bridge

standard curves (Veinott (51)). The leakage inductance for the slot bottom is given by

$$\begin{aligned} L_{SB} &= \mu_0 w' \lambda_{SB} \\ &= 9.61 \times 10^{-8} \text{ H} \end{aligned} \quad (3.24)$$

The bridge, zig-zag and slot top leakage inductances are calculated as one inductance using the method developed by Birch and Butler (53) outlined below.

The slot bridge is divided into several strips of which a typical strip is shown in Fig. 3.10. The flux entering this strip, ϕ_n , is related to that leaving it, ϕ_{n-1} , by

$$\phi_n = \phi_{n-1} + \phi_{SN} + \phi_{GN} \quad (3.25)$$

where ϕ_{SN} and ϕ_{GN} are the fluxes which cross the slot top and the air-gap respectively. These fluxes are calculated from:

$$\phi_{SN} = \lambda_{SN} F_{SN} \quad (3.26)$$

$$\phi_{GN} = \lambda_{GN} F_{GN} \quad (3.27)$$

F_{SN} and F_{GN} are the mmf's acting across the slot top and the air-gap. The method for determining these mmf's is presented in section 8.2.

The flux density at the n^{th} section

$$B_n = \frac{\phi_n}{a_n} \quad (3.28)$$

where a_n is the cross sectional area of the bridge at the n^{th} strip. A B-H characteristic for the lamination material together with B_n is used to calculate the mmf acting at the n^{th} section (H_n). By estimating the flux density, B_0 , at the bridge centre and calculating a value for H_n for every section, the mmf drop across the bridge can be determined by summing the mmf drops across the individual strips. Assuming all iron outside the bridge is infinitely permeable, the mmf drop should be equal to the rotor bar current. Repeated estimates for B_0 are made until this equality is satisfied.

For a rotor bar current, I_{bar} , the flux entering the first (leftmost) strip can be calculated and the total leakage inductance for the slot top further calculated.

$$L_{\text{ST}} = \frac{\phi_1}{I_{\text{bar}}} \quad (3.29)$$

A curve relating the slot top leakage inductance to the rotor bar current was derived (Fig. 3.11) in this manner and used in an iterative procedure (section 3.4) to calculate the slot top leakage inductance at specific operating points. The rotor leakage inductance is expressed as

$$L_2 = L_{\text{ST}} + L_{\text{SB}} \quad (3.30)$$

A deep bar correction was not included in these calculations, as discussed in the previous section.

The equivalent circuit parameter L_2' , the rotor inductance referred to the stator is calculated as

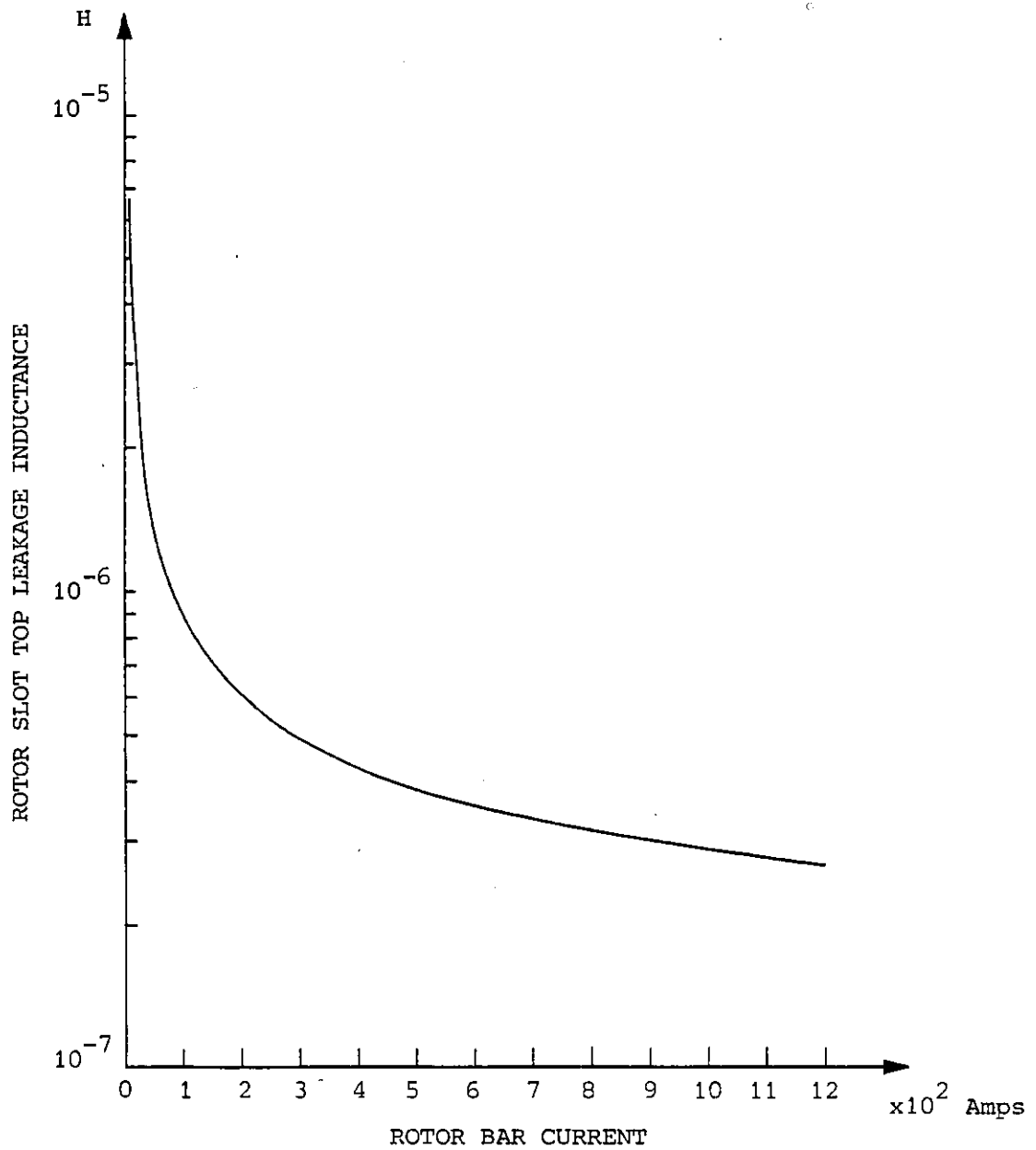


Fig. 3.11 Calculated characteristic relating the rotor slot top leakage inductance to the rotor bar current

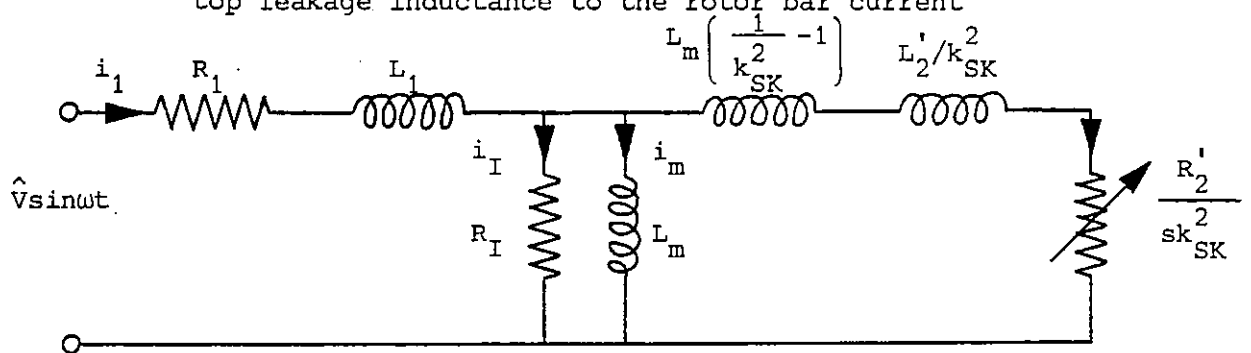


Fig. 3.12 Equivalent circuit after modification to include skew effects

$$L_2' = \frac{12}{N_R} N_{ph}^2 K_{\omega 1}^2 L_2 \quad (3.31)$$

The rotor bar current is derived from the equivalent circuit current I_2' , as

$$I_{bar} = \frac{6}{N_R} N_{ph} K_{\omega 1} I_2' \quad (3.32)$$

3.3.8 Effect of Rotor Skew: The effects of rotor skew are taken into account by modifying the equivalent circuit according to proposals presented by Butler and Birch (54). The modified equivalent circuit shown in Fig. 3.12 was shown by these authors to yield the correct terminal and internal relationships. The circuit modifications were later endorsed by Williamson and Smith (55) who came to the same conclusions via a completely different approach. The equivalent circuit described in the preceding sections was therefore modified to incorporate rotor skew according to these ideas.

The modifications to the equivalent circuit are two-fold. Firstly, the referred rotor components are divided by k_{SK}^2 where

$$k_{SK} = \frac{\sin(sp\pi/N_R)}{sp\pi/N_R} \quad (3.33)$$

s is the rotor skew expressed as a fraction of one rotor slot pitch. Secondly, the referred rotor leakage inductance is increased by the addition of

$$L_{SKEW} = \left\{ \frac{1}{k_{SK}^2} - 1 \right\} L_m \quad (3.34)$$

3.4. Use of the Equivalent Circuit

Conventional use of the equivalent circuit involves determination of torque, power and current for a specified slip. In this study, however, the current, power and rotor speed are required for a specified torque. In order to accomplish this, the motor speed is estimated based on the known fundamental supply frequency, and the slip calculated. The motor output torque is obtained for this slip as the algebraic sum of the torques calculated for each time harmonic circuit. The torque so calculated is compared to the torque specified and the motor speed notionally adjusted until the two agree.

An iterative technique was also employed in the calculation of the current dependent magnetising and rotor leakage inductances. Initial values for L_m and L_2' are estimated and used to calculate the magnetizing current, i_m , and the rotor bar current, I_{bar} . These currents may be used with their relevant characteristics to derive new values for L_m and L_2' , which are then used to recalculate i_m and I_{bar} . This process is repeated until suitable agreement is found between two successive iterations. This iterative procedure is carried out using the fundamental-frequency components of i_m and I_{bar} .

3.5 Experimental Verification of the Equivalent Circuit on a Sinusoidal Supply

The parameters derived for the 4 kW motor were verified experimentally for sinusoidal operation at 50 Hz using the layout shown in Fig. 3.13. Accurate readings for torque and speed were obtained using an in-line torque transducer of ± 0.2 Nm accuracy. The load torque was applied using a separately excited 5 Hp shunt connected dc motor.

So that the simulation method and the calculated parameters could be

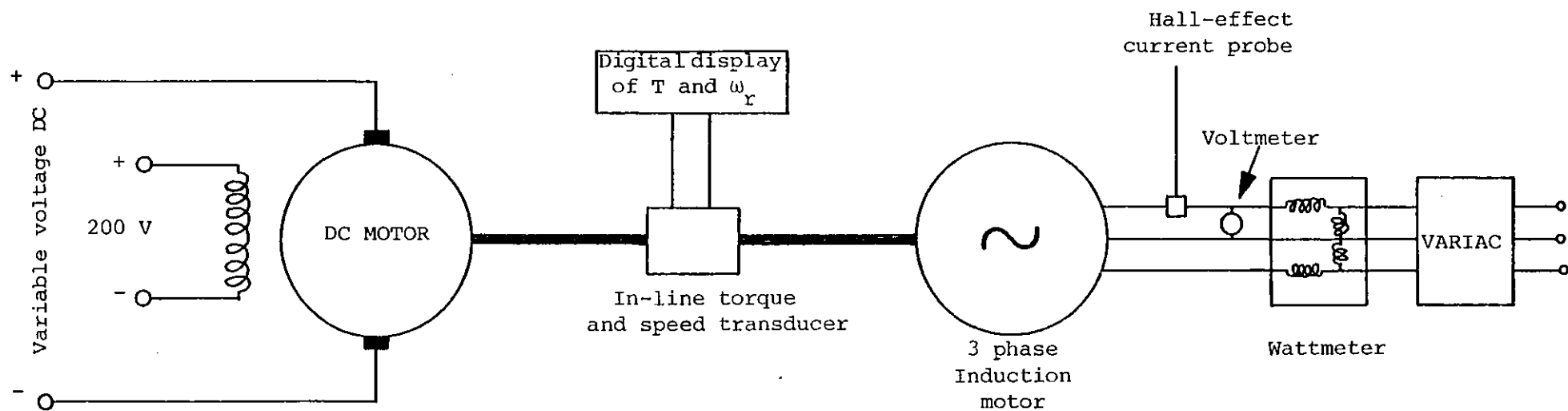


Fig. 3.13 Experimental set-up for verification of the test motor equivalent circuit parameters

fully verified, the motor had to be tested over its full speed range. This would require the motor to draw excessive currents at rated voltage; therefore the tests were initially carried out at a reduced line voltage of 200 V. Temperature effects caused by the still relatively high currents were noticeable at this voltage and so a further set of tests were done at 100 V.

Reasonable agreement was shown between the computed and experimental results, illustrated in Figs. 3.14 to 3.19.

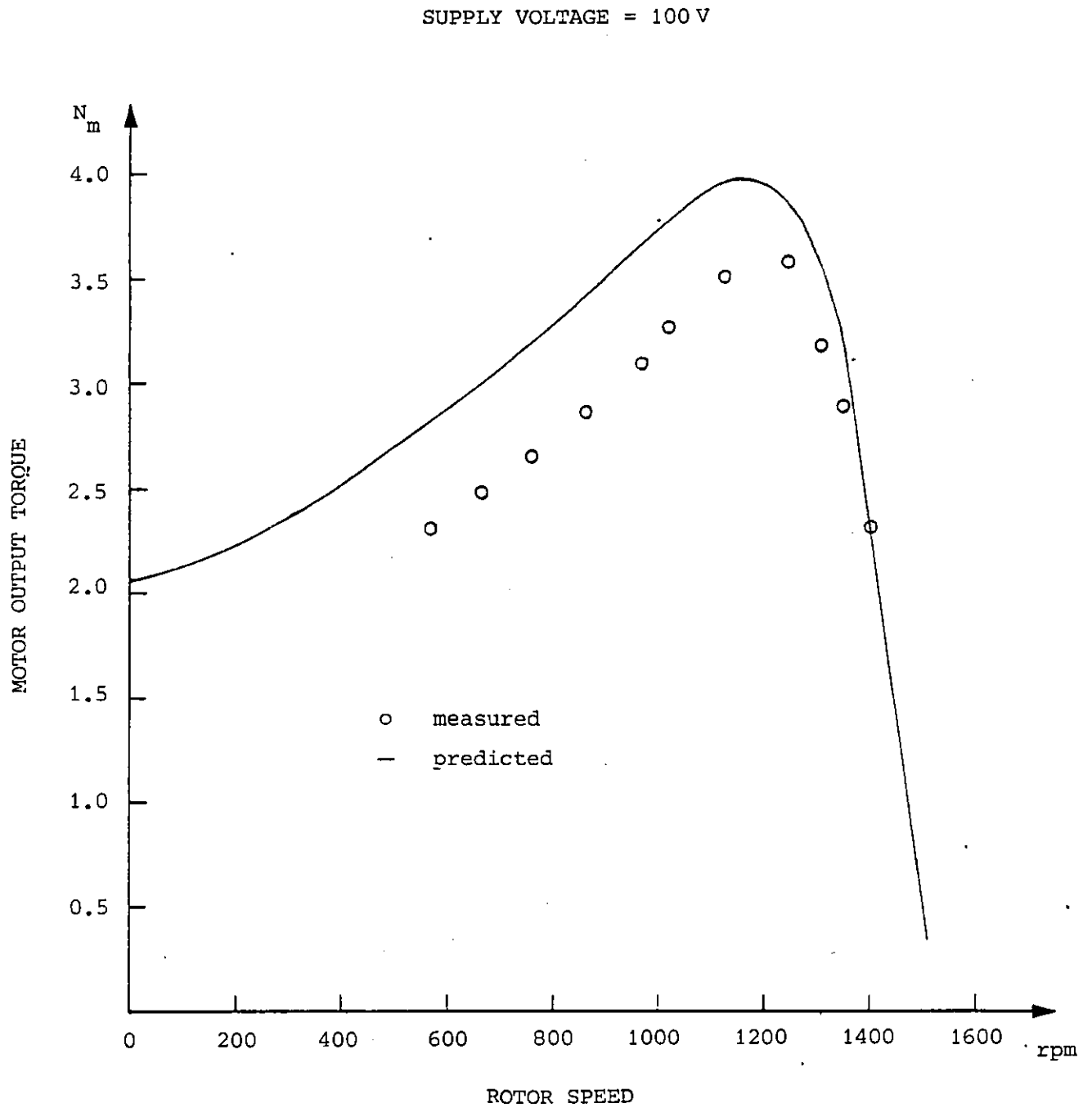


Fig. 3.14 Torque-speed curve for the test motor operating on a 100 V sinusoidal supply

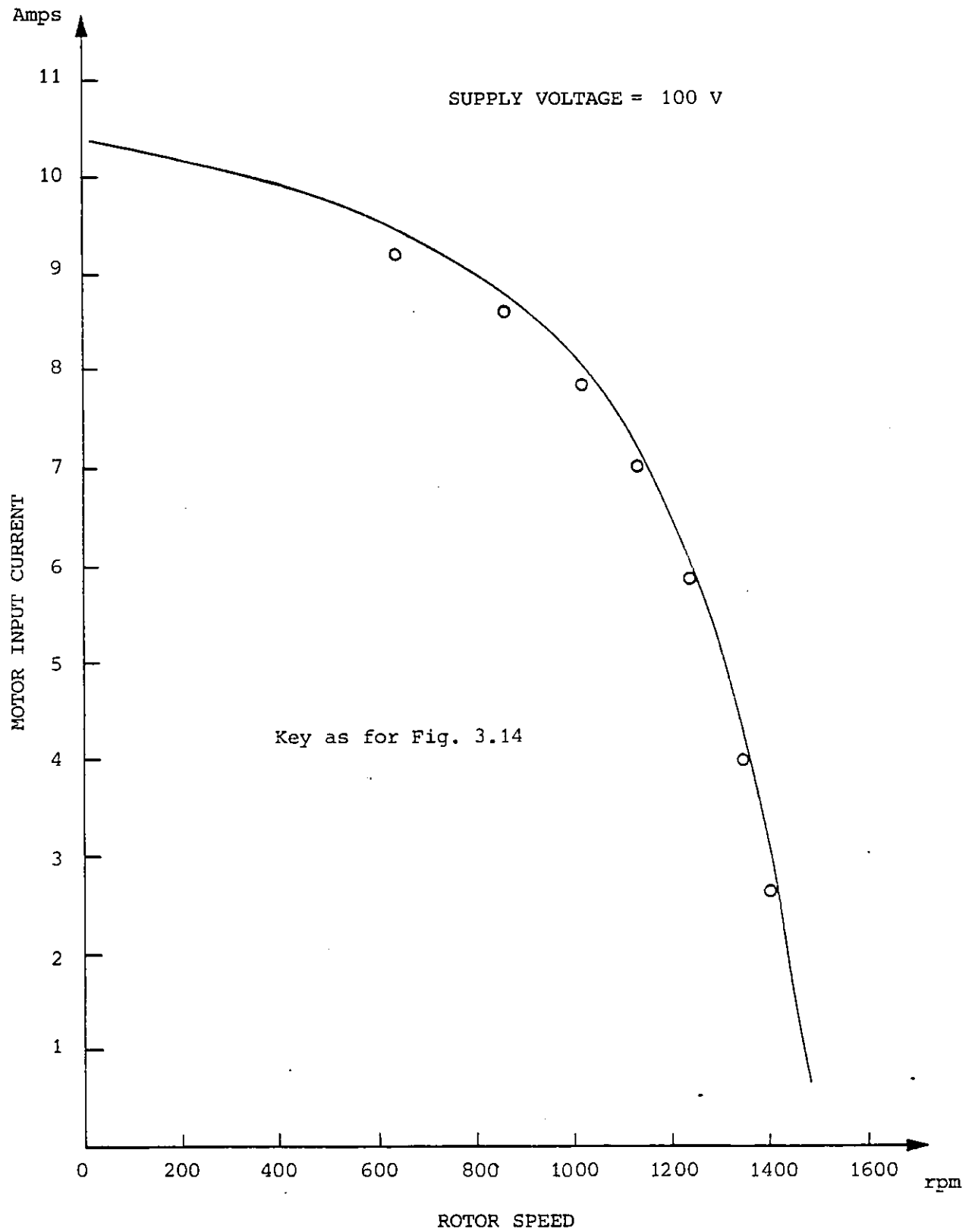


Fig. 3.15 Current-speed curve for the test motor operating on a 100 V sinusoidal supply

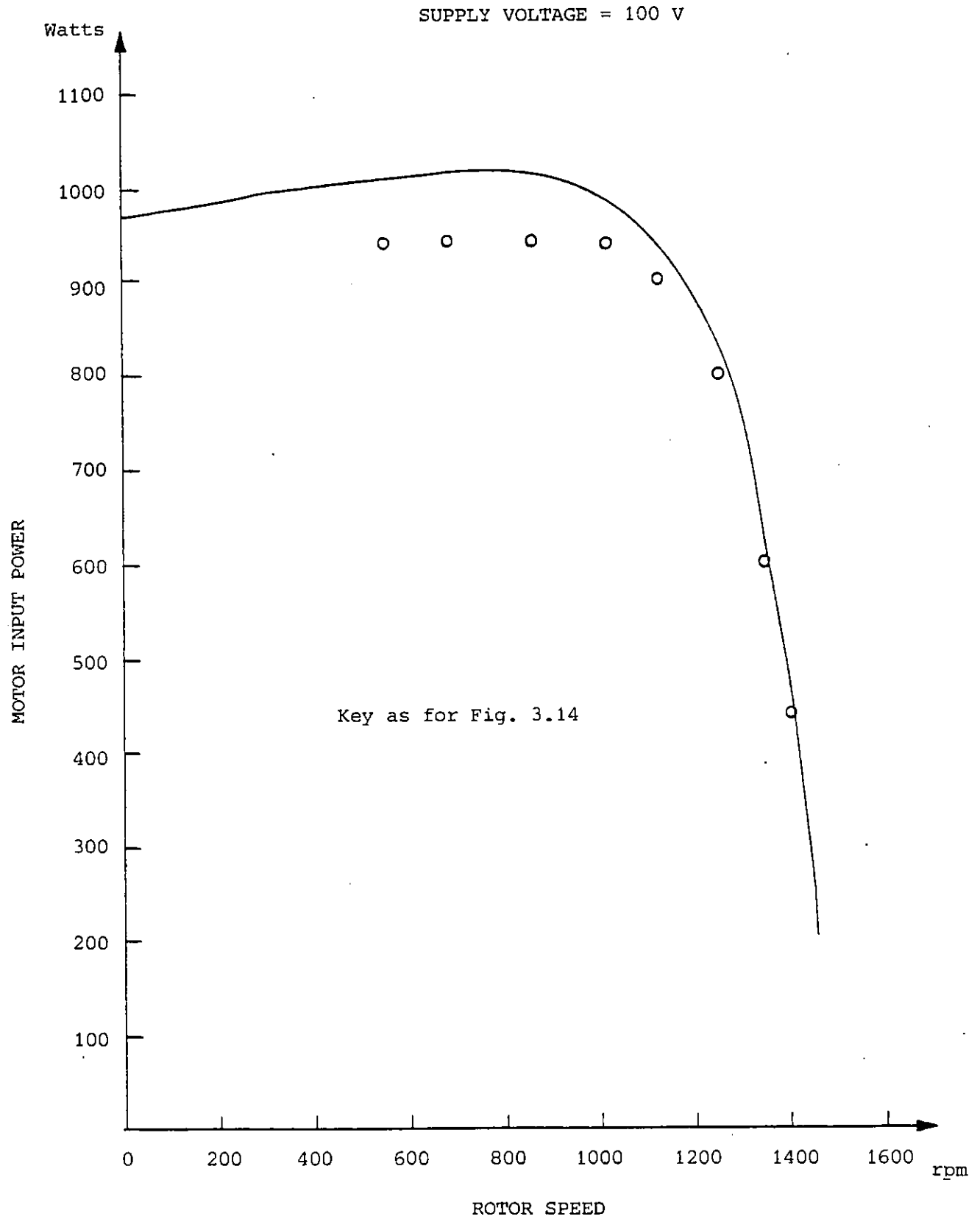


Fig. 3.16 Input Power-speed curve for the test motor operating on a 100V sinusoidal supply

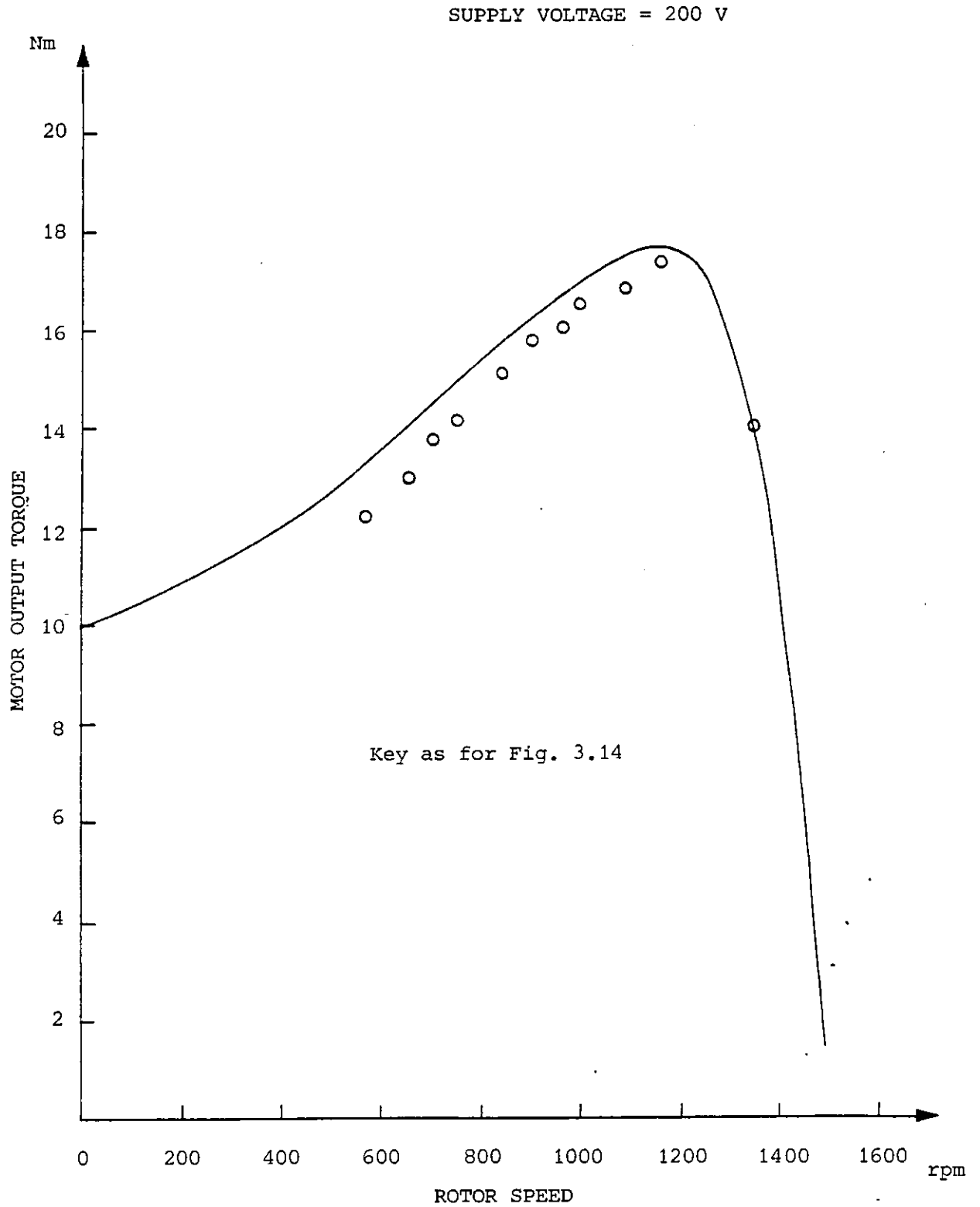


Fig. 3.17 Torque-speed curve for the test motor operating on a 200 V sinusoidal supply

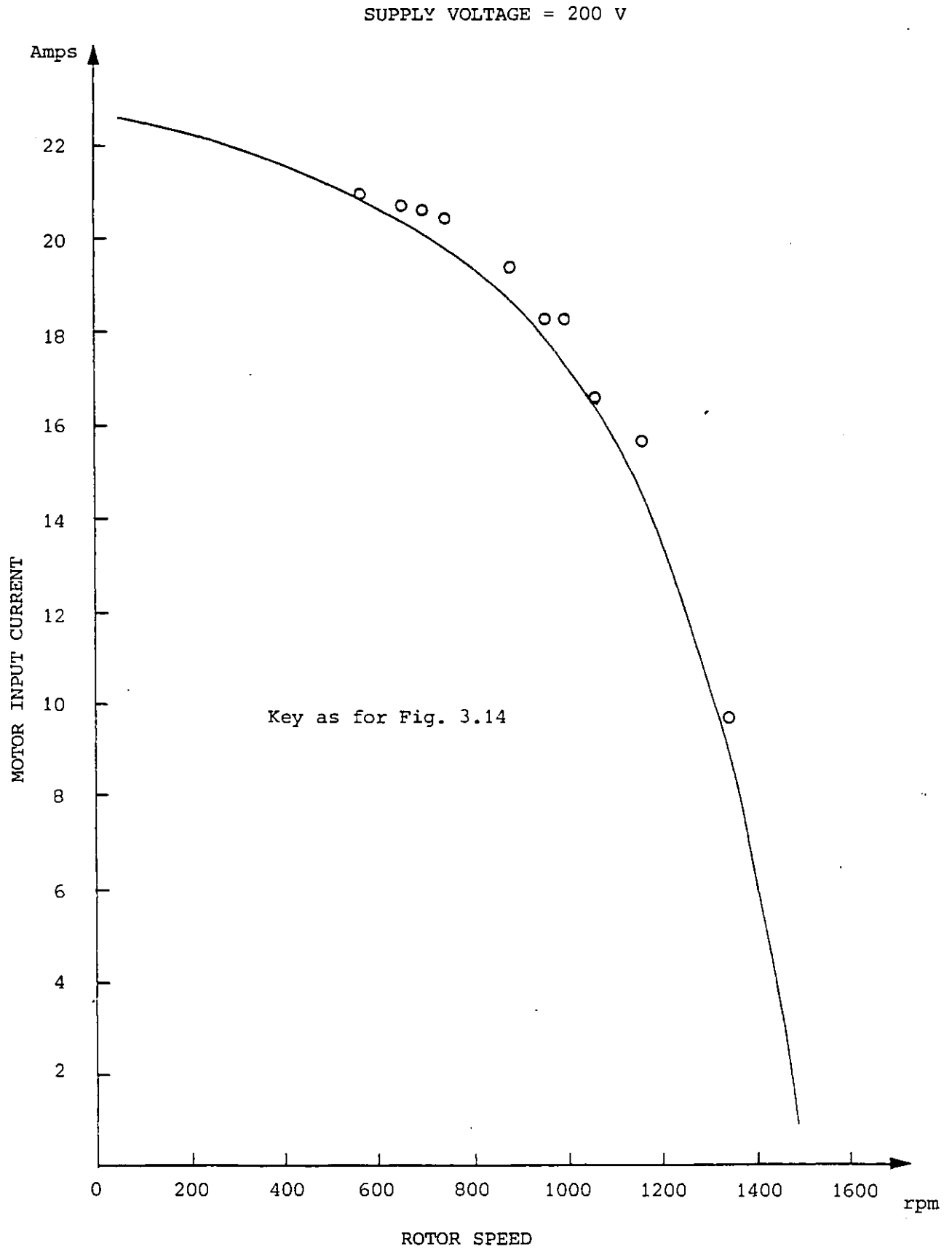


Fig. 3.18 Current-speed curve for the test motor operating on a 200 V sinusoidal supply

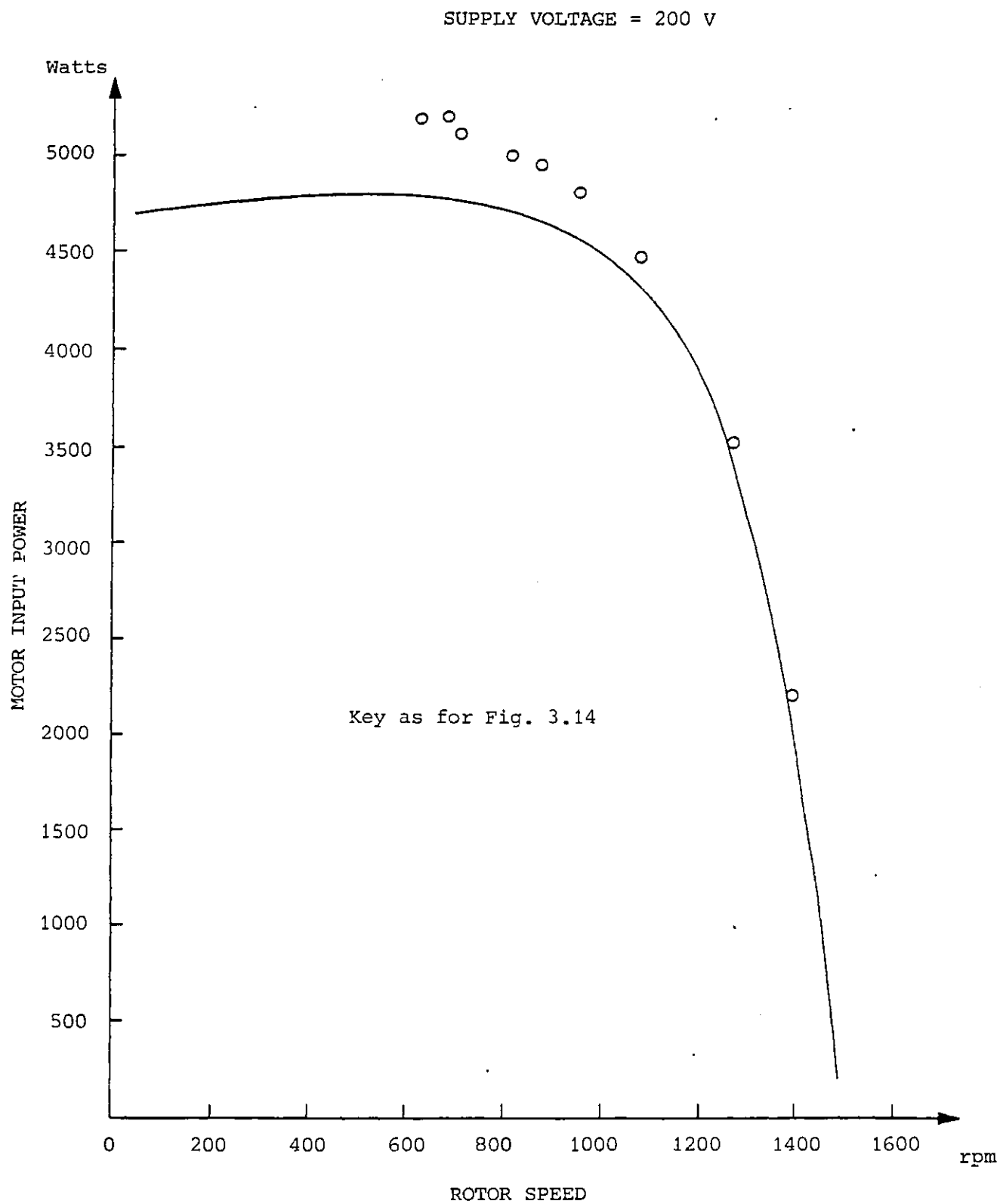


Fig. 3.19 Input power-speed curve for the test motor operating on a 200 V sinusoidal supply

CHAPTER FOUR

DEVELOPMENT OF THE SYSTEM MODEL

4.1 Introduction

In the previous chapter, the equivalent circuit and its parameters were verified for sinusoidal operation. This fundamental-frequency equivalent circuit forms the basis for the series of time harmonic equivalent circuits used in the simulation method described in section 3.2.2. In section 4.2 the simulation method is explained in detail with emphasis on the calculation of the motor line current and power losses. Simulation of the motor operating on a three phase inverter is verified experimentally by comparing measured and predicted line current waveforms in section 4.3.

With the development of the inverter and motor models, a system model simulating the inverter/motor drive is possible. The system model is described in section 4.4 and is verified experimentally in section 4.5.

4.2 Simulating the Induction Motor Operating from the Three Phase Inverter

4.2.1 Number of Harmonics Considered: The simulation technique adopted in this study represents the non-sinusoidal inverter output voltage as a series of sinusoids of different frequency. In the derivation of the Fourier Series (section 8.1), an infinite number of harmonics define the waveform. In practice, only a limited number of harmonics can be considered. It is therefore necessary to balance the accuracy of the representation with the computation times required to

achieve that accuracy. In general, a large number of harmonics have to be evaluated when simulating inverter output waveforms, so that step changes in voltage levels can be included.

Investigation of the simulation accuracy for different harmonic numbers revealed that increasing the number of harmonics beyond 200 resulted in negligible change in the computer predictions. All the remaining simulation work in this thesis is therefore carried out using 200 harmonics. Actual voltage waveforms and their reconstructions using 200 harmonics are compared in Figs. 4.1 to 4.4. An uncomparred reconstruction of the 25 Hz waveform is shown in Fig. 4.5.

4.2.2. Non-linear Effects: Although deep bar effect is assumed to be absent in this study (section 3.3.6), other non-linear effects due to saturation must be included. Such non-linearities are present in the magnetising and rotor leakage inductances.

The level of saturation in the motor is determined largely by the principle-frequency component of airgap flux, which is normally the dominant field component. The common path followed by all components of the magnetising flux lies partly in air and partly in iron. For standard industrial designs, the saturation of the iron parts of this path is not excessive and the airgap reluctance dominates the magnetising reactance. It is therefore a reasonable approximation to assume that the magnetising reactance for the time-harmonics may be obtained by simple frequency scaling from the magnetising reactance calculated from the fundamental frequency component of airgap flux. The calculation of the fundamental frequency magnetising reactance is described in section 3.2.2. For normal operating conditions, the harmonic slip s_k is approximately unity for all time-harmonics. This causes the rotor branch in the

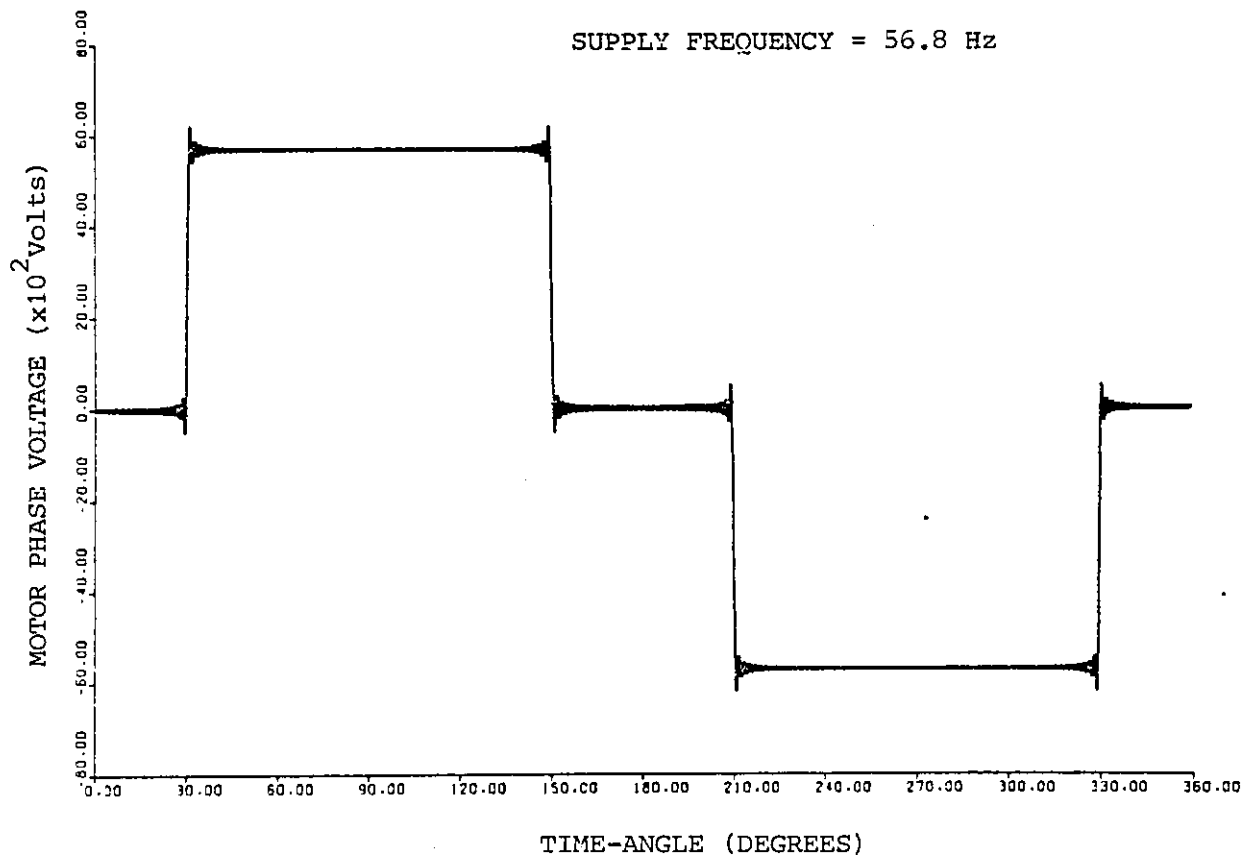


Fig. 4.1 Reconstruction of the motor phase voltage for 56.8 Hz using 200 harmonics

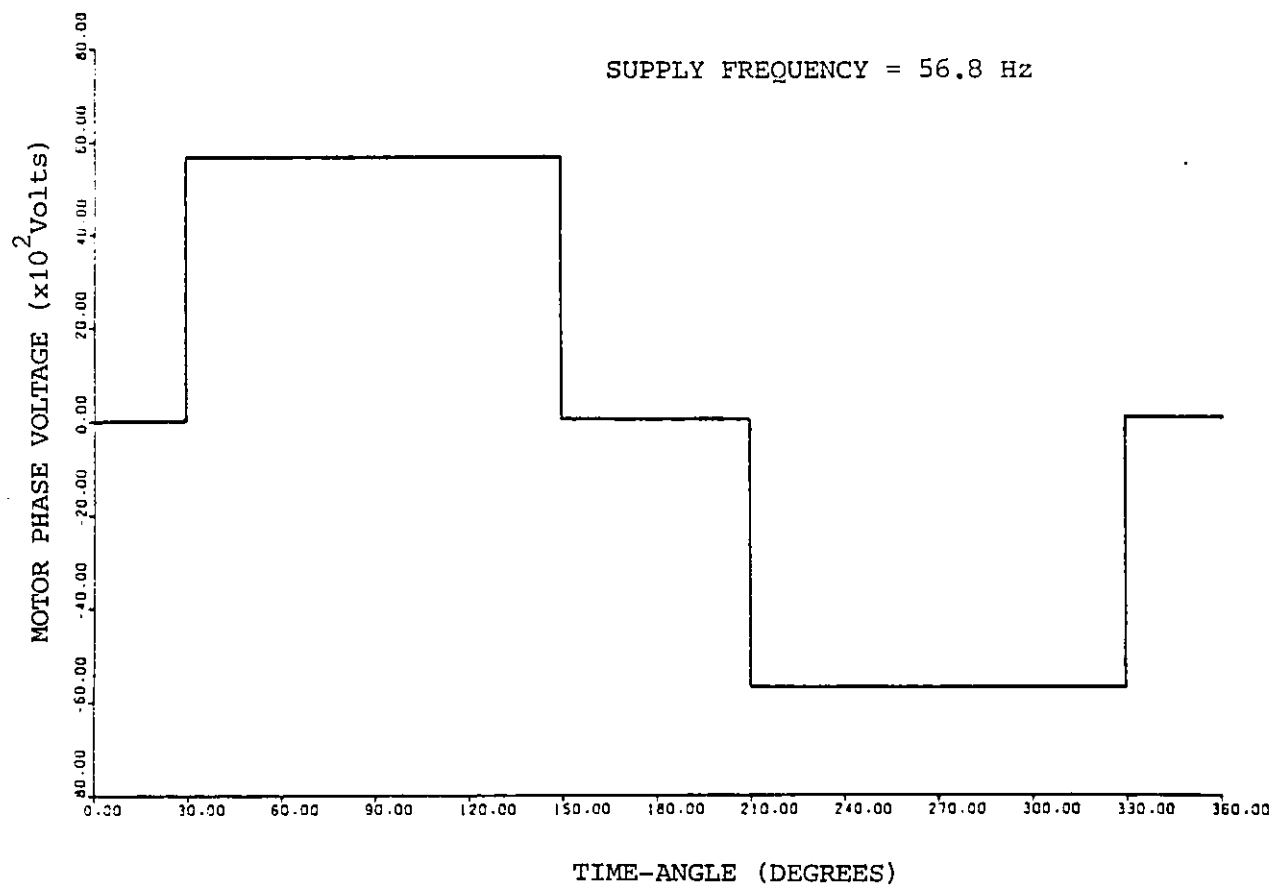


Fig. 4.2 Actual motor phase voltage for 56.8 Hz

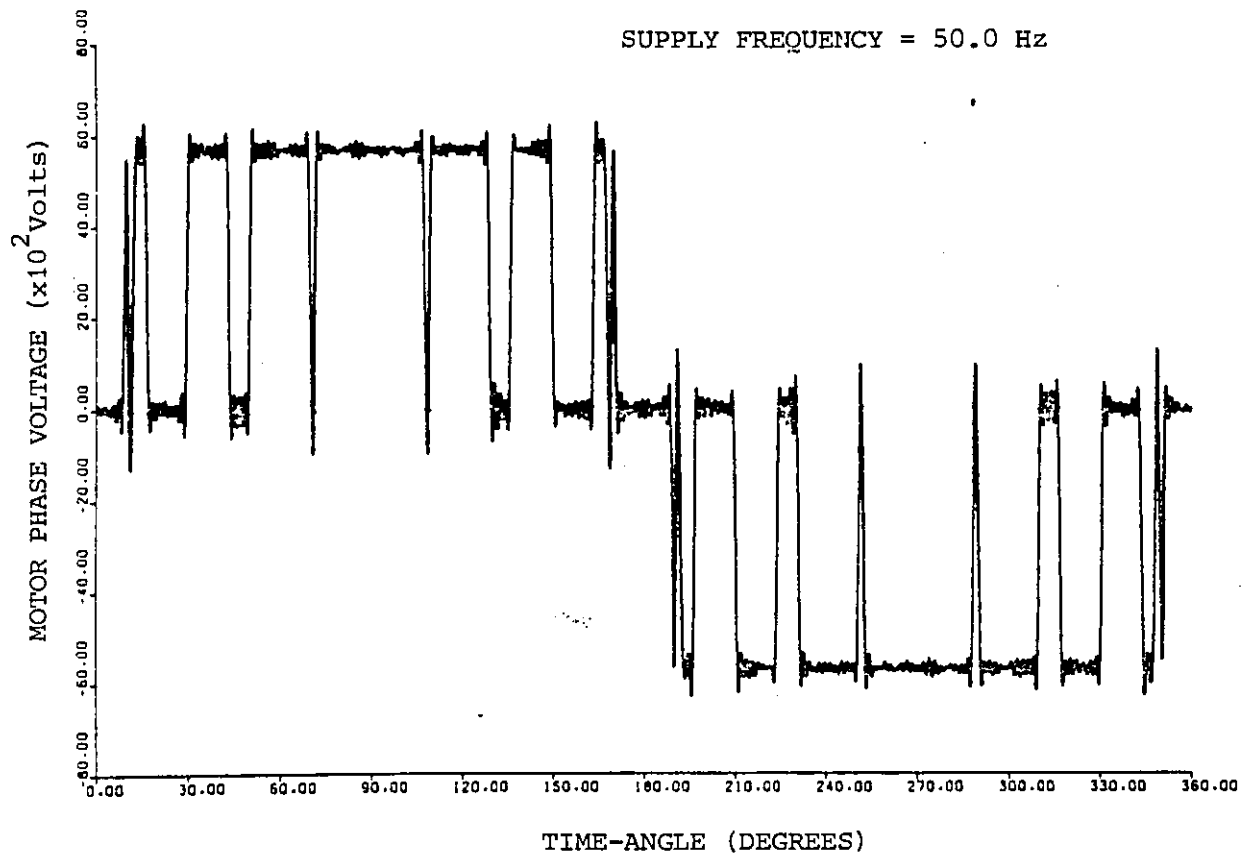


Fig. 4.3 Reconstruction of the motor phase voltage for 50.0 Hz using 200 harmonics

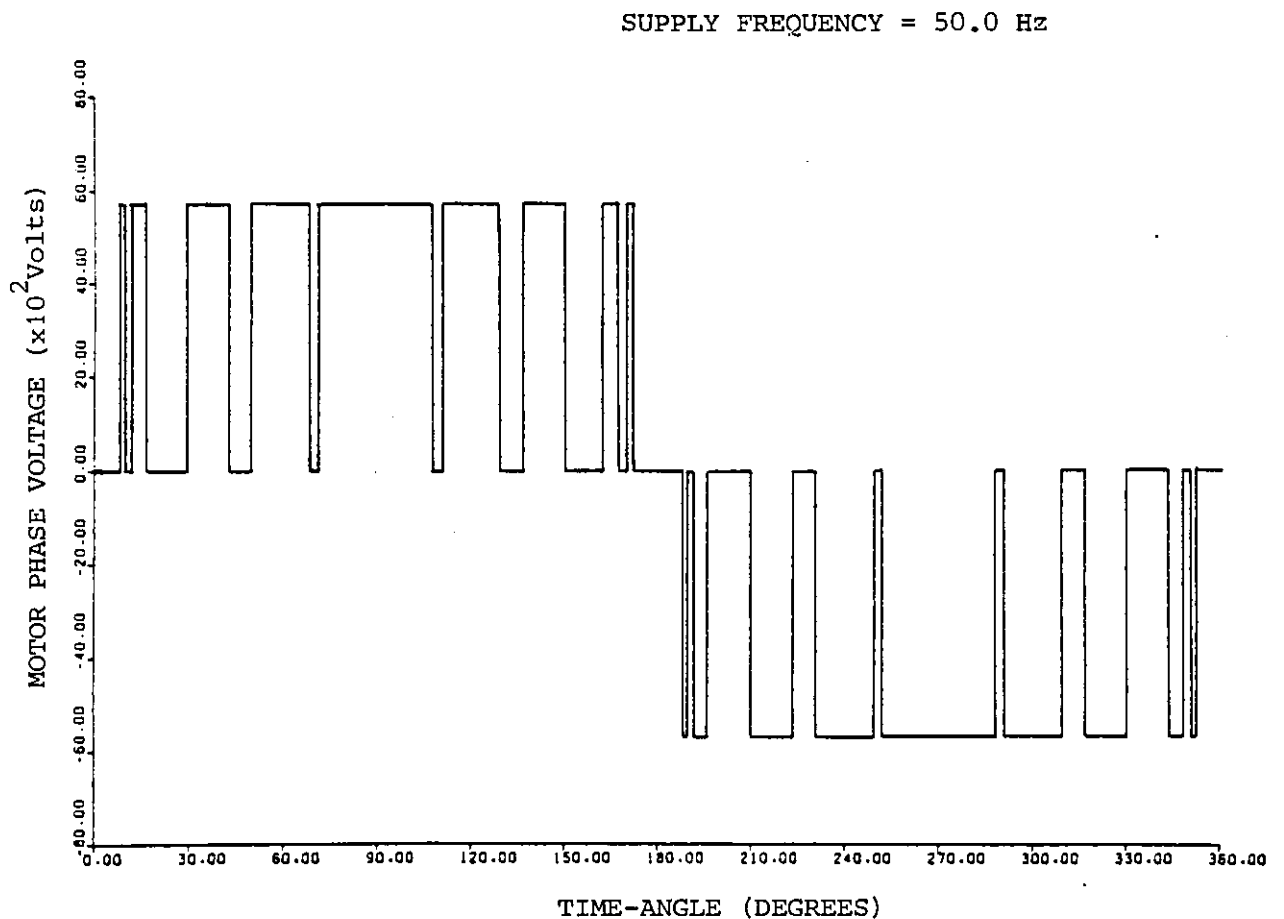


Fig. 4.4 Actual motor phase voltage for 50.0 Hz

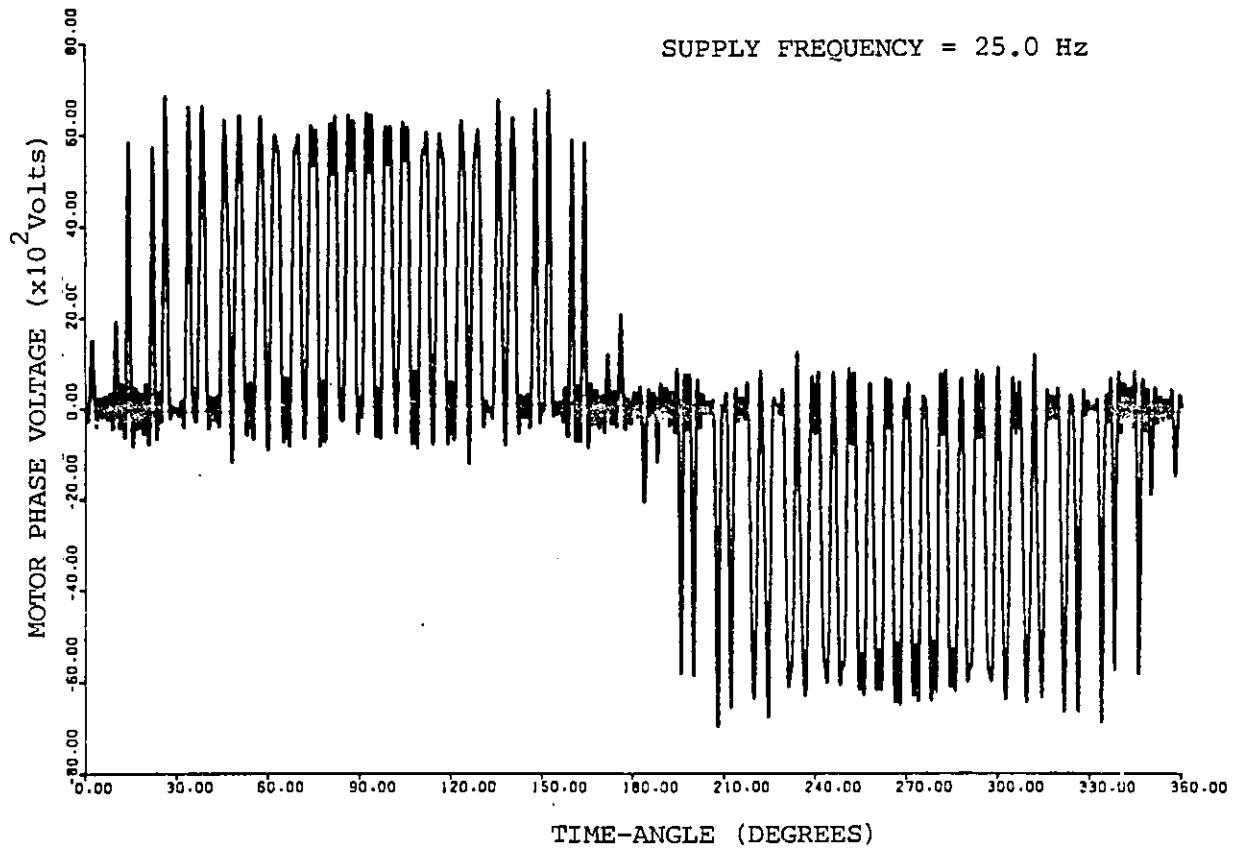


Fig. 4.5 Reconstruction of the motor phase voltage for 25.0 Hz using 200 harmonics

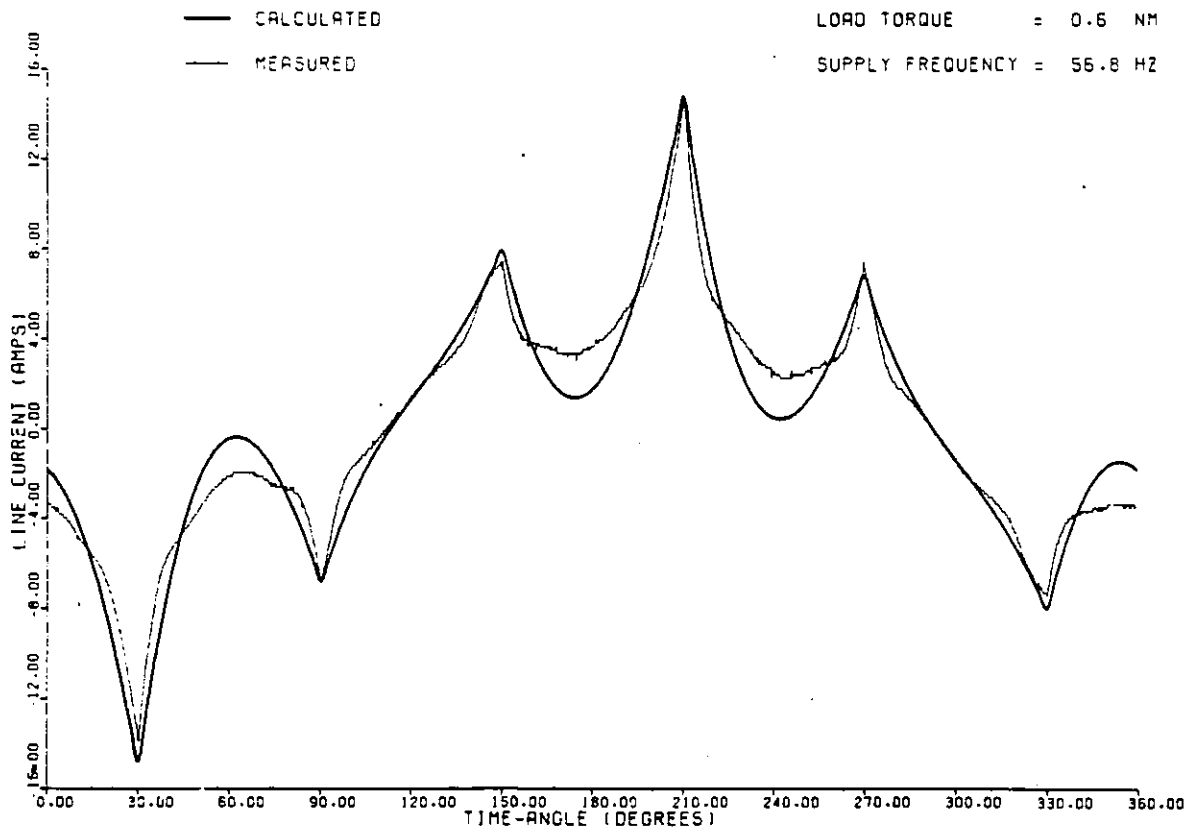


Fig. 4.6 Comparison of motor line current waveforms

harmonic-equivalent circuits to have a low resistance thereby reducing the effect of the magnetising branch. The above assumption therefore causes little inaccuracy. Indeed, several authors have suggested that the magnetising branch may be removed from the harmonic circuits, to improve computation times with little loss in accuracy (15, 2).

A similar approach applied to the rotor slot bridge leakage inductance, however, would lead to serious inaccuracies. The rotor slot bridge flux follows paths which are entirely in iron, therefore, the saturated bridge leakage inductance will not scale linearly with frequency. The operating point on the B-H curve for the rotor slot bridge is again assumed to be set by the principle-frequency component of rotor bar current. The time-harmonic rotor bar currents may now be viewed as producing a magnetisation/demagnetisation effect similar to that of a minor in the fundamental B-H curve. The slope of this minor would be significantly less than that for the fundamental curve at the calculated operating point. This argument suggests that the rotor leakage inductance seen by the time-harmonic currents is much smaller than that calculated using the fundamental current. To this end, a saturated value of rotor slot bridge leakage inductance was assumed for the time-harmonic equivalent circuits.

4.2.3 Calculation of the Motor Line Current: The Fourier Series describing the voltage across a motor phase, expressed previously as

$$v(t) = \sum_{n=1}^{200} \hat{V}_n \cos(n\omega t + \theta_n) \quad (4.1)$$

is not in a convenient form for use with the harmonic equivalent circuits.

The input impedance of the equivalent circuit is expressed in a complex form and so a complex representation of the voltage is more suitable.

Equation 4.1 may be written as

$$v(t) = \sum_{n=1}^{200} \text{Re} [\sqrt{2} \bar{V}_n e^{jn\omega t}] \quad (4.2)$$

where

$$\bar{V}_n = \frac{\hat{V}_n}{\sqrt{2}} e^{j\theta_n} \quad (4.3)$$

Each time-harmonic voltage \bar{V}_n may now be applied to its approximate equivalent circuit, and the n^{th} harmonic input current \bar{I}_n calculated in the usual manner as

$$\bar{I}_n = \frac{\hat{I}_n}{\sqrt{2}} e^{j\phi_n} \quad (4.4)$$

\hat{I}_n and ϕ_n are derived from the computed current according to

$$\hat{I}_n = \sqrt{2} |\bar{I}_n| \quad (4.5)$$

$$\phi_n = \tan^{-1} \left\{ \frac{\text{Imag}(\bar{I}_n)}{\text{Real}(\bar{I}_n)} \right\} \quad (4.6)$$

The real time-dependent n^{th} harmonic current is recovered as

$$i_n(t) = \hat{I}_n \cos(n\omega t + \phi_n) \quad (4.7)$$

The total input current is obtained by superposition

$$i(t) = \sum_{n=1}^{200} i_n(t) = \sum_{n=1}^{200} \hat{I}_n \cos(n\omega t + \phi_n) \quad (4.8)$$

Using this technique, the phase relationship between the harmonics is retained throughout the calculation process.

The motor line current is derived from the phase current as

$$i_{\text{line}}(t) = \sum_{n=1}^{200} \hat{I}_n \cos(n\omega t + \phi_n) - \sum_{n=1}^{200} \hat{I}_n \cos(n(\omega t + \frac{2\pi}{3}) + \phi_n) \quad (4.9)$$

which may be simplified to

$$i_{\text{line}}(t) = 2 \sum_{n=1}^{200} \hat{I}_n \sin(\frac{n\pi}{3}) \sin(n\omega t + \phi_n + \frac{n\pi}{3}) \quad (4.10)$$

4.2.4 Calculation of the Motor Power Losses: Power loss in the motor is assumed to be due to core losses, stator and rotor copper losses. All other loss mechanisms are assumed to be negligible. As the motor input and output powers had to be calculated for use in the system model (section 4.4), the motor losses were calculated indirectly as

$$P_{\text{LOSS}} = P_{\text{IN}} - P_{\text{OUT}} \quad (4.11)$$

The output power is calculated by summing the harmonic torque components and multiplying by the rotor speed.

$$P_{\text{OUT}} = \omega_r \sum_{n=1}^{200} T_n \quad (4.12)$$

T_n is the torque produced by the n^{th} harmonic field, calculated from the equivalent circuit as

$$T_n = \frac{3I_2'^2 R_2'}{s_n \omega_{sn}} \quad (4.13)$$

The input power may be expressed, in terms of complex quantities, as

$$P_{IN} = 3 \sum_{n=1}^{200} R_e(\bar{v}_n \bar{i}_n^*) \quad (4.14)$$

where * denotes complex conjugate.

4.3 Experimental Verification of the Motor Simulation for Operation from the Three Phase Inverter

The simulation method presented in the previous section should ideally be verified using measured values for the motor input and output powers. However, although the output power is easily measured, the high voltage and current levels present in the motor supply, combined with their high harmonic content, makes accurate measurement of the input power extremely difficult. As a consequence, the motor simulation was verified by the comparison of measured and predicted line current waveforms. This verification method is appropriate to this situation as an accurate predication of the motor line current waveform is required when the motor and inverter models are combined to form the system model in section 4.4.

In previous investigations of this type the computed current waveforms, usually produced by computer graphics, are compared with the measured current waveforms displayed separately as oscilloscope traces (43,47). This method of verification has inherent problems because the two waveforms are presented separately and on different scales. It is therefore very difficult to directly compare the two waveforms and so judge the accuracy of the simulation. To overcome this problem, a method of displaying the measured and predicted waveforms on the same graph was

developed.

A similar experimental procedure to that described in section 2.3 was used. The motor phase voltage and line current were digitally recorded using the DL912 transient recorder. The voltage was measured using 50:1 compensated probes via an isolating differential amplifier and a 50 MHz bandwidth Hall effect current probe was used to measure the line current. A spectrum analyser was used to accurately determine the fundamental frequency of the inverter output.

The two stored waveforms were transferred to an LSI-11 mini-computer where they were processed to isolate a single inverter output cycle. The switching angles describing the motor phase voltage waveform were calculated and the digitised description of one cycle of the motor line current was extracted. These two sets of data were downloaded to the campus computer for further processing, as this computer was far faster than the LSI-11 and had superior graphics facilities.

The switching angles describing the motor phase voltage were used in the motor simulation program to calculate the line current waveform. The computed and measured waveforms were drawn on the same axes using computer graphics. These two waveforms can now be compared directly as they were both derived for identical motor phase voltages.

Graphical outputs comparing measured and predicted line current waveforms are presented in Figs. 4.6 to 4.14 for several load torques and fundamental drive frequencies. The agreement between computed and measured results will be seen to be very close. The major discrepancies between the measured and predicted waveforms are thought to be due to the presence of slot ripple in the measured waveforms. An example of the effect of slot ripple is shown in Fig. 4.15 (for quasi-square wave operation at rated torque) in which slot ripple is seen propagating

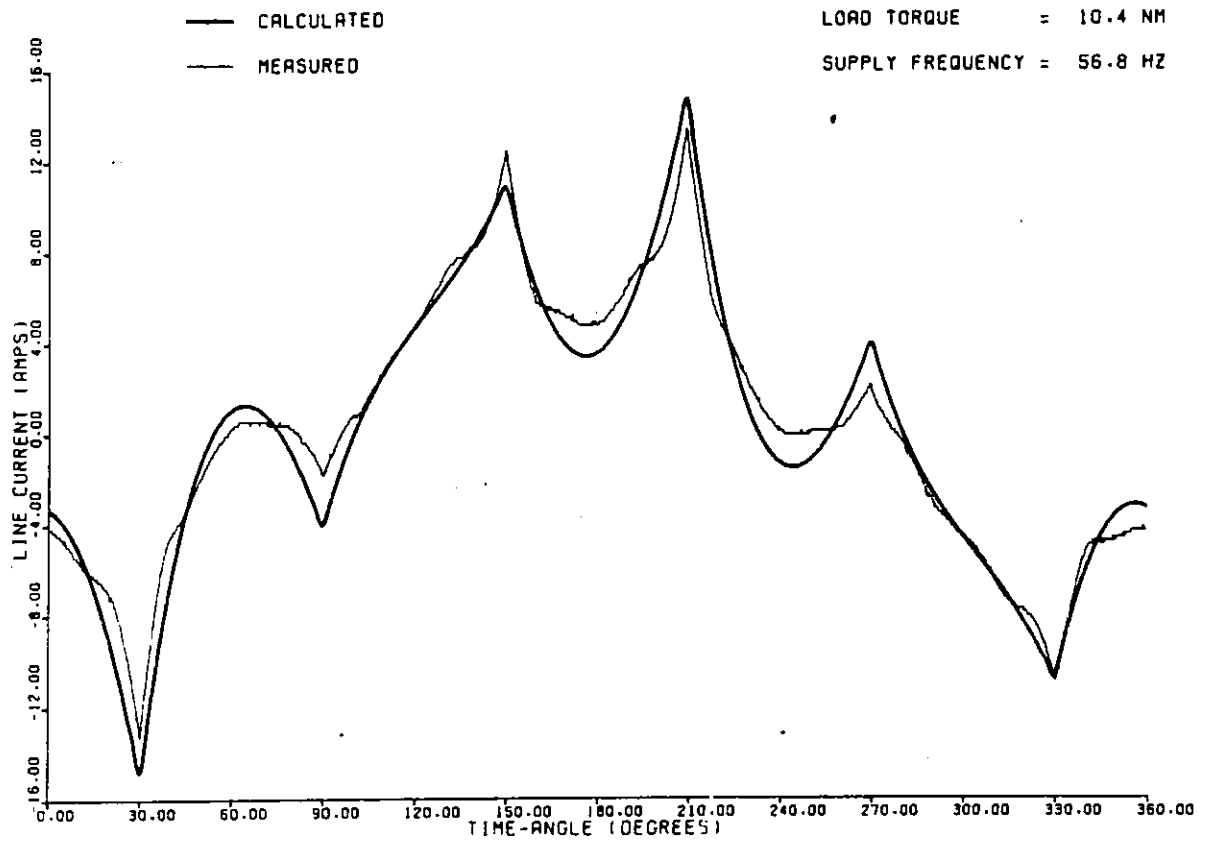


Fig. 4.7 Comparison of motor line current waveforms

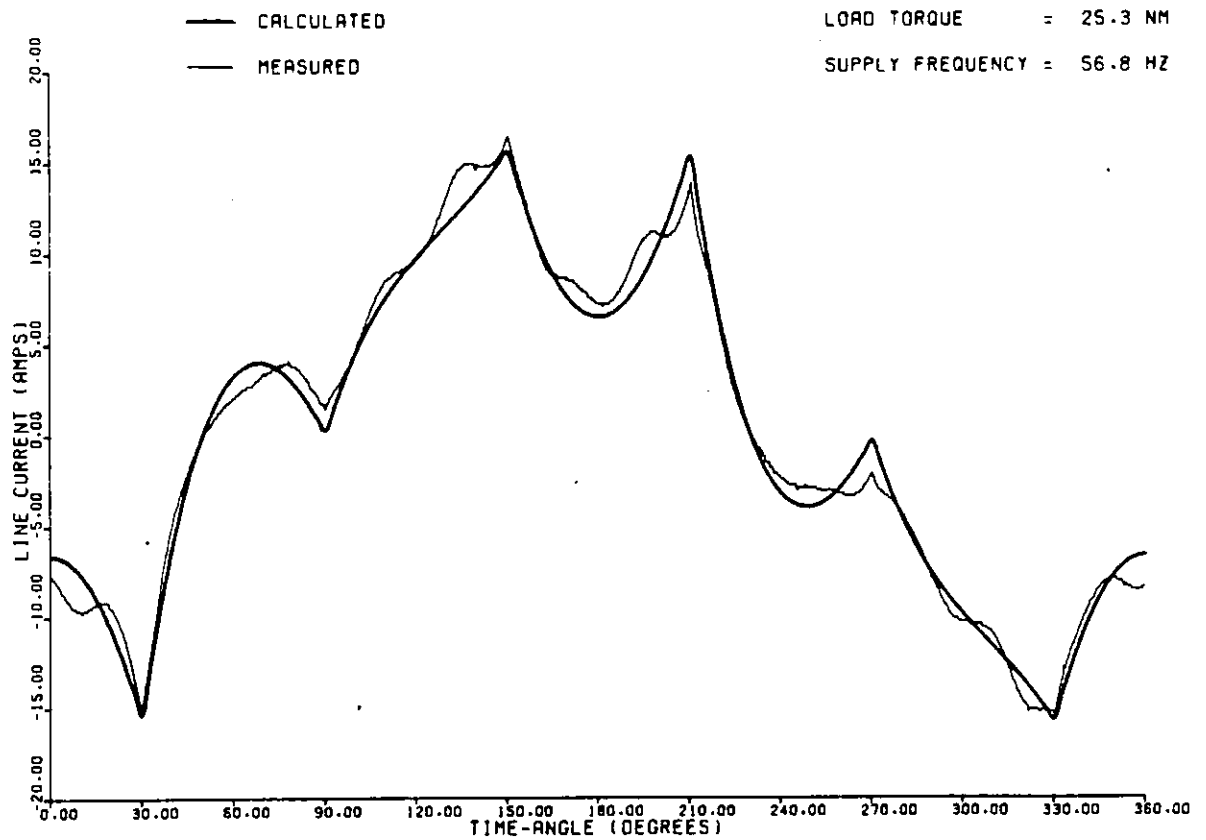


Fig. 4.8 Comparison of motor line current waveforms

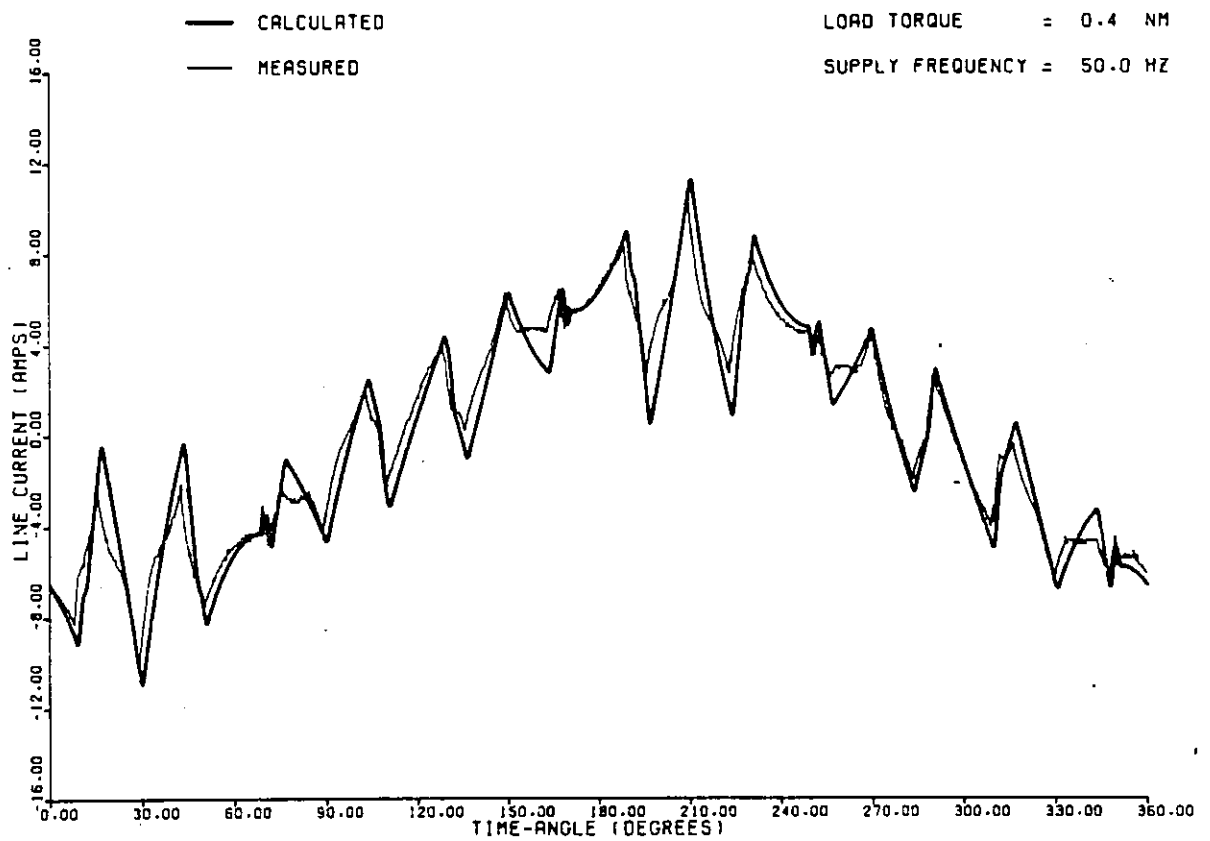


Fig. 4.9 Comparison of motor line current waveforms

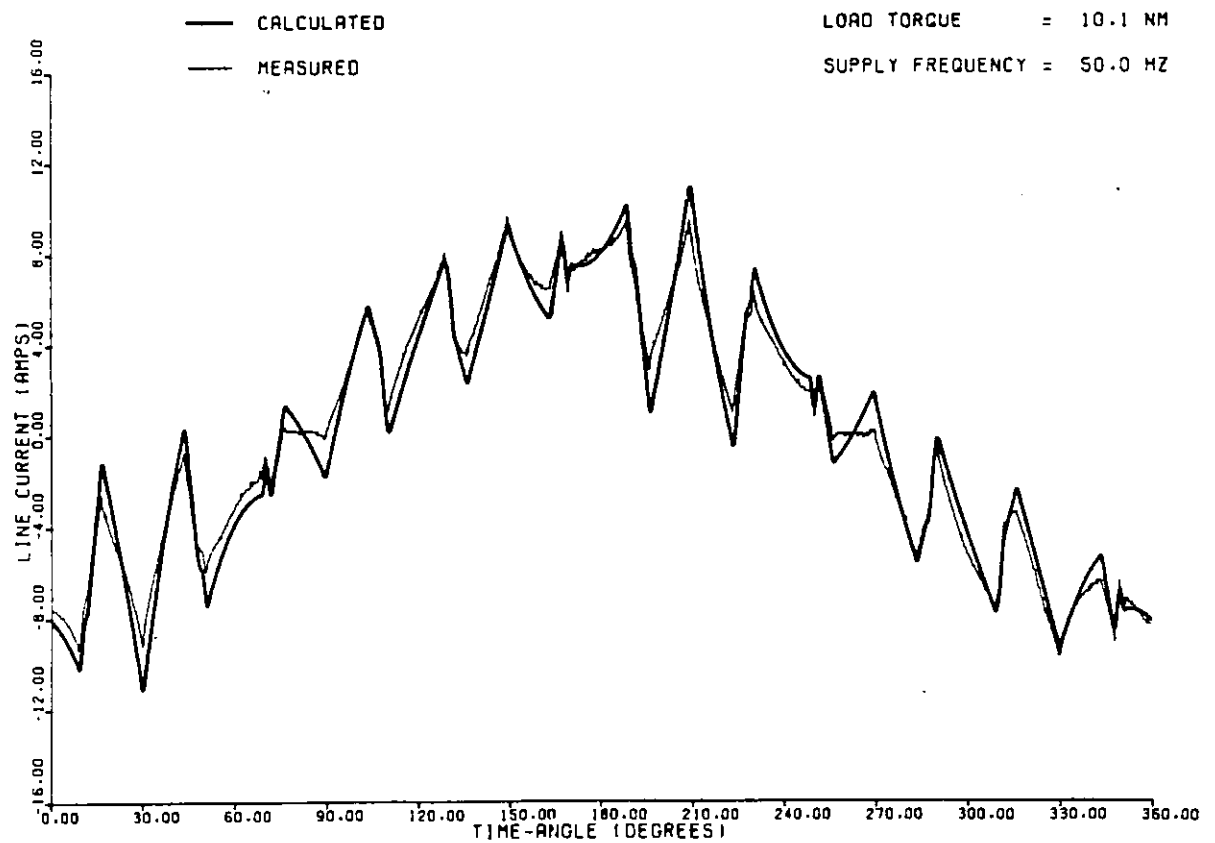


Fig. 4.10 Comparison of motor line current waveforms

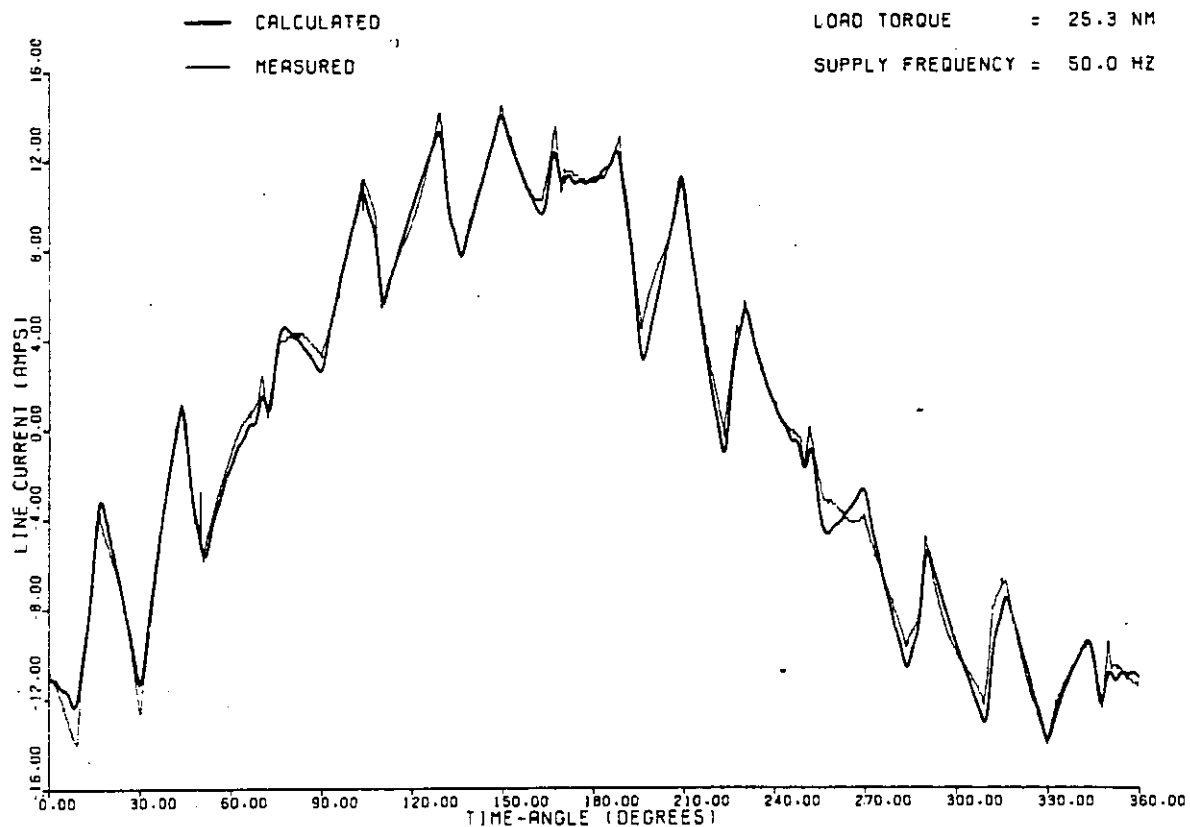


Fig. 4.11 Comparison of motor line current waveforms

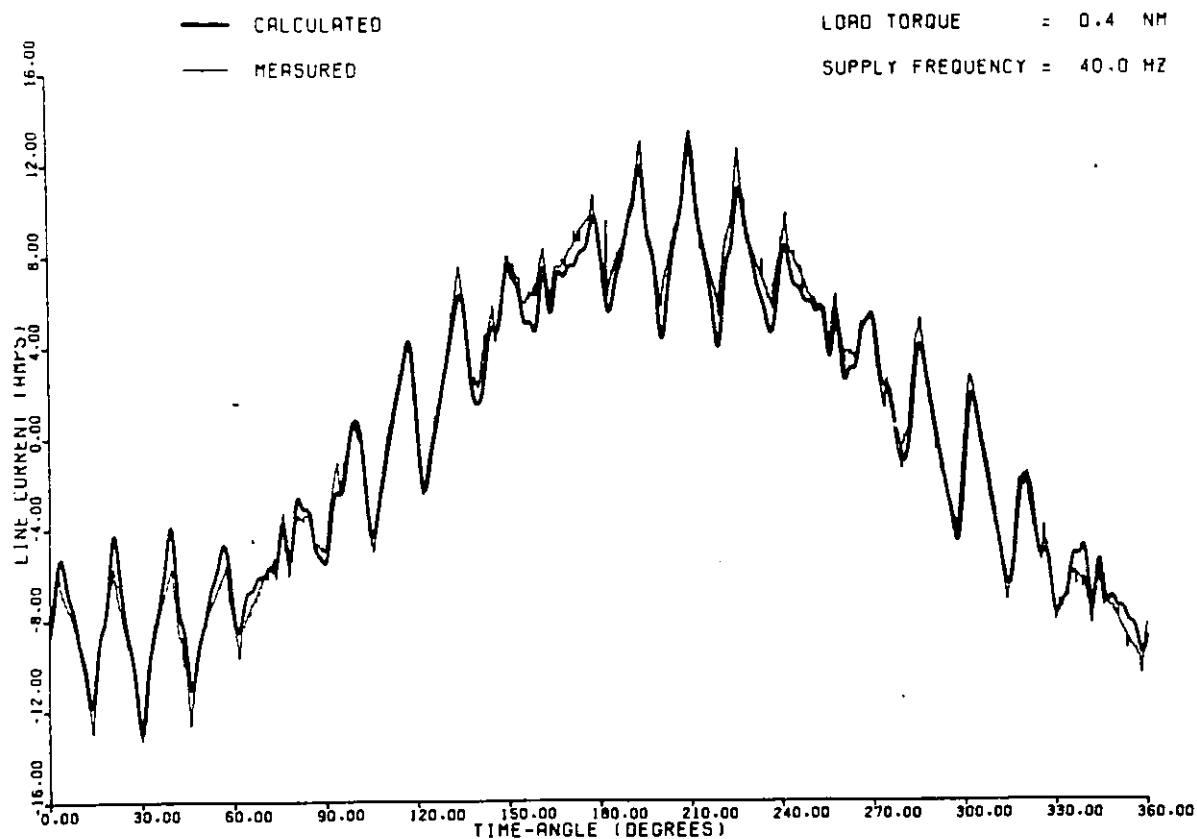
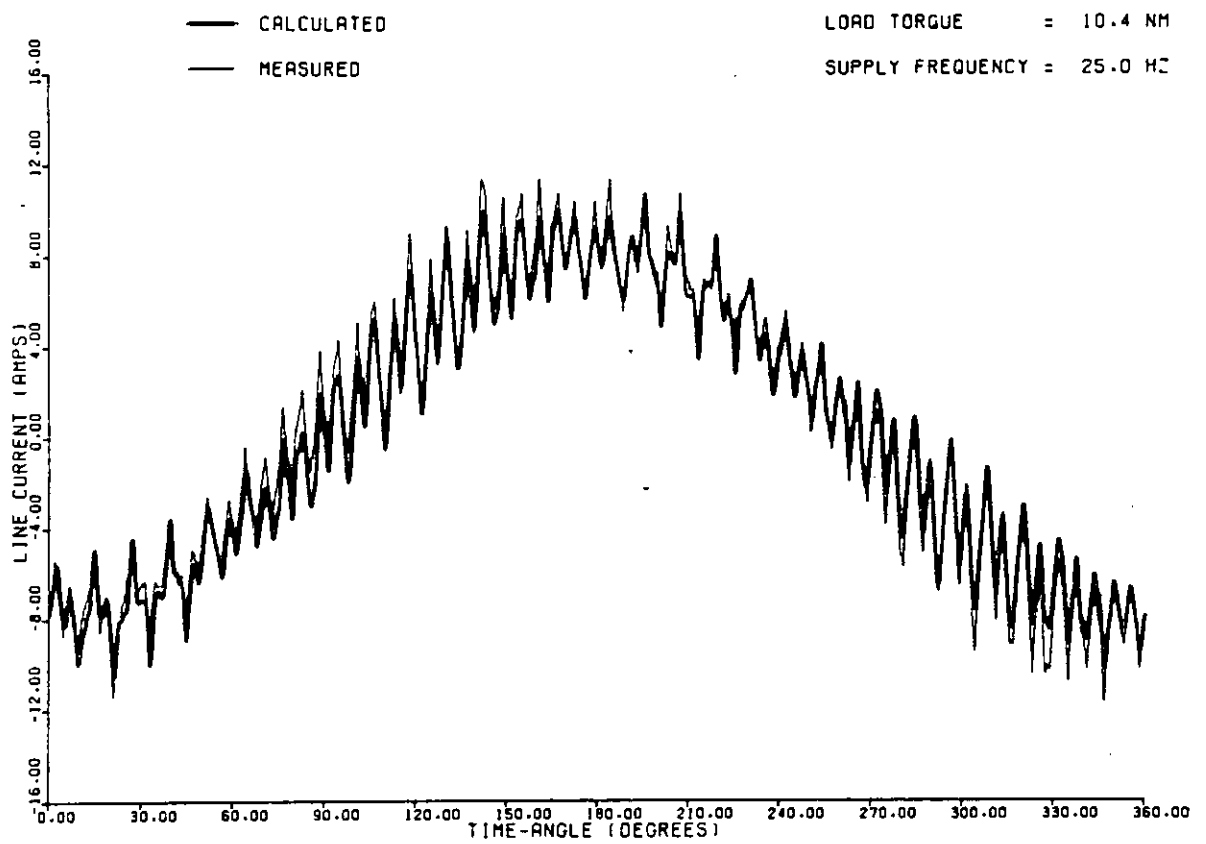


Fig. 4.12 Comparison of motor line current waveforms



4.13 Comparison of motor line current waveforms

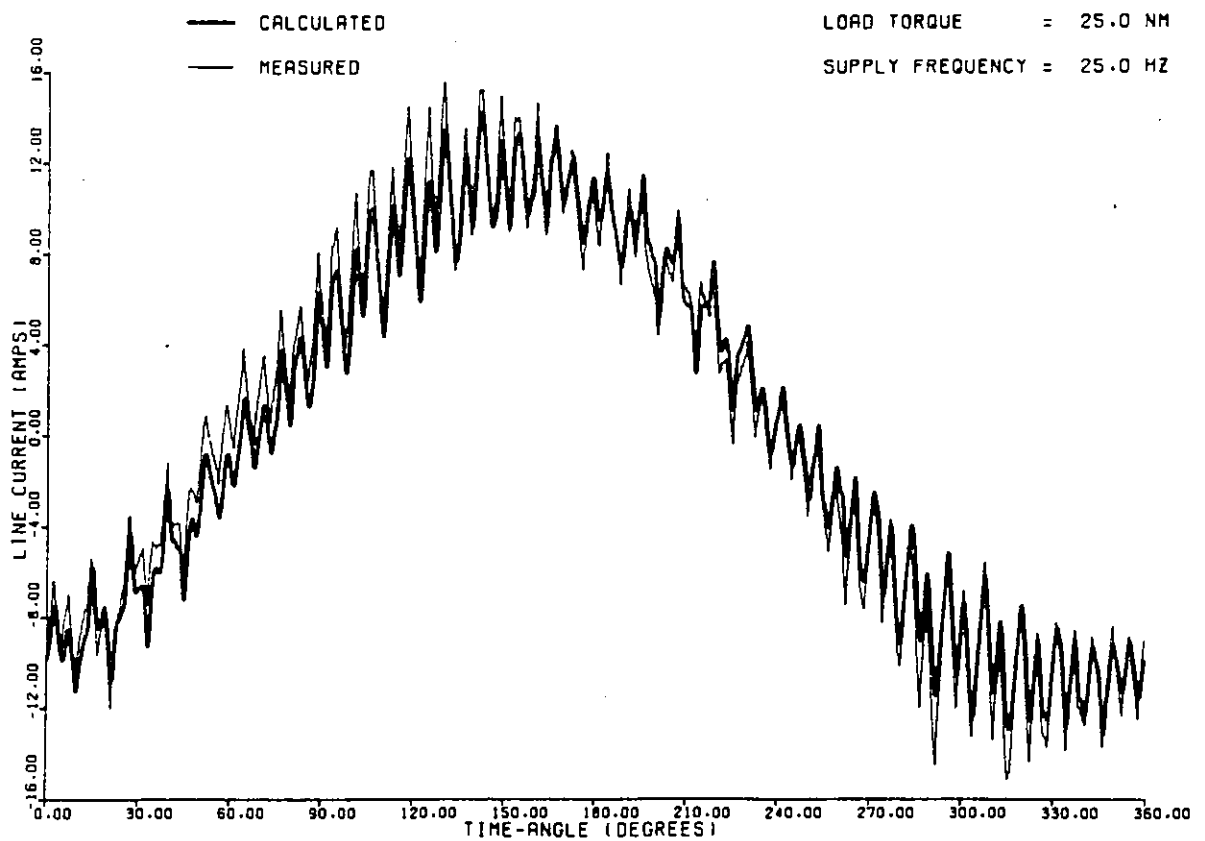


Fig. 4.14 Comparison of motor line current waveforms

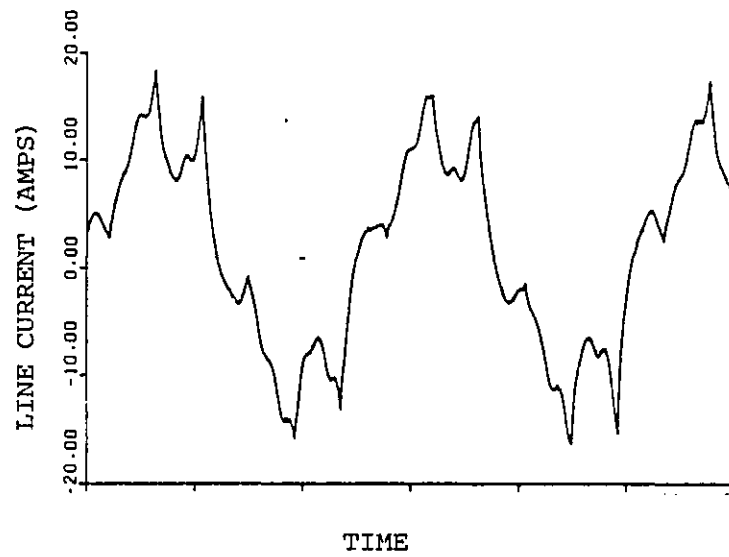


Fig. 4.15 Effect of slot ripple on the motor line current waveform

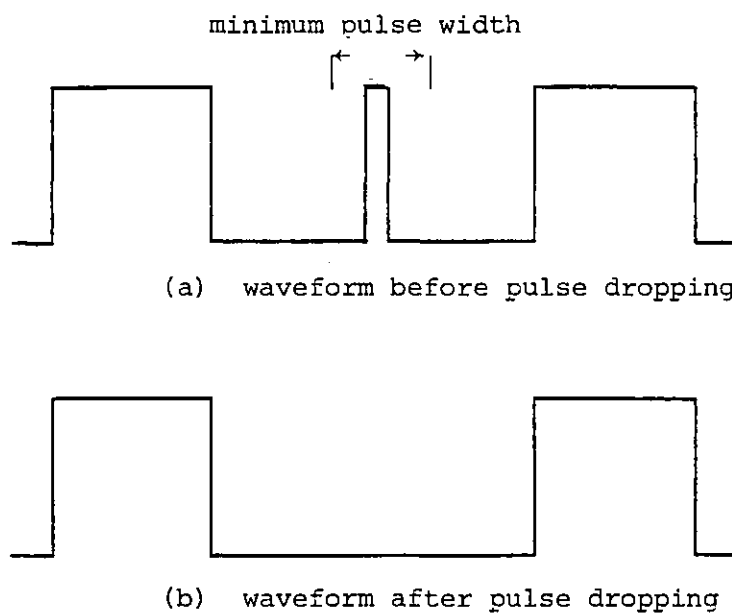


Fig. 4.16 Principle of pulse dropping

through several cycles of the motor line current.

4.4 Development of the System Model

A method of simulating the inverter/motor drive system may be developed using the three phase inverter and induction motor models. The combination of these two models is most easily described by following the logic of the system simulation program. Initially an ideal inverter producing ideal voltage waveforms is assumed, the inverter output voltage being described using the gating information for one phase in the form of the 2-level waveform switching angles.

At this point the concept of minimum pulse width is introduced. A limitation imposed by thyristor inverters is that a minimum time interval has to elapse after the initiation of commutation of a thyristor before its complementary thyristor is gated. This is necessary because of the finite time needed to commutate a thyristor. The minimum time interval (or minimum pulse width) is usually assumed to be marginally greater than the period of the commutation current waveform (Fig. 2.5). The inclusion of the minimum pulse width criterion was deemed necessary because the system model is used in the next chapter to compare PWM switching strategies which may demand unrealistically small pulses. Any pulse in the 2-level waveform which has a duration less than the specified minimum is therefore removed. An example of pulse-dropping is shown in Fig. 4.16.

The 2 level waveform resulting after pulse dropping is used to derive the motor phase voltage (the 3-level waveform). The motor phase voltage is calculated by subtracting two inverter line voltage waveforms, these being the 2-level waveform and the 2-level waveform phase shifted by 120 degrees. From the motor phase voltage, the motor efficiency and

line current may be calculated as described in section 4.2.

The line current, together with the inverter gating information, is used to calculate the inverter power loss, the components of which are the forward conduction, commutation and switching losses. The procedures for calculating these losses are described in sections 2.4.1, 2.4.2 and 2.6.

The system power loss is given by the sum of the motor and inverter power losses.

4.5 Experimental Verification of the System Model

Measurement of the drive (system) input and output powers together with the measured system efficiency derived from these two values were used to verify experimentally the system model. The drive input power was measured in a similar way to section 2.5 where the input power was calculated as the product of the DC source voltage and the DC input current. The voltage was measured using a digital dc voltmeter and the current was measured using a Hall-effect current probe in conjunction with a spectrum analyser. The drive output power was obtained as the product of motor output torque and motor speed measured using an in-line torque transducer.

The experimental and theoretical results are presented in Tables 4.1 to 4.3 for several load torques and a range of drive frequencies. The measured and predicted system input and output powers are compared in Tables 4.1 and 4.2 respectively. Table 4.3 compares the system efficiencies calculated from the predicted and measured powers.

In Table 4.4, the computed motor, inverter and system efficiencies are separated. From this table the inverter efficiency is seen to be a

major component of the system efficiency, especially at low output frequencies, where the number of commutations per cycle is greatest.

The measurements of system efficiency were therefore due to power losses in both the inverter and the motor and not solely measurements of the motor efficiency.

OUTPUT FREQUENCY (Hz)	25 Nm LOAD			15 Nm LOAD			5 Nm LOAD		
	SYSTEM INPUT POWER (W)			SYSTEM INPUT POWER (W)			SYSTEM INPUT POWER (W)		
	Measured	Predicted	% Error	Measured	Predicted	% Error	Measured	Predicted	% Error
50	4681	4681	0.0	2939	2846	-3.16	1295	1344	3.78
45	4276	4279	0.07	2705	2637	-2.51	1228	1187	-3.34
40	3879	3848	-0.8	2502	2482	-0.8	1212	1216	0.33
35	3444	3455	0.32	2222	2250	1.26	1090	1079	-1.01
30	3022	3121	3.28	1959	2012	2.71	989	1021	3.24
25	2561	2629	2.66	1650	1697	2.85	836	888	6.22
20	2144	2330	8.68	1377	1417	2.9	720	749	4.03
15	-	-	-	1111	1139	2.52	615	634	3.09
10	-	-	-	825	864	4.73	478	496	3.77

Table 4.1 Measured and predicted system input powers

OUTPUT FREQUENCY (Hz)	25 Nm LOAD			15 Nm LOAD			5 Nm LOAD		
	SYSTEM OUTPUT POWER (W)			SYSTEM OUTPUT POWER (W)			SYSTEM OUTPUT POWER (W)		
	Measured	Predicted	% Error	Measured	Predicted	% Error	Measured	Predicted	% Error
50	3794	3824	0.76	2311	2301	-0.43	781	810	3.71
45	3412	3425	0.38	2079	2074	-0.24	703	723	2.84
40	3038	3040	0.07	1850	1846	-0.22	625	652	4.32
35	2644	2621	-0.87	1614	1623	0.56	546	559	2.38
30	2251	2248	-0.13	1378	1385	0.51	467	476	1.93
25	1854	1833	-1.13	1142	1149	0.61	389	410	5.4
20	1454	1433	-1.44	905	915	1.1	310	309	-0.32
15	-	-	-	668	660	-1.2	232	233	0.43
10	-	-	-	426	403	-5.4	153	156	1.96

Table 4.2 Measured and predicted system output powers

OUTPUT FREQUENCY (Hz)	INVERTER SWITCHING FREQUENCY (kHz)	25 Nm LOAD			15 Nm LOAD			5 Nm LOAD		
		SYSTEM EFFICIENCY			SYSTEM EFFICIENCY			SYSTEM EFFICIENCY		
		Measured %	Predicted %	% Error	Measured %	Predicted %	% Error	Measured %	Predicted %	% Error
50	0.9	81.1	81.7	0.74	78.7	80.9	2.8	60.3	64.8	7.46
45	1.17	79.8	80.0	0.25	76.9	78.6	2.21	57.2	61.0	6.64
40	1.36	78.3	79.0	0.89	73.9	74.4	0.68	51.5	53.7	4.27
35	1.47	76.8	75.9	-1.17	72.6	72.1	-0.69	50.1	51.8	3.39
30	1.80	74.5	72.0	-3.02	70.4	68.8	-2.27	47.3	46.6	-1.48
25	1.50	72.4	69.7	-3.73	69.2	67.7	-2.17	46.5	46.2	-0.65
20	1.68	67.8	63.4	-6.49	65.7	64.6	-1.67	43.1	41.3	-4.18
15	1.80	-	-	-	60.2	57.9	-3.82	37.7	36.8	-2.39
10	1.68	-	-	-	51.7	46.7	-9.67	32.0	30.3	-5.31

Table 4.3 Comparison of predicted and measured system efficiencies

OUTPUT FREQUENCY (Hz)	25 Nm LOAD			15 Nm LOAD			5 Nm LOAD		
	EFFICIENCIES (%)			EFFICIENCIES (%)			EFFICIENCIES (%)		
	MOTOR	INVERTER	SYSTEM	MOTOR	INVERTER	SYSTEM	MOTOR	INVERTER	SYSTEM
50	82.99	97.69	81.07	81.29	96.75	78.65	64.61	93.27	60.27
45	82.26	97.01	79.8	80.29	95.72	76.85	62.76	91.18	57.32
40	81.29	96.35	78.32	78.02	94.75	73.92	57.52	89.61	51.54
35	80.23	95.68	76.76	77.46	93.75	72.62	57.06	87.75	50.08
30	78.99	94.31	74.49	76.73	91.72	70.38	56.22	84.08	47.27
25	76.79	94.29	72.4	75.49	91.69	69.22	55.32	84.12	46.53
20	73.28	92.58	67.84	73.72	89.15	65.72	53.95	79.84	43.07
15	-	-	-	70.02	85.91	60.15	50.16	75.12	37.68
10	-	-	-	62.68	82.42	51.67	45.48	70.39	32.01

Table 4.4 Computed values of the drive component efficiencies

CHAPTER FIVE

COMPARISON OF PWM SWITCHING STRATEGIES

5.1 Introduction

The method presented in the previous three chapters for simulating an inverter/induction motor drive system, is used in this chapter to compare four popular PWM switching strategies, on the basis of system efficiency. The four strategies, namely duty ratio, naturally sampled modulation, harmonic elimination and distortion minimisation, are compared for increasing numbers of commutations (switching angles) per cycle to evaluate the "optimum" strategy at specific frequencies, for load torques of 1, 0.5 and 0.25 p.u. Comparisons are undertaken for the 4 kW drive described in Chapter 3, and also for a 30 kW drive of similar design.

The four PWM switching strategies are introduced in section 5.2 and the computed results are presented and discussed in section 5.3. A general discussion of the results of the comparisons together with conclusions are presented in section 5.4. Published works of a similar nature, and their relevance to this study, are also reviewed in this section.

5.2 The Chosen PWM Switching Strategies

PWM switching strategies may conveniently be segregated into two categories; those which may be achieved using analogue techniques (56,57), and those which must be generated digitally, using either microprocessors or dedicated LSI circuitry (58,59). Although these categories are adopted

in this chapter, it will no doubt be appreciated that the analogue strategies may also be generated digitally.

The four PWM strategies considered in this study are the most commonly referenced types. Quasi-square wave is not included because this strategy requires a variable-voltage supply and in order to limit the scope of this study, the restriction of a fixed-voltage dc rail was imposed. A variable dc power supply would, of course, represent an additional source of energy loss.

5.2.1 Analogue-generated PWM Switching Strategies: The switching angles for PWM strategies created using analogue methods are derived from the intersection points of a reference (or modulating) wave and a higher frequency carrier wave. The carrier wave is usually a triangular wave with a fundamental frequency which is a multiple of that of the reference wave. The carrier wave determines the number of switching angles, and consequently the number of "pulses" per cycle. The reference wave determines the width of these pulses and also the fundamental frequency and voltage of the resulting line waveform. Examples of this technique including several typical reference waveforms are given by Sen and Gupta (56). The two most common types, sine and square reference waves, were chosen for this study.

The PWM switching strategy whose angles are prescribed by the intersection points of a triangular wave and a square wave is referred to in the literature as duty ratio modulation (56), or variable ratio modulation (60). A typical example showing the generation of the inverter line voltages and the load phase voltage, is presented in Fig. 5.1. The mathematical derivation of the switching angles is outlined in section 8.3.1. The harmonic spectrum of this strategy is identical to

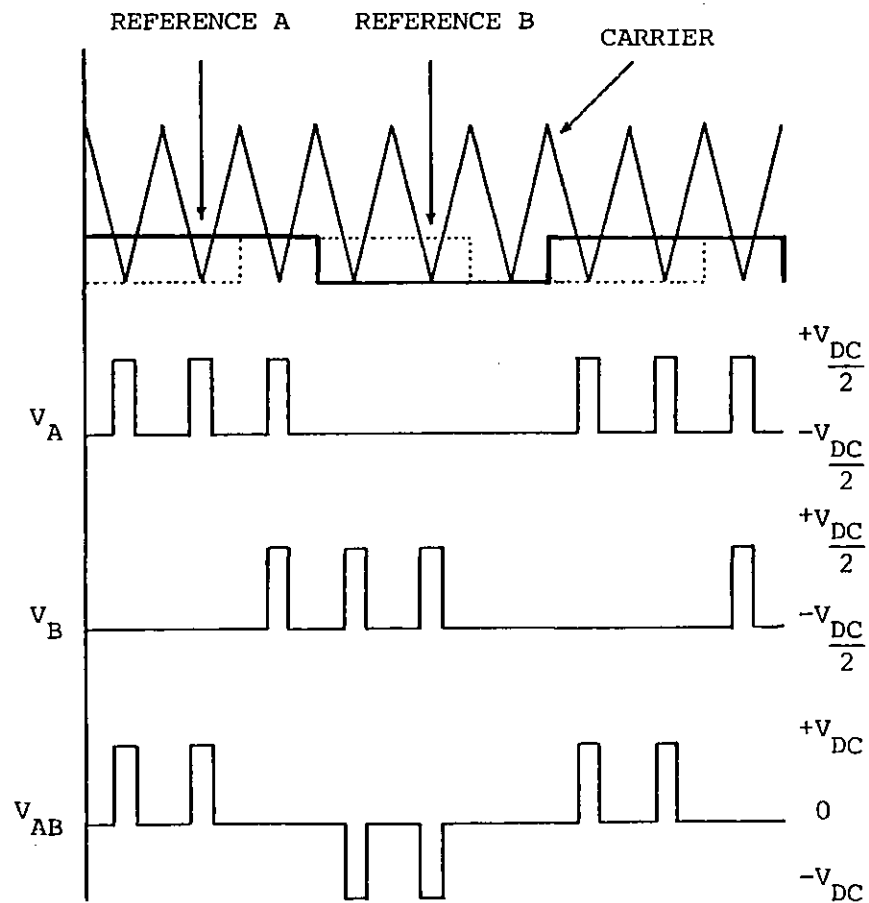


Fig. 5.1 Derivation of line and phase voltages for duty ratio modulation

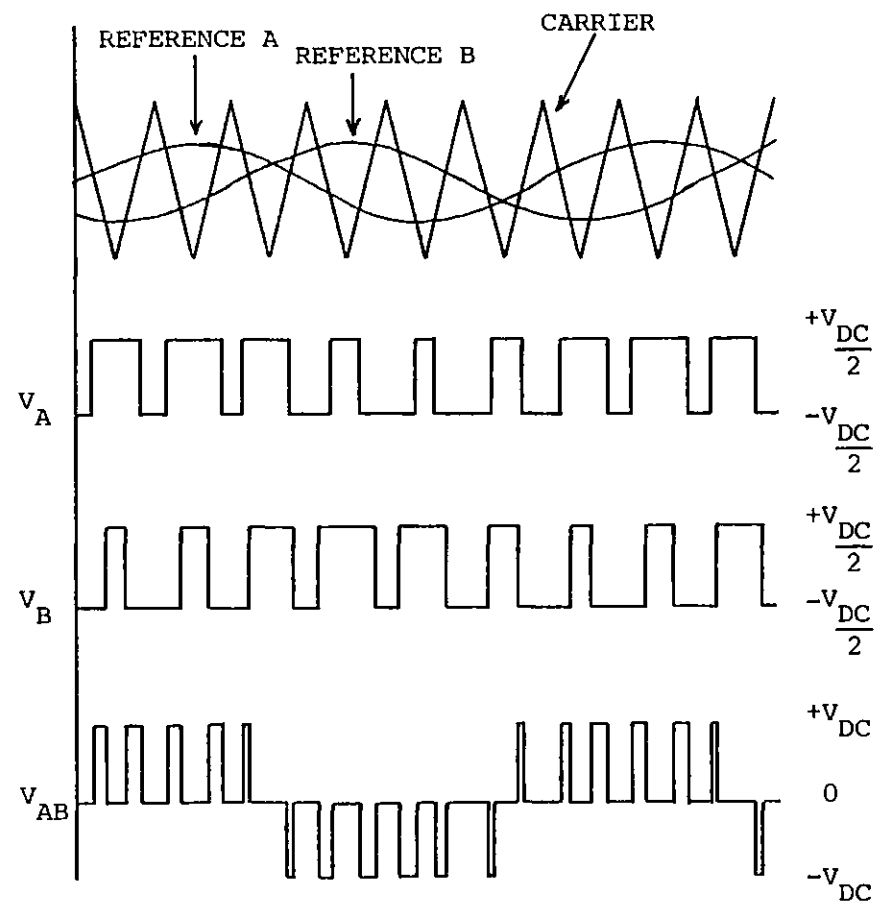


Fig. 5.2 Derivation of line and phase voltages for naturally sampled modulation

that of a quasi-square wave but includes additional harmonics at side-bands of the pulse frequency.

The switching angles in the second of the analogue PWM strategies are defined using a sinusoidal reference wave. This strategy is commonly referred to as either naturally sampled modulation (57), sine modulation (56) or subharmonic modulation (61). An example showing the generation of the line and phase voltage is given in Fig. 5.2 The mathematical calculation of the switching angles is dealt with in section 8.3.2. The generated waveforms are rich in harmonics, containing harmonics at frequencies of

$$f_H = pf_C \pm zf_R \quad p = 1, 2, \dots \quad z = 0, 1, 2, \dots \quad (5.1)$$

where f_C is the carrier frequency and f_R is the reference waveform frequency.

5.2.2 Digitally-generated PWM Switching Strategies: An inverter line waveform may be Fourier analysed to derive the magnitudes of the harmonics present, purely in terms of the waveform switching angles. For a waveform with 1/4 and 1/2 wave symmetry, the n^{th} harmonic voltage is given by:

$$\hat{V}_n = \frac{4}{n\pi} \left[1 + 2 \sum_{k=1}^M (-1)^k \cos(n\alpha_k) \right] \quad n = 1, 3, 5, \dots \quad (5.2)$$

where M is the number of commutations, or switching angles per 1/4 cycle, and α_k are the switching angles.

The two digitally-generated PWM switching strategies considered in

this study use this equation to calculate waveform switching angles which either eliminate a number of selected voltage harmonics or minimise some performance index.

The first of these strategies, termed harmonic elimination, was proposed by Patel and Hoft (58). For a waveform with M switching angles per 1/4 cycle, (M-1) harmonics can be eliminated and the fundamental voltage controlled. The mathematical principles of this method, together with the procedure for deriving the switching angles are presented in section 8.3.3.

The second type of digitally generated strategy involves the calculation of the switching angles to minimise a suitable function, such as the capital cost of filter components (62), or a factor representing the harmonic distortion in the inverter output current (13,59). The latter is the most commonly referenced type, the most popular form being the distortion minimisation strategy proposed by Buja and Indri(59). The switching angles are calculated to minimise the rms value of the harmonics in the inverter line current, I_{σ} , where

$$I_{\sigma} = \sqrt{\frac{1}{2} \sum_{n=1}^{\infty} \left(\frac{\hat{V}_n}{n\omega_0 L} \right)^2} \quad (5.3)$$

The procedure for deriving the switching angles is reviewed in section 8.3.4.

5.3 Comparison of Strategies

The investigation involving the four PWM strategies introduced in the previous section has two objectives. The first of these aims to show

that, for any strategy, an optimum number of commutations per cycle exists which will maximise system efficiency. This investigation involves calculating the system efficiency for a range of commutation numbers per cycle. To illustrate this, computed curves of motor, inverter and system efficiency are presented in Fig. 5.3. It will be seen from this figure that by increasing the number of switching angles (switches) per cycle, the motor efficiency will improve. The motor normally operates at a low slip value for the fundamental supply frequency. If higher frequencies are present, then the motor will be rotating with a greater slip with respect to them, and therefore at reduced efficiency. As the number of switches per cycle increases, the motor supply voltage resembles more closely a distortion free sinusoid and therefore the motor efficiency will increase until high-frequency iron losses become dominant. Thereafter further increase in switching frequency causes a reduction in efficiency. The inverter efficiency, on the other hand, will decrease because of the extra energy losses incurred as the number of commutation cycles increases. The system efficiency, which is obtained from the product of the motor and inverter efficiencies, will therefore exhibit a maximum at some switching frequency.

As a footnote, inverters are usually operated at their maximum switching frequency to produce waveforms with a low harmonic content. The principle of this being to achieve the highest possible motor efficiency, whilst assuming the inverter losses to be insignificant.

The second objective of the investigation is to determine which PWM strategy/switches per cycle combination will produce maximum system efficiency. The comparison of the four strategies was carried out over a range of frequencies from 10 Hz to twice rated frequency, 100 Hz for 1/4, 1/2 and full rated torque for the 4 kW motor.

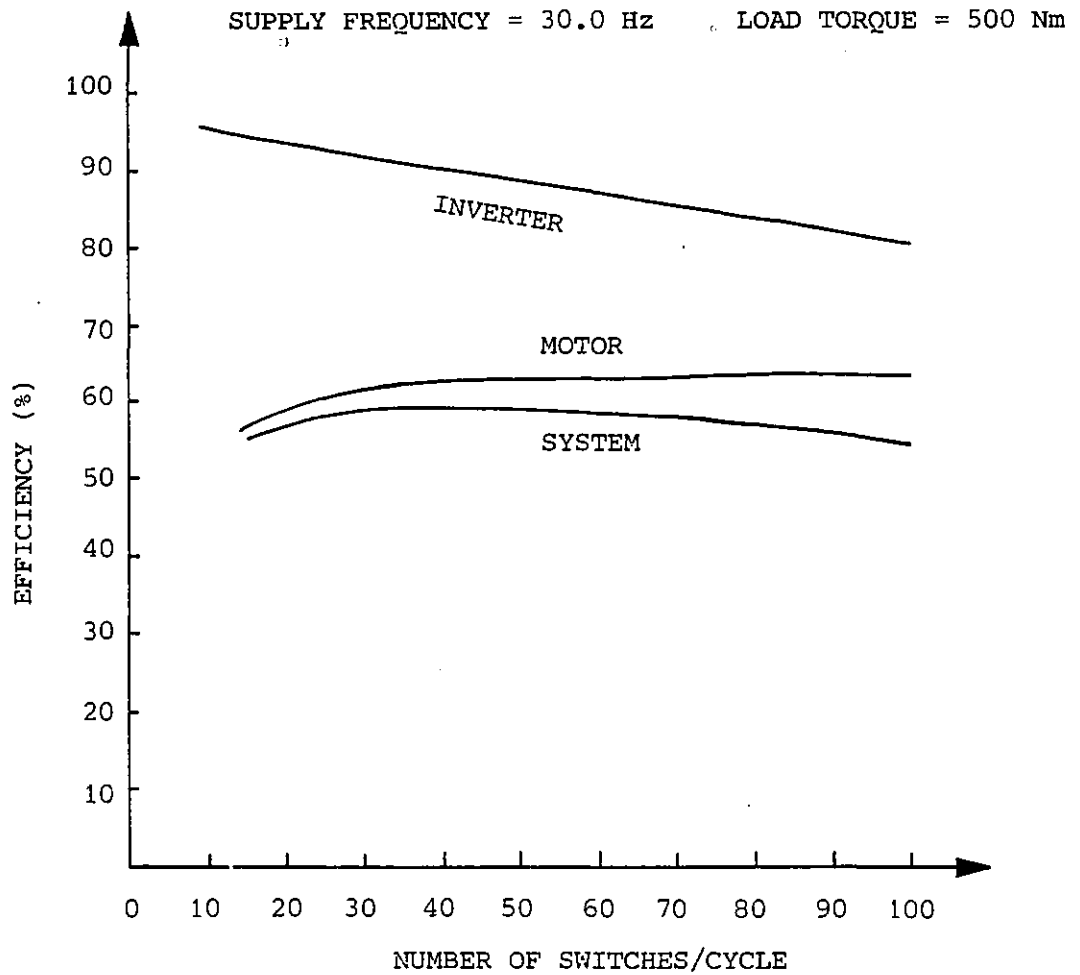


Fig. 5.3 Variation of component efficiencies with number of switches per cycle

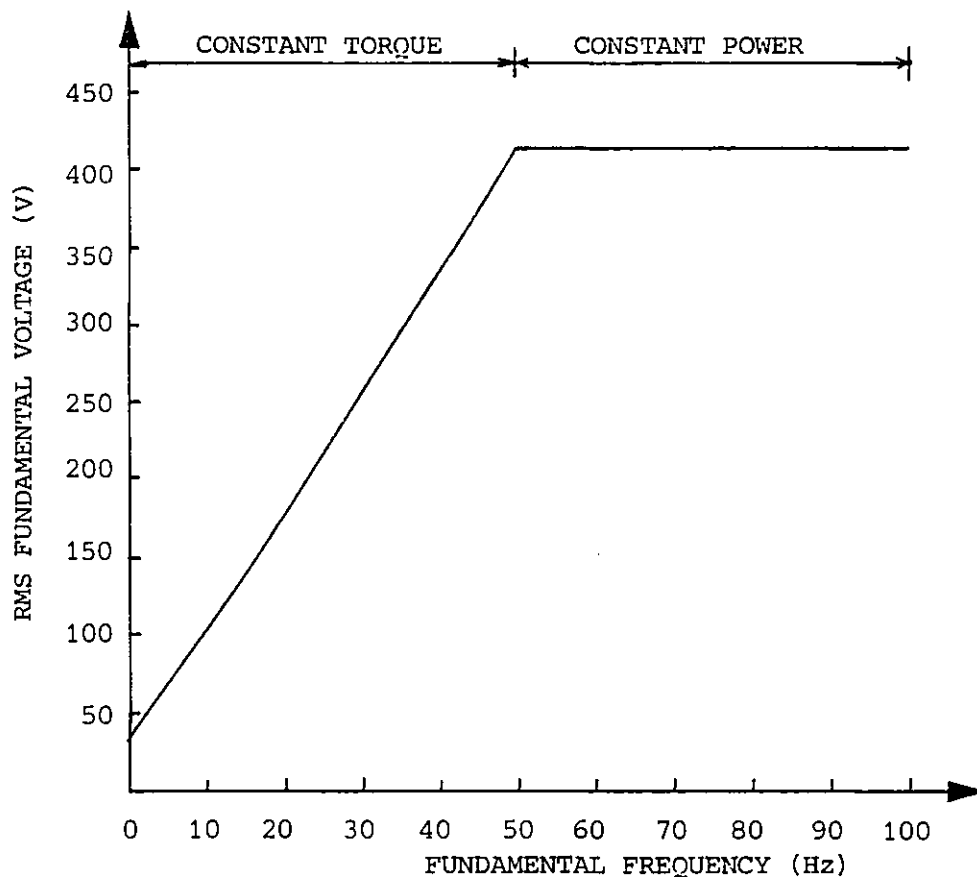


Fig. 5.4 Adopted V,f characteristic for 4 kW induction motor

System efficiency may also be maximised by adopting the fundamental voltage which maximises the induction motor efficiency at a prescribed frequency. This method is the subject of other research (1,10) and is not considered in this study. Therefore, to achieve a meaningful comparison of the strategies, a voltage-frequency (v,f) characteristic was strictly adhered to. The v,f characteristic was chosen to allow the 4 kW motor to operate at its designed flux level up to rated frequency. For frequencies above this point, the voltage remains constant at that for rated frequency. These two regions are referred to as the constant torque and constant power regions. The adopted v,f characteristic is presented in Fig. 5.4.

Pulses in the calculated PWM strategies which contravene the "minimum pulse width" criterion are dropped (see section 4.4). As a consequence, the fundamental voltage of the waveform will change, causing a departure from the specified voltage at that frequency. Strategies involving pulse dropping and whose fundamental voltage differed by greater than 1% from the specified voltage were ignored.

The investigations outlined above were carried out for the 4 kW drive discussed in the previous three chapters and also for a 30 kW drive of similar design. The 30 kW drive and its simulation are discussed in section 8.4.

5.3.1 Comparison of PWM Strategies for the 4 kW Drive

The computed results for the comparison are presented in Figs. 5.5 to 5.11. Curves have not been drawn through the points as some computed points do not lie on a smooth curve. The reasons for this are given later in the discussions of the individual strategies. The results

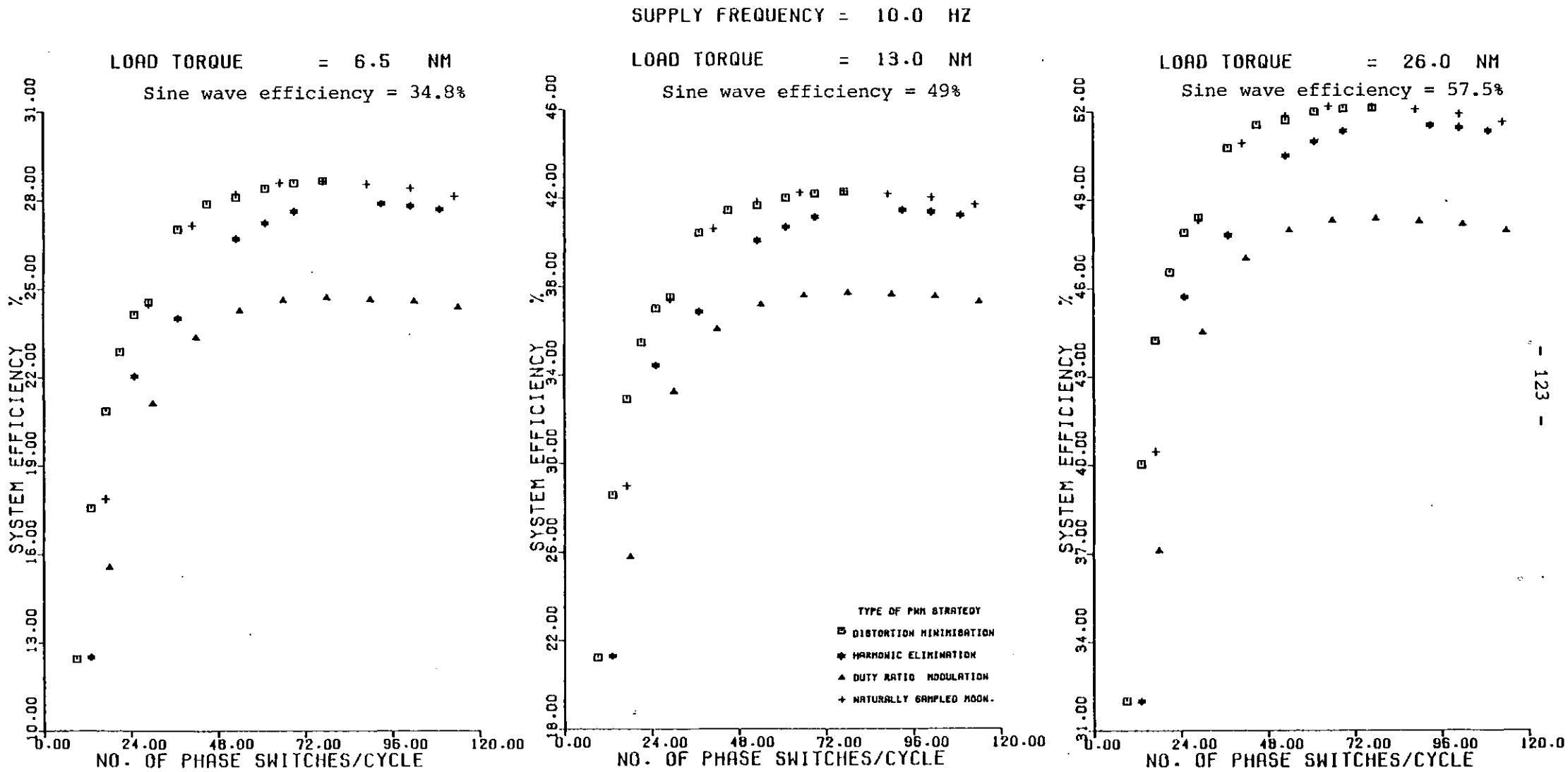


Fig. 5.5 Comparison of strategies for 4 kW drive, for an output frequency of 10 Hz

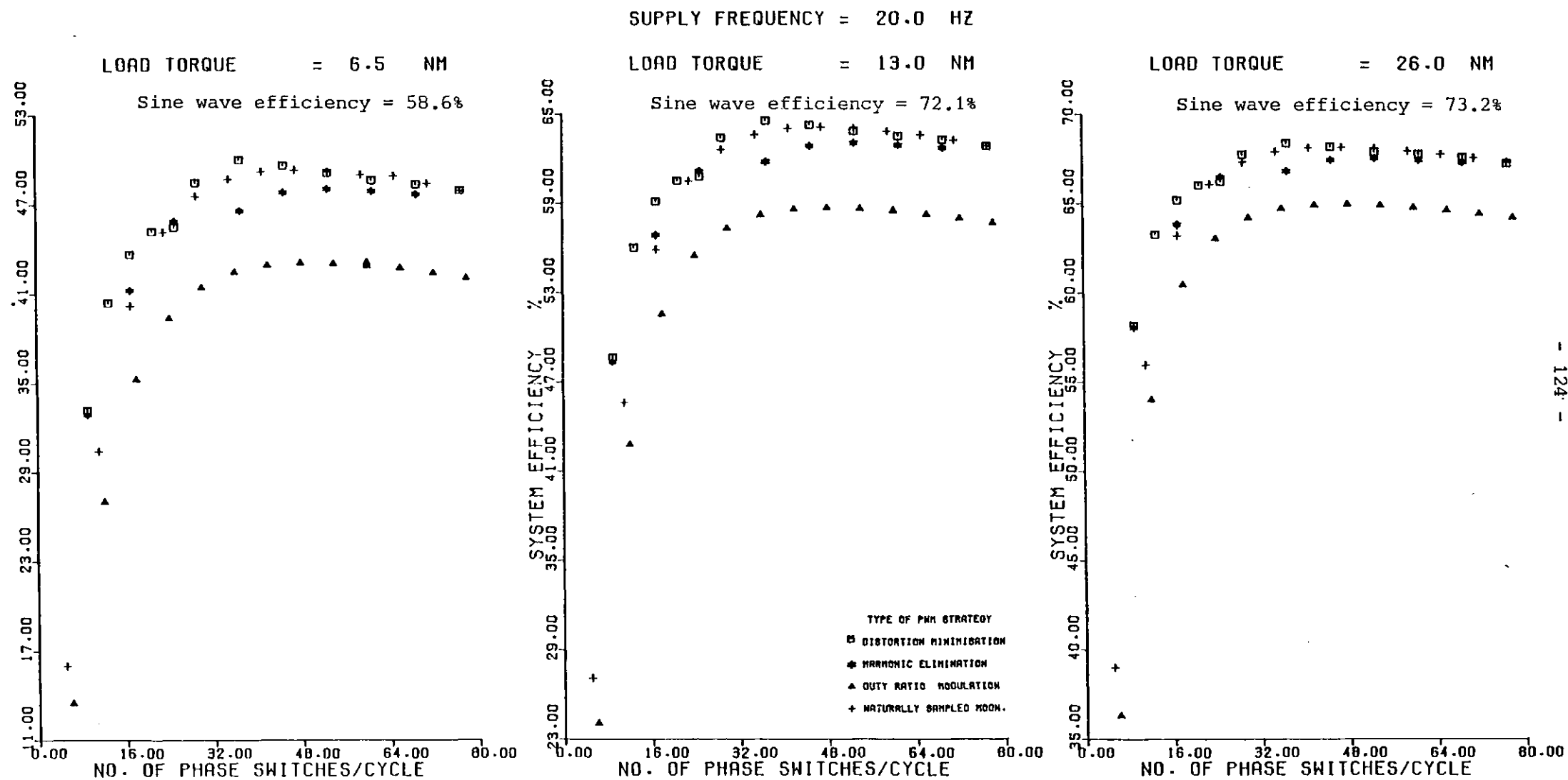


Fig. 5.6 Comparison of strategies for 4 kW drive, for an output frequency of 20 Hz

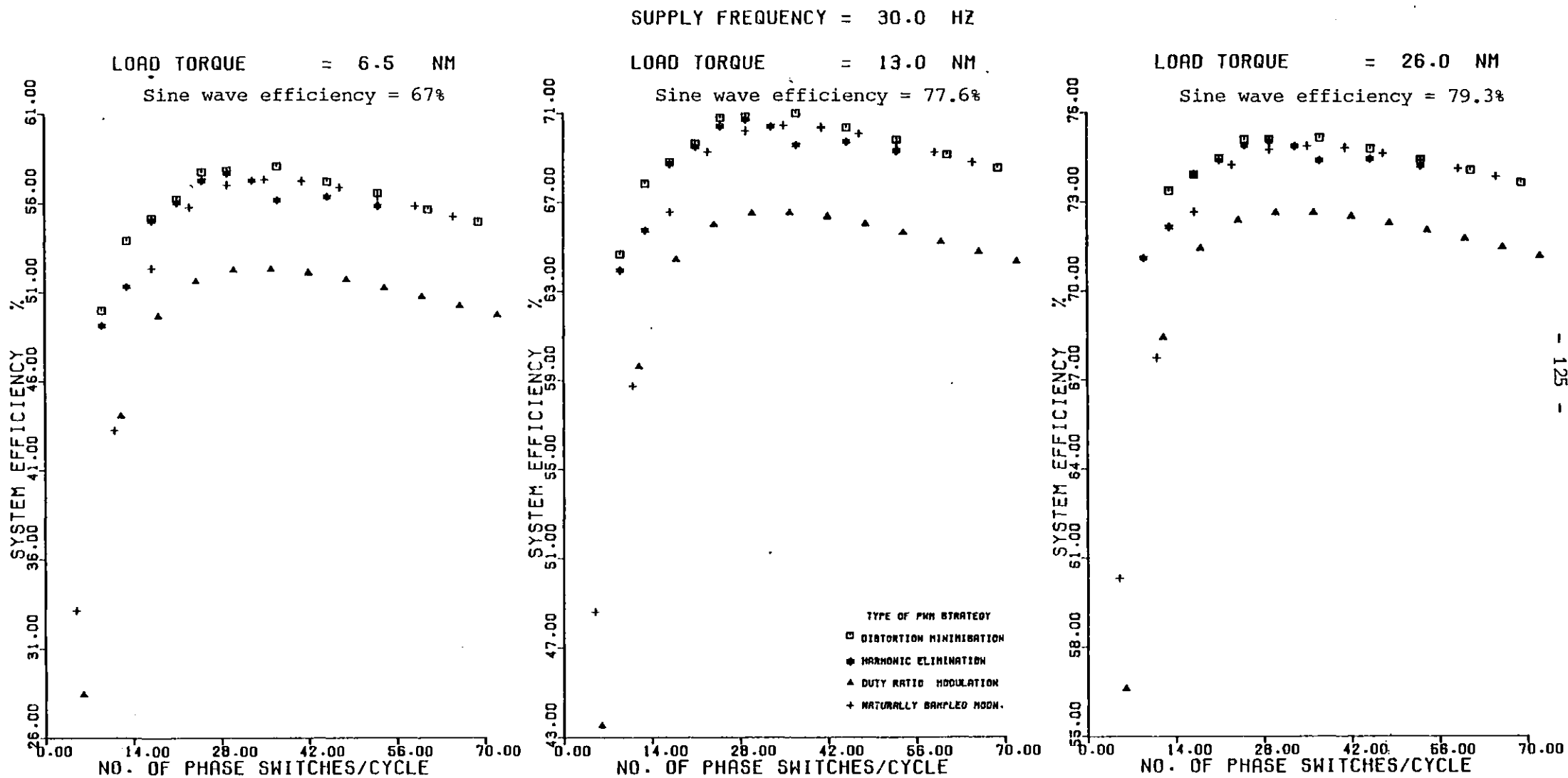


Fig. 5.7 Comparison of strategies for 4 kW drive, for an output frequency of 30 Hz

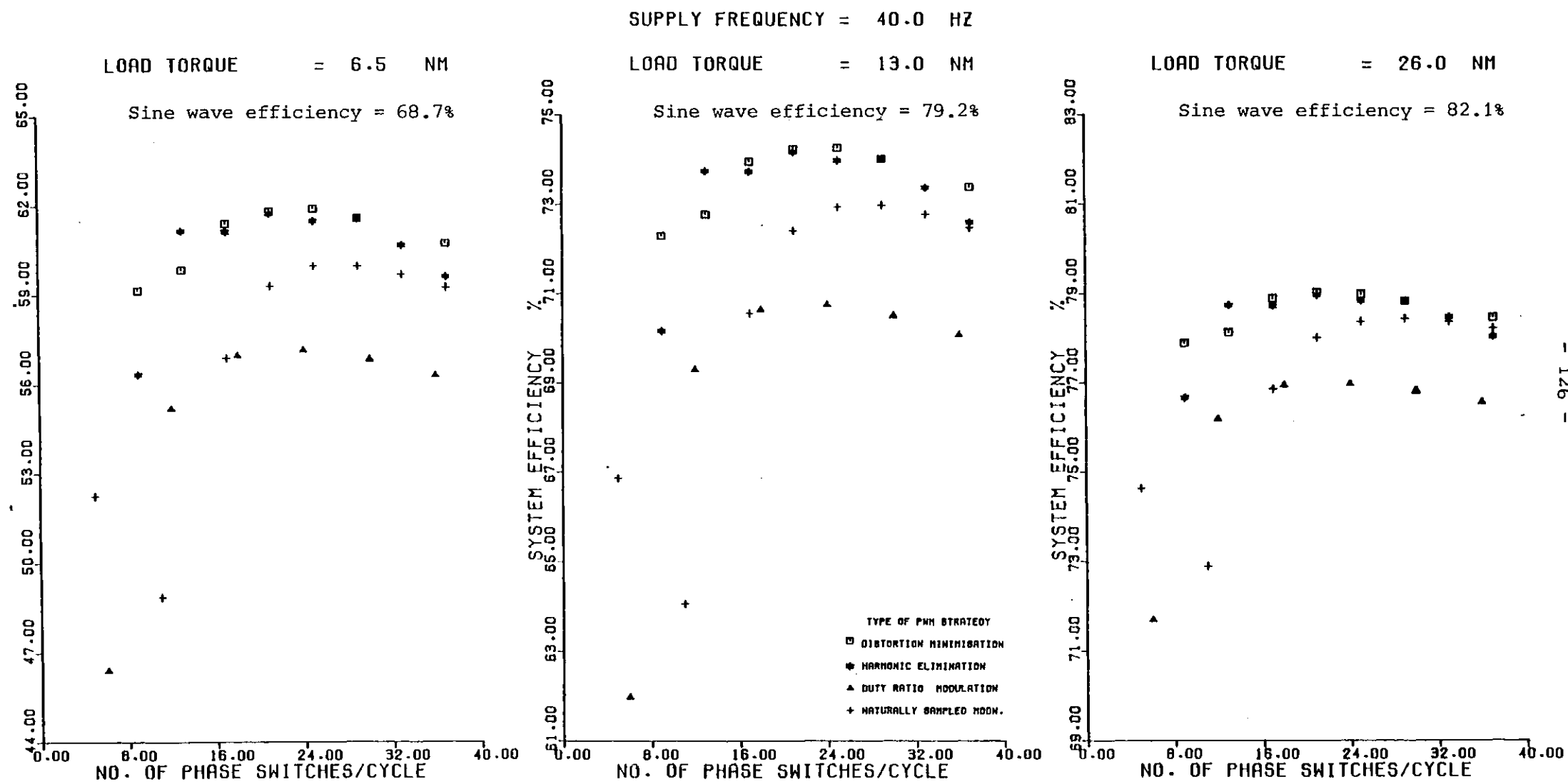


Fig. 5.8 Comparison of strategies for 4 kW drive, for an output frequency of 40 Hz

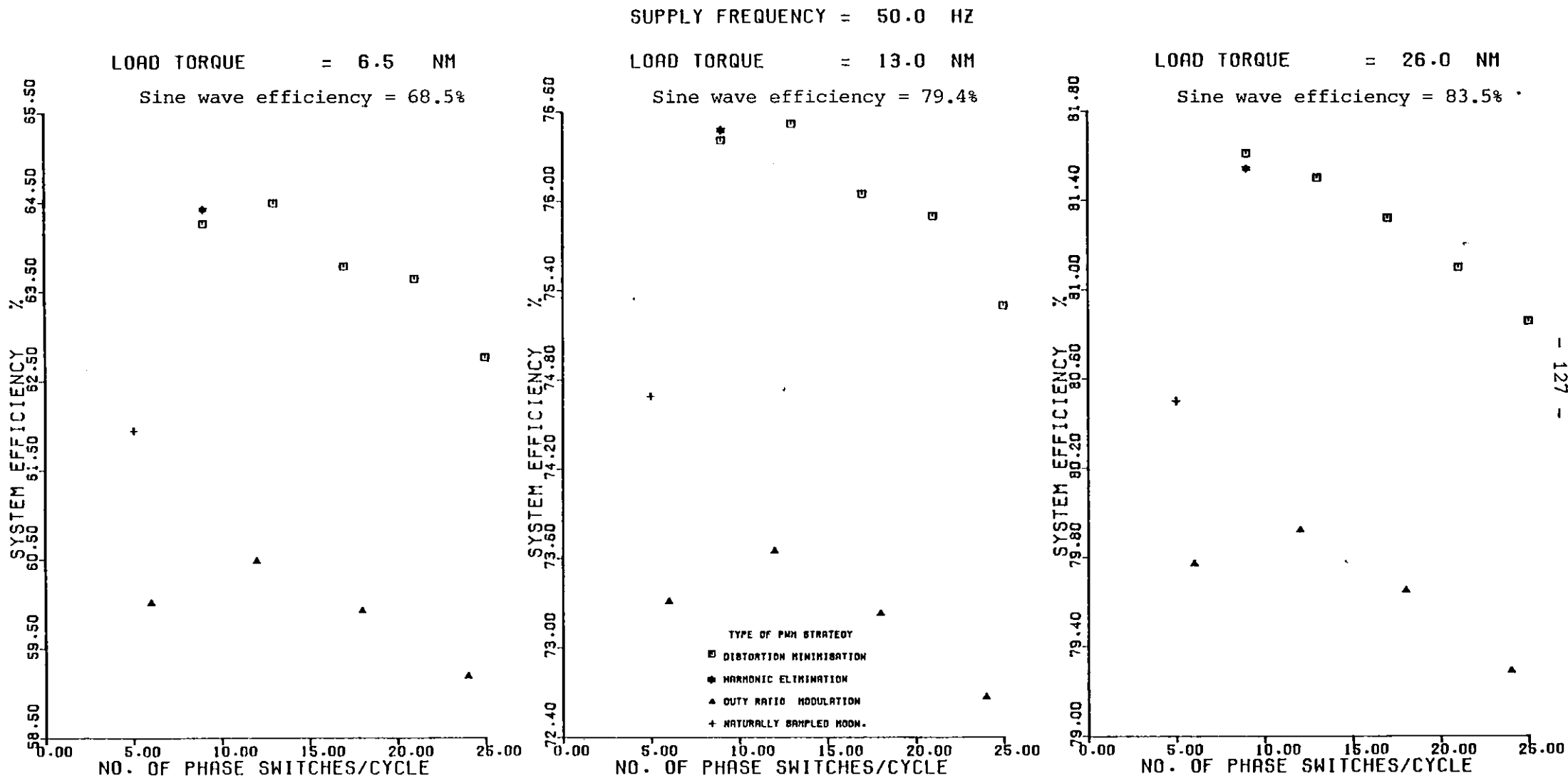


Fig. 5.9 Comparison of strategies for 4 kW drive, for an output frequency of 50 Hz

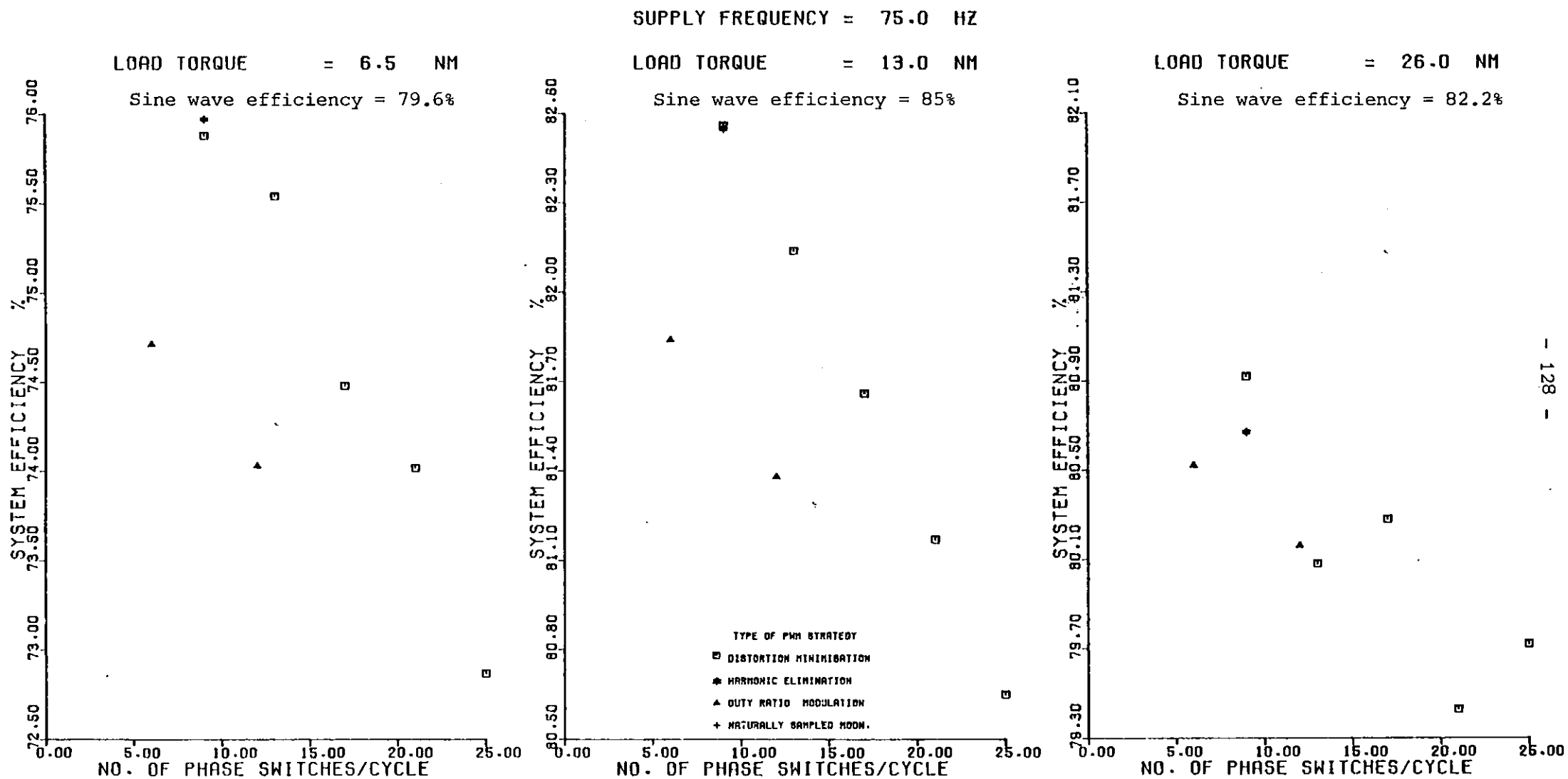


Fig. 5.10 Comparison of strategies for 4 kW drive, for an output frequency of 75 Hz

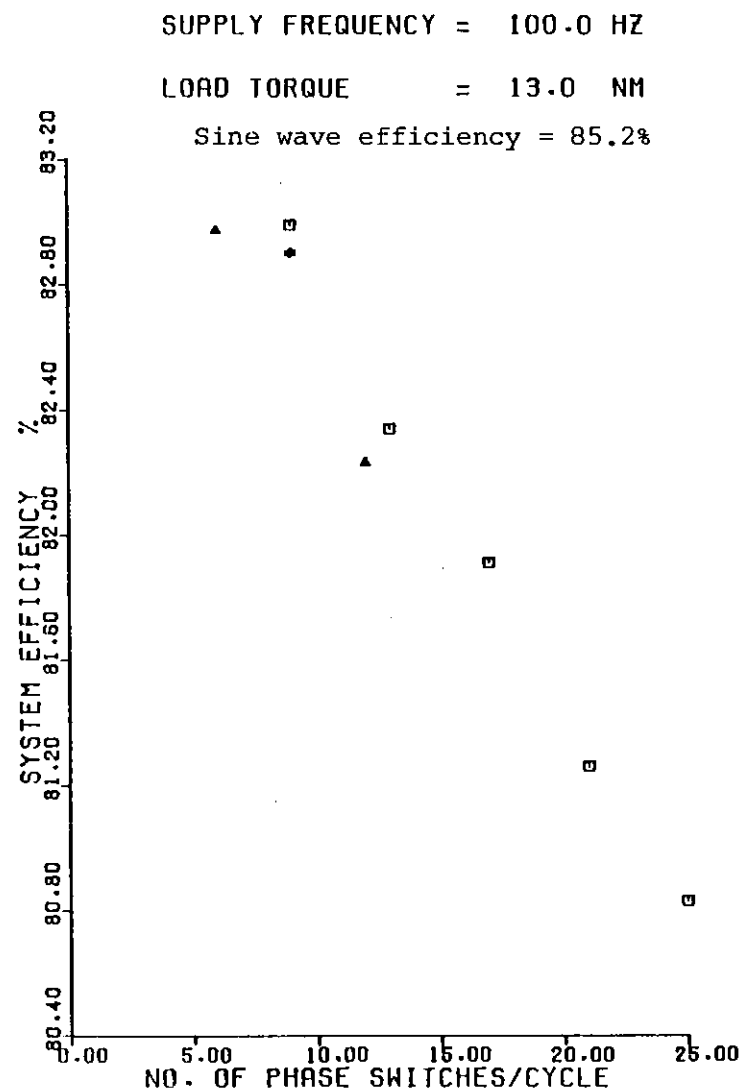
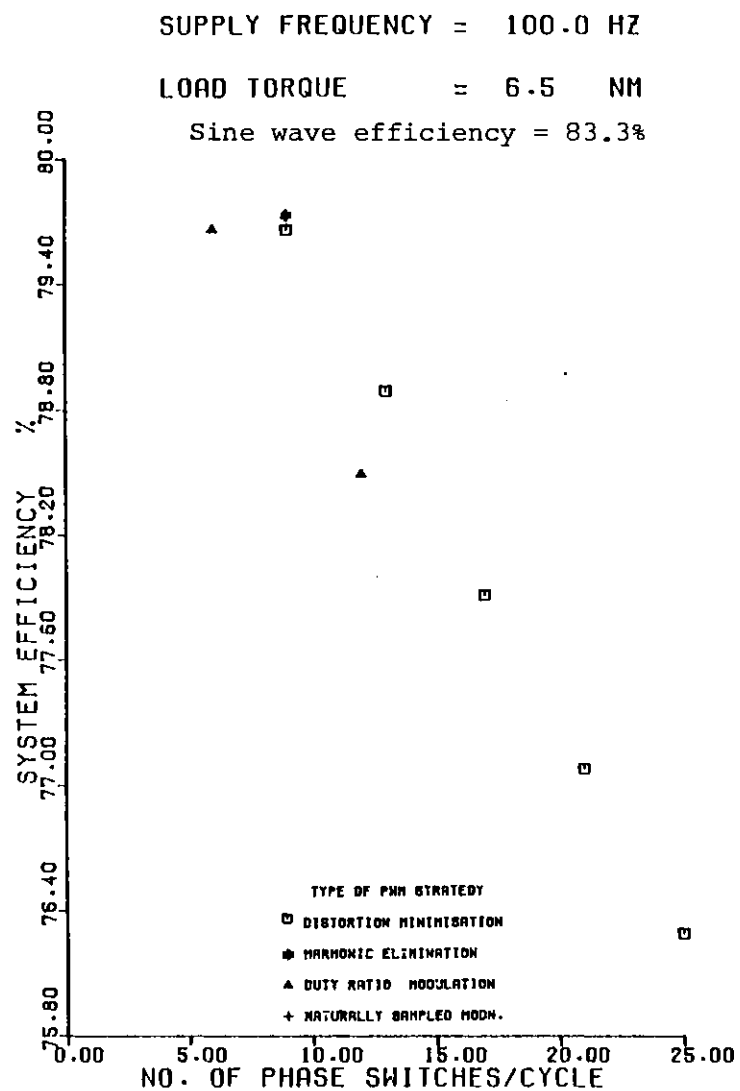


Fig. 5.11 Comparison of strategies for 4 kW drive, for an output frequency of 100 Hz

for some frequency-torque combinations are not presented as the required load torque at these frequencies was not achievable.

These figures show that the PWM strategies at each frequency, torque combination examined, exhibit a clearly defined maximum system efficiency at a specific number of switches per cycle. The profiles of the efficiency variations are mostly similar to the system efficiency variation depicted in Fig. 5.3, except at the higher frequencies where the maximum system efficiency occurs at the smallest number of switches per cycle possible. The decrease in system efficiency above the optimum number of switches per cycle is more marked at the higher frequencies.

Specific points relating to the individual strategies are now considered.

(i) analogue-generated strategies

Duty ratio modulation is shown to be the least efficient strategy for frequencies up to 50 Hz. Above that frequency it becomes a viable alternative to the more complicated digitally-generated strategies. Duty ratio modulation strategies which incur pulse dropping degenerate into a quasi-square wave and are therefore not included in the comparisons.

Naturally sampled modulation, on the other hand, compares favourably with the best (optimum) strategies for frequencies below 40 Hz. For 40 Hz, and above, this strategy becomes less effective for two reasons. Firstly, waveforms created using naturally sampled modulation with high fundamental voltages involve short duration pulses, which may be subject to pulse dropping, thereby causing changes in the waveform's harmonic profile. An example of this may be seen in the 40 Hz case (Fig. 5.8) where pulse dropping occurs for switching angle numbers greater than 8.

Secondly, the very nature of the derivation of the switching angles from the intersection points of two waveforms, means that a required number of switches per cycle may not be achievable. This is indicated in the 50 Hz case (Fig. 5.9) where only one pulse number is available.

(ii) digitally-generated strategies.

Distortion minimisation is shown in the computed results to be the optimum strategy at all frequencies, except for certain load conditions at the highest frequencies. Distortion minimisation is the most successful strategy because it minimises the total harmonic content of the motor line current on which motor efficiency is most dependent.

Anomalous points occur in the distortion minimisation curves, even though the distortion factor being minimised (see section 8.3.4) was always found to decrease with increasing number of switches per cycle. An example of this occurs in the 20 Hz case shown in Fig. 5.6, where the waveform with 25 switches per cycle does not attain the system efficiency expected when considering the results for the waveforms with 21 and 29 switches per cycle. These anomalous points may be explained in the following ways.

In distortion minimisation the switching angles are calculated to globally minimise a distortion factor. However, as explained in section 8.3.4, the minimisation process will converge to the nearest local minimum for a specific initial guess for the waveform switching angles. There is no mathematical means of establishing a global minimum, and so, an approach was adopted in which the global minimum is assumed to be the smallest of the local minima found using a large set of initial guesses. Although far fewer local minima were found than the number of initial guesses, it is possible that a local minimum, corresponding to the

global minimum, may have been missed. This could therefore lead to a waveform with a lower distortion factor than that for a waveform with fewer switching angles but which will not perform as well as the waveform corresponding to the true global minimum. An anomolous point may then be viewed as being due to waveform which does not represent a global minimum.

An alternative explanation is provided by close examination of the harmonic spectra for the calculated waveforms. In the minimisation of the distortion factor no direct attention is paid to specific harmonics, therefore it is possible for two waveforms with similar distortion factors to have widely differing spectral fingerprints. This is illustrated by considering the three waveforms in the previously cited example. On close inspection of the three harmonic spectra, the anomolous waveform (25 switches/cycle) was found to have its dominant harmonics at a lower frequency than the other two waveforms (21 and 29 switches). Therefore, because lower harmonics have a greater effect on the motor, the 25 switch waveform will incur larger losses than the 21 and 29 switch waveforms. Having recognized this phenomenon a further investigation was carried out on two 25 switch waveforms with similar distortion factors. The globally minimised waveform, with a distortion factor of 2.62×10^{-4} , was found to have its dominant harmonics around 480 Hz, whereas a waveform with a distortion factor of 2.78×10^{-4} had dominant harmonics around 600 Hz. This suggests that the waveform with the higher distortion should, in fact, be the better waveform. Indeed, this was verified using calculated values for the system efficiency; the result being that the waveform with the higher distortion factor yielded the better system efficiency. This observation highlights an inherent weakness of the distortion minimisation philosophy, showing

that it is insensitive to harmonic order.

Another explanation for the anomolous points is that the relative amounts of positive and negative sequence harmonics may effect the system efficiency. A positive sequence time harmonic causes losses in the motor, but also produces positive torque, which although produced at lower efficiency than that for the fundamental, will add to the nett forward torque. A negative-sequence time harmonic however causes losses in the motor and also produces a negative torque. Therefore, a waveform with a high concentration of positive-sequence harmonics will yield a greater system efficiency than one with a similar spectrum of negative-sequence harmonics. This particular explanation is extremely difficult to verify as the harmonic spectra of these waveforms consist of large numbers of both positive and negative sequence harmonics. It is, therefore, extremely difficult to extract the required data from the harmonic spectra. Nevertheless, these considerations once again point towards a certain insensitivity in the distortion minimisation process, arising from its lack of discrimination between positive and negative sequence harmonics. Considering the above explanations, a waveform corresponding to a global minimum may not always result in the optimum waveform as far as motor efficiency is concerned.

The anomolous points discussed above do not change with load torque, however the shapes of some curves are load torque dependent - these being at the higher frequencies. The reason for this is that the individual waveforms compared have slightly different fundamental voltages, caused not by pulse dropping, but by slight inaccuracies in the minimisation algorithm. The variations in the shape of the curves occur because the motor responds in different ways to slightly dissimilar fundamental voltages as load torque varies (9).

The other digitally-generated strategy, harmonic elimination is shown to be more favourable at higher frequencies, nevertheless it compares very favourably with the optimum strategy at all frequencies. The relatively poor performance of harmonic elimination at low frequency is explained as follows. Harmonic elimination seeks to eliminate a number of specified low order harmonics, but in doing so no attention is paid to the resulting higher order harmonics. Consequently, large high order harmonics become prevalent resulting in a detrimental effect on system efficiency. This effect is more pronounced at low fundamental frequencies because they are still relatively low multiples of the design frequency of the motor.

Anomalous points also occur in the harmonic elimination curves which are explained as follows. Firstly, successive waveforms may contain different concentrations of high-order harmonics (section 8.3.3 and Ref. 63) which would cause the computed efficiencies to deviate slightly from the expected smooth curve. Secondly, the relative concentrations of positive and negative sequence harmonics (as discussed above), remaining after the elimination process, may effect the system efficiency.

5.3.2 Comparison of PWM Strategies for the 30 kW Drive: The computed results for the 30 kW drive are presented in Figs. 5.12 to 5.17. The V,f characteristic used for the 30 kW motor was identical to that calculated for the 4 kW motor, therefore the switching angles for the PWM strategies are identical, except for distortion minimisation where the angles are calculated using a minimum pulse width appropriate for the 30 kW inverter.

The results show the same trends as those for the 4 kW drive, the

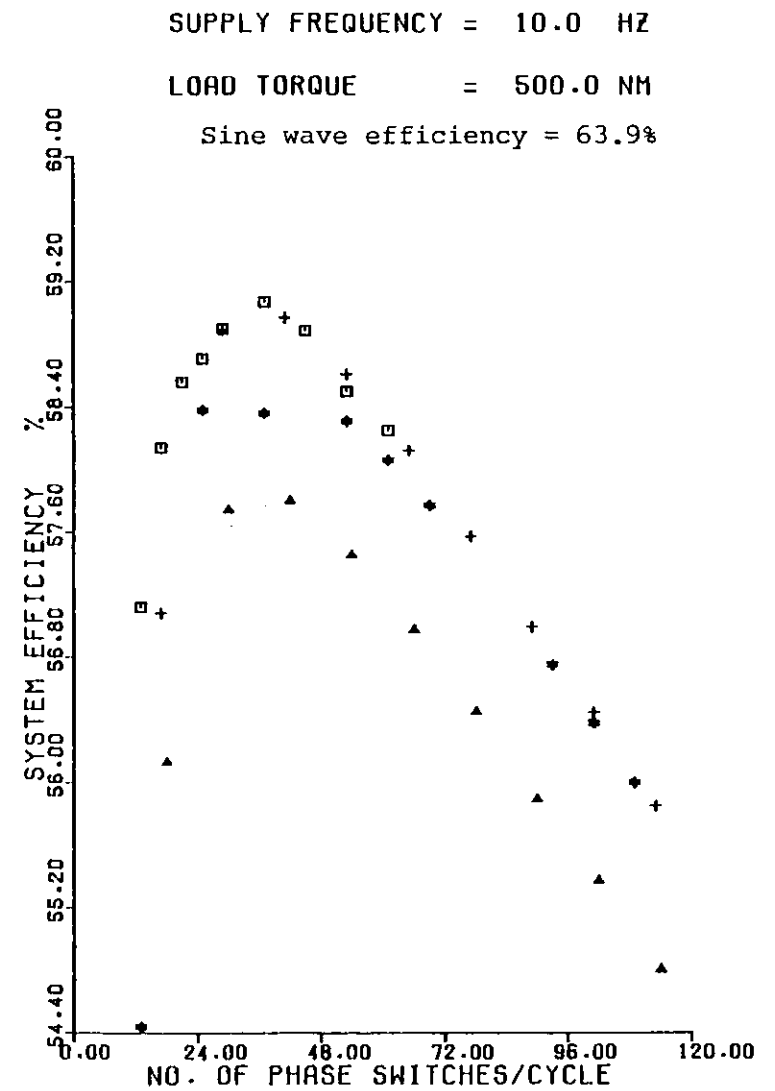
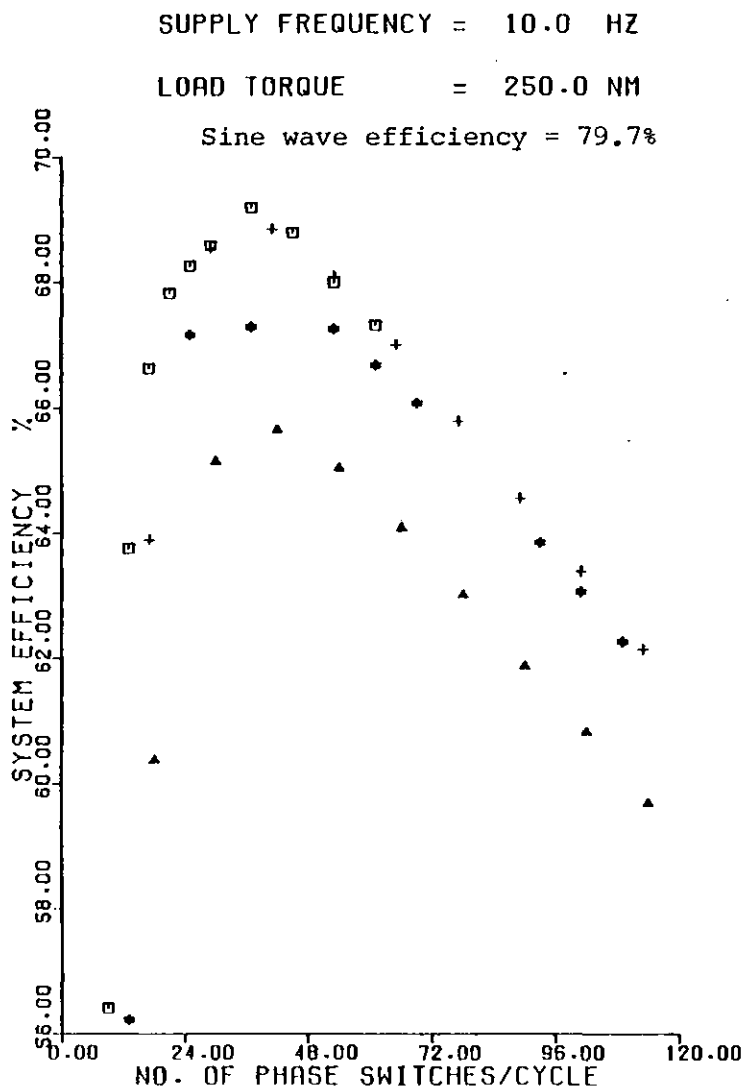


Fig. 5.12 Comparison of strategies for 30 kW drive, for an output frequency of 10 Hz

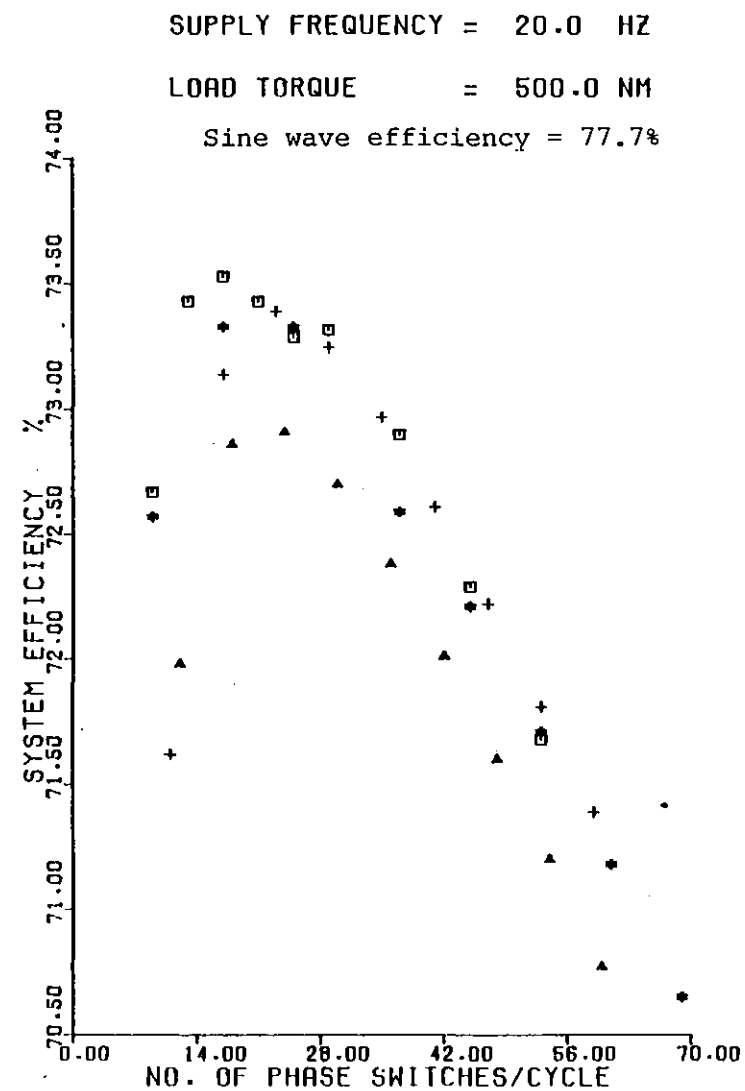
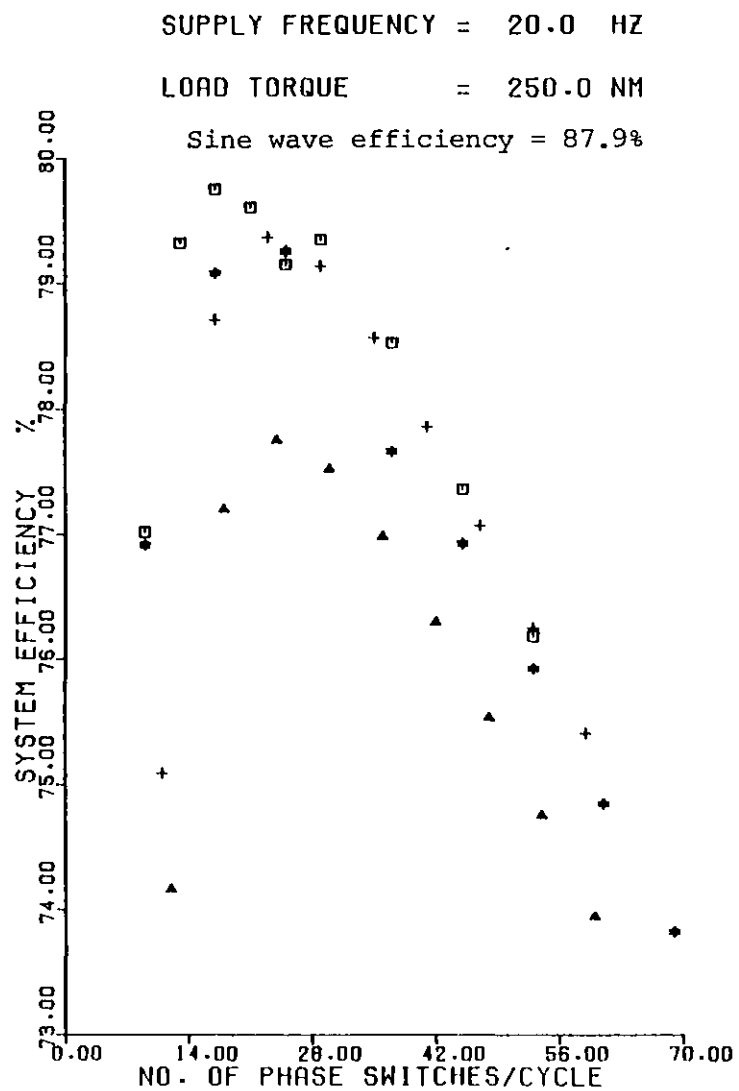


Fig. 5.13 Comparison of strategies for 30 kW drive, for an output frequency of 20 Hz

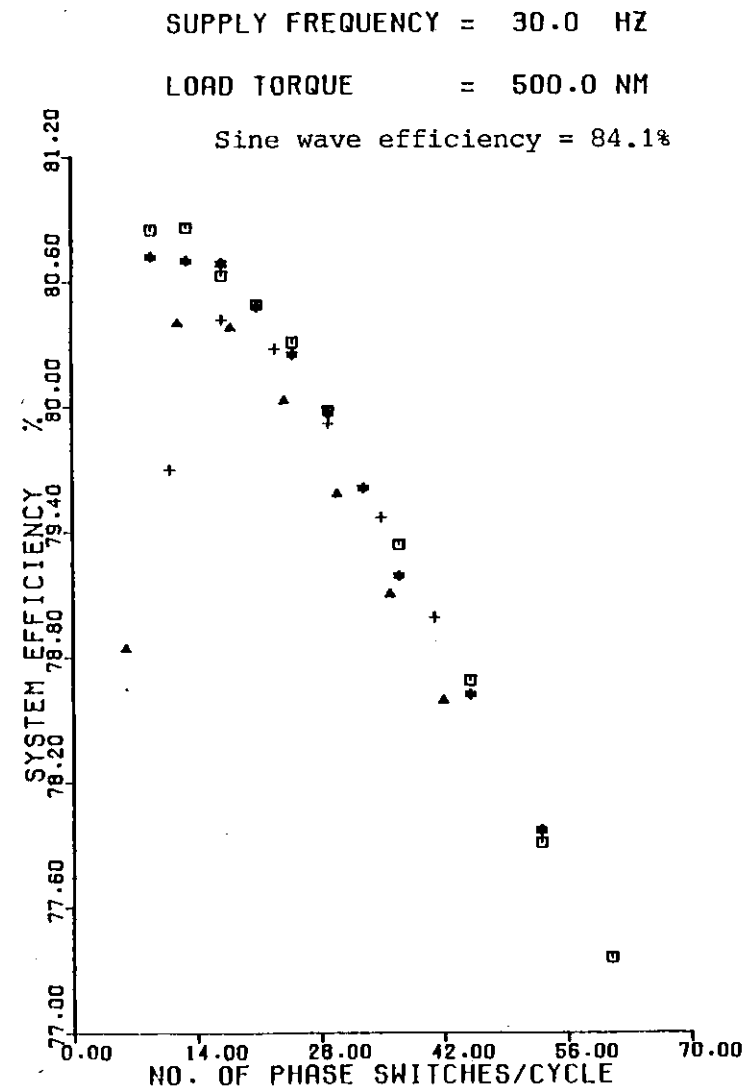
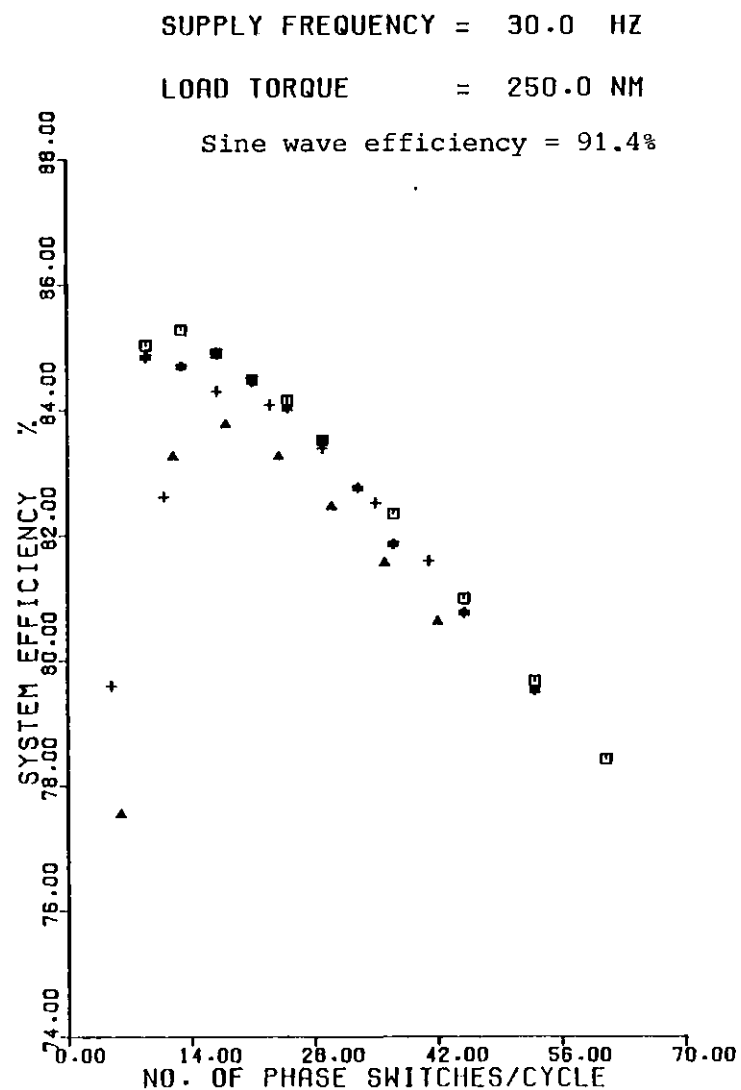


Fig. 5.14 Comparison of strategies for 30 kW drive, for an output frequency of 30 Hz

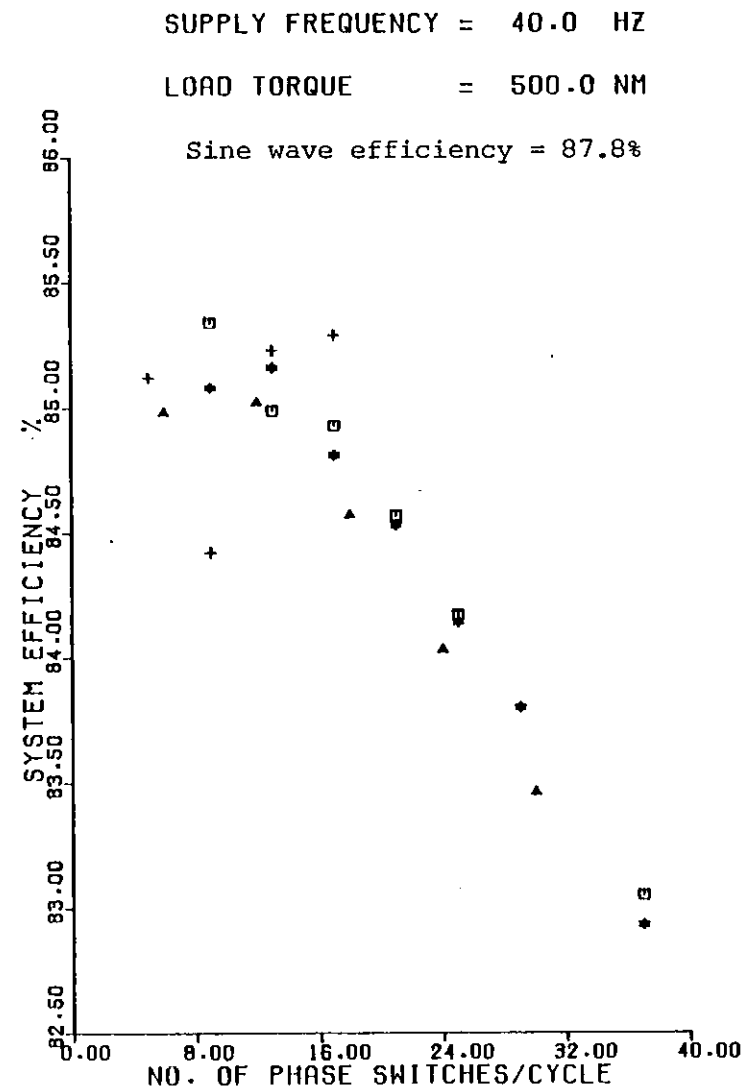
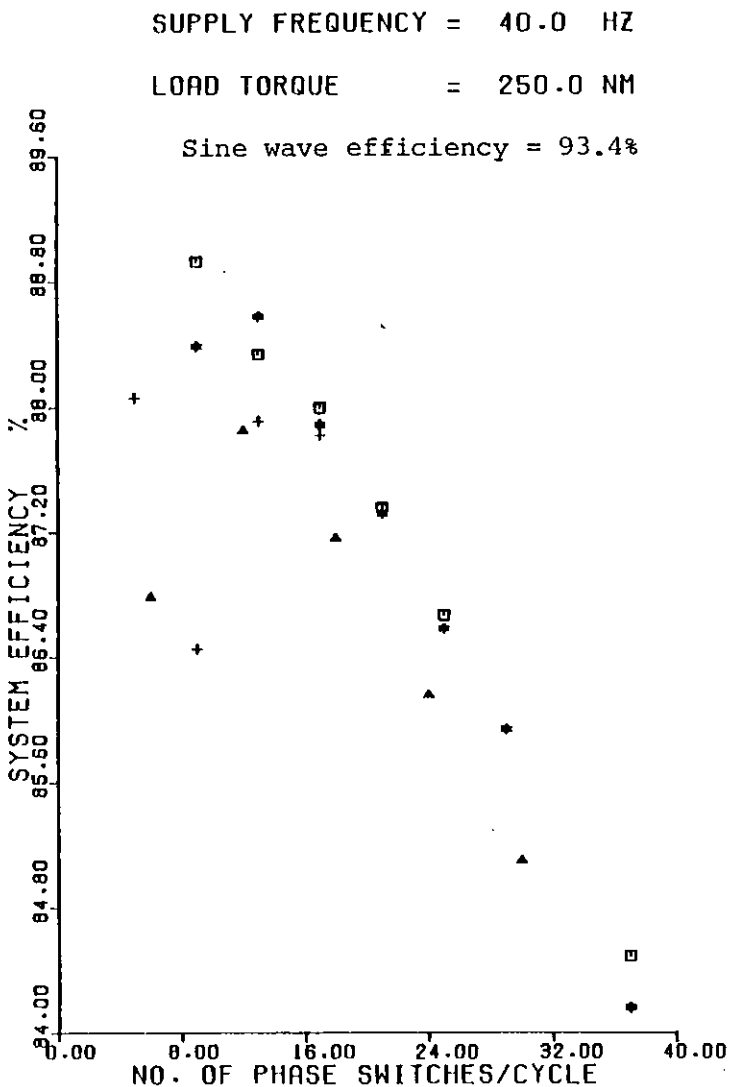


Fig. 5.15 Comparison of strategies for 30 kW drive, for an output frequency of 40 Hz

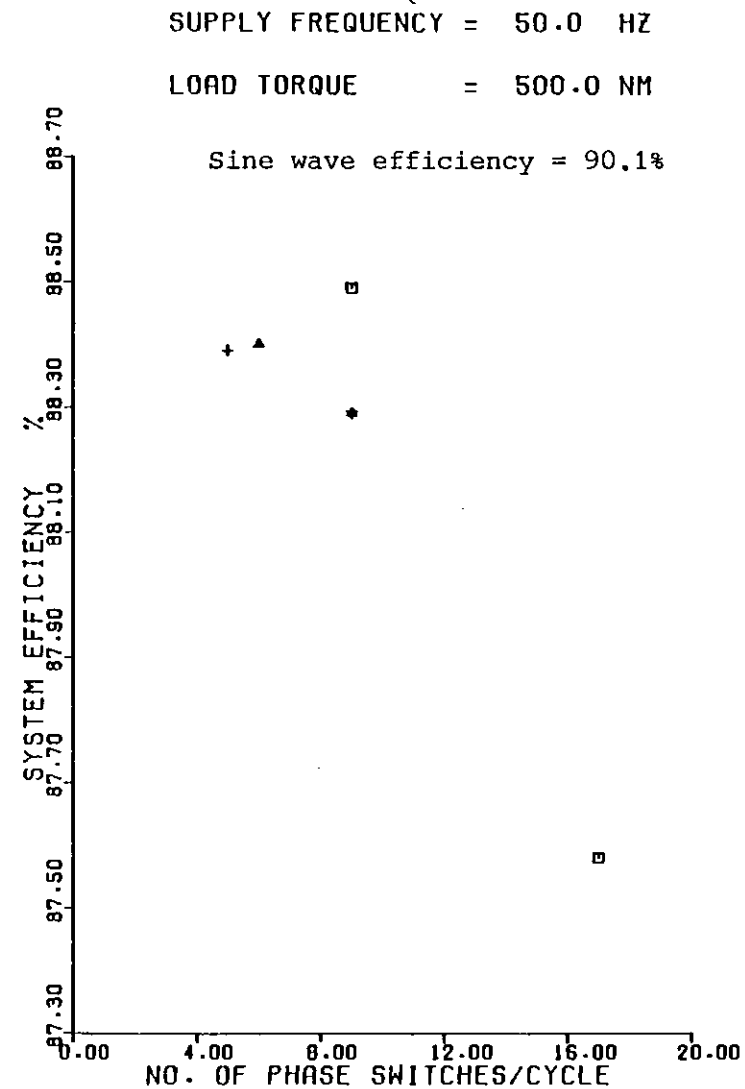
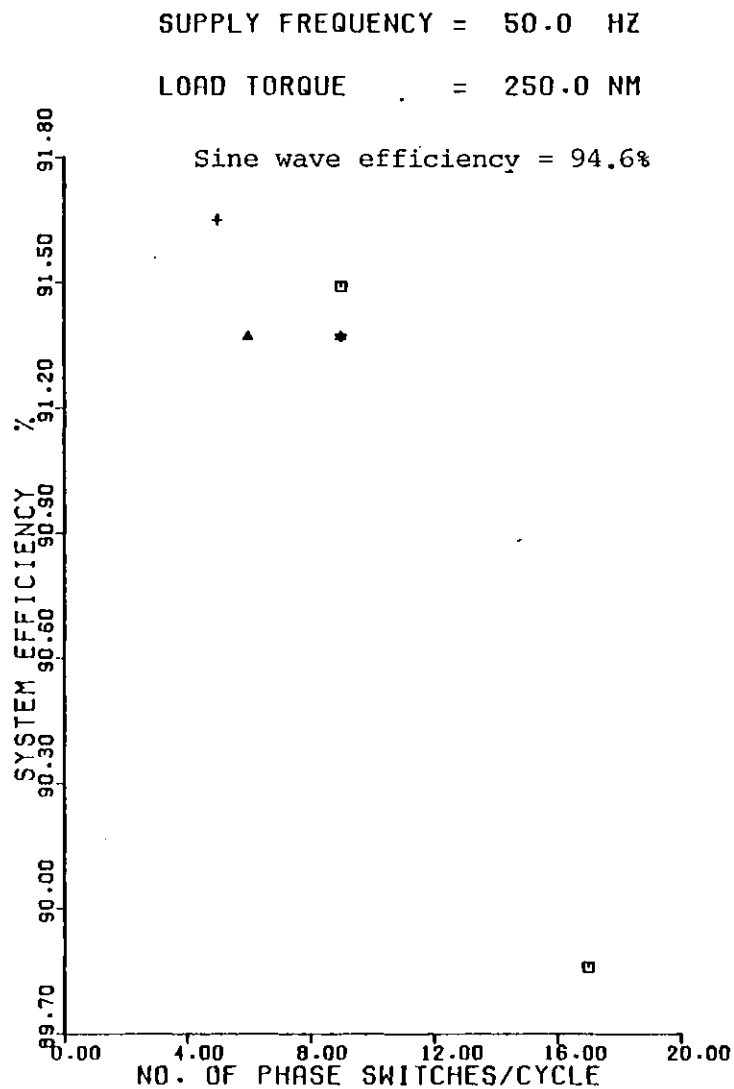
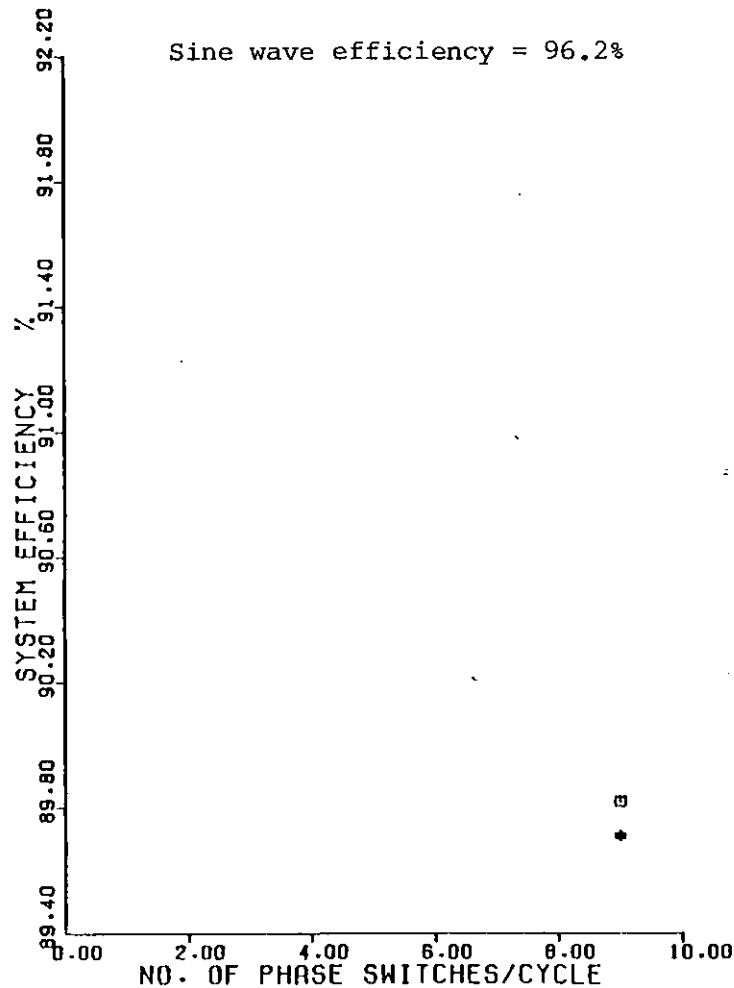


Fig. 5.16 Comparison of strategies for 30 kW drive, for an output frequency of 50 Hz

SUPPLY FREQUENCY = 75.0 HZ

LOAD TORQUE = 250.0 NM

Sine wave efficiency = 96.2%



TYPE OF PWM STRATEGY
□ DISTORTION MINIMISATION
* HARMONIC ELIMINATION
▲ DUTY RATIO MODULATION
+ NATURALLY SAMPLED MOD.

SUPPLY FREQUENCY = 100.0 HZ

LOAD TORQUE = 250.0 NM

Sine wave efficiency = 87.2%

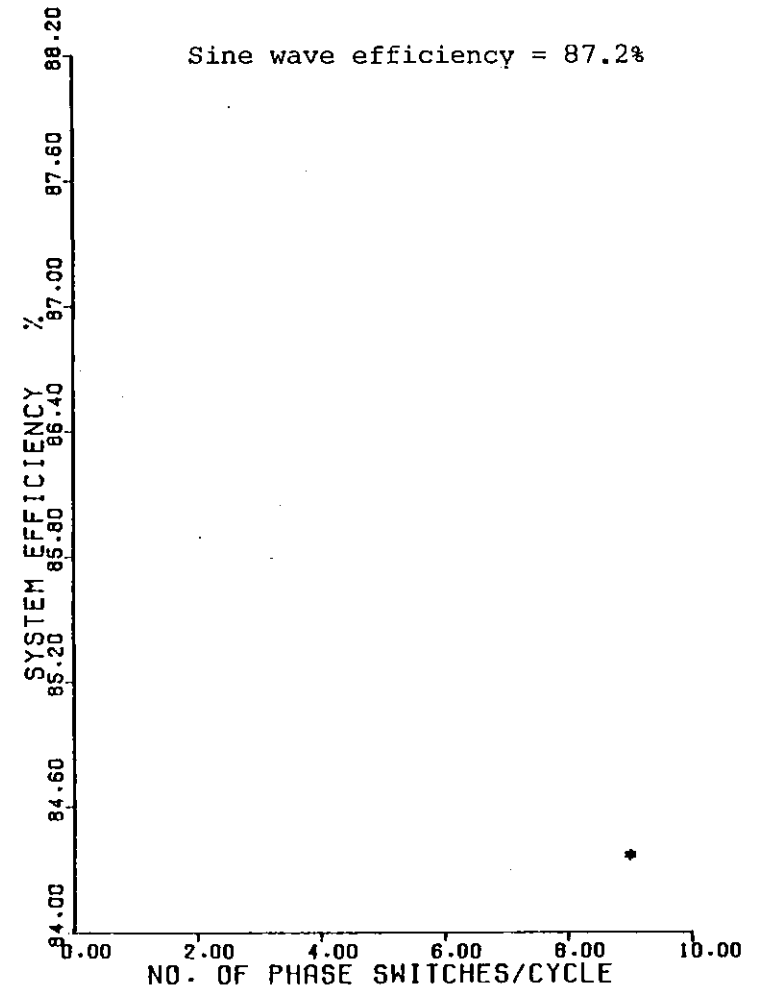


Fig. 5.17 Comparison of strategies for 30 kW drive, for output frequencies of 75 and 100 Hz

differences in efficiency between the four strategies being much smaller in the 30 kW case. The maximum system efficiency occurs at lower numbers of switches per cycle, indicating that the inverter commutation losses are more dominant in the 30 kW drive.

5.4 Discussion and Conclusions on Chapter 5

For both drives the digitally-generated strategies perform better than those generated using analogue methods. The increase in efficiency over naturally-sampled modulation, however, is only marginal. The hardware needed to implement the digital strategies is both more costly and more complex than that for the analogue strategies. It may therefore be prudent to accept the slight decrease in efficiency and employ the analogue-generated strategy of naturally sampled modulation.

If a digital method of generating the switching angles is to be adopted, naturally sampled modulation may still be the best choice of strategy because of the difficulties encountered in the calculation of switching angles for harmonic elimination and distortion minimisation. If the optimisation of system efficiency is the principle requirement, then distortion minimisation should be used.

The choice of the number of switches per cycle will depend on the drive used and should be varied with the inverter output fundamental frequency. The gains in efficiency that can be achieved warrant tailoring the PWM strategies and the number of switches per cycle for a particular drive.

The comparisons undertaken in this thesis have been concerned solely with system efficiency. Other criteria have been investigated in the literature (12,13,14). These studies have usually compared strategies

on the basis of the total rms current distortion in the motor line current, calculated using Equation 5.3. These studies were restricted to comparisons of strategies with identical numbers of commutations per cycle and also considered waveforms with no larger than 22 switches/cycle. The results show distortion minimisation to be the optimum strategy except for frequencies greater than 0.75 p.u., where harmonic elimination is better. Naturally sampled modulation is again shown to be only slightly worse than the optimum strategies over the whole frequency range.

Amongst the other comparisons considered are peak inverter current and motor pulsating torques (64). Reduction of pulsating torques requires the reduction of harmonic rotor currents, especially those of low order. Comparison of the strategies for torque pulsations (12,64) give the following results. Harmonic elimination has the lowest level of torque pulsations as it specifically eliminates the troublesome low order harmonics. Naturally sampled modulation significantly reduces the low order harmonics and causes relatively low level torque pulsations. Distortion minimisation reduces total harmonic distortion without paying any particular attention to the low order harmonics. Large pulsating torques are therefore developed using this strategy at low inverter output frequencies. Considering these points in conjunction with the results of this study, in situations where the reduction of pulsating torques is important, harmonic elimination represents the optimum strategy.

The criterion of peak inverter line current (64) is important when considering the design of an inverter. Of the four strategies considered here, the types generated digitally, especially distortion minimisation, produce the smallest peak currents.

CHAPTER SIX

CONCLUSIONS AND RECOMMENDATIONS FOR FURTHER WORK

This thesis may be considered as consisting of two parts, the first to develop a method of simulating an inverter/induction motor drive, the second to use this simulation in the comparison of the most popular PWM switching strategies.

The simulation of the inverter is based on a simple model of a conducting semiconductor, in conjunction with an analytical method of simulating the various conduction regimes during inverter operation. Despite its relative simplicity, this method proved satisfactory when calculated losses were compared with experimental measurements made on an inverter built to a commercial design. Nevertheless, further improvements in accuracy could be made if the high frequency characteristics of the semiconductor devices could be included in an equally empirical manner. This would permit device turn-on and turn-off losses to be estimated with reliability.

Simulating the inverter analytically requires detailed knowledge of the circuit operation. Numerical methods, which relieve this problem, may become more attractive as computing costs fall, particularly in situations where mini-computers may be employed. The secondary problem with numerical techniques is the lack of an accurate simple model for a thyristor. If this were overcome, through the development of a simulation package directly related to thyristor circuits, then numerical simulation may become more advantageous.

The induction motor model, which employs the harmonic equivalent circuit approach was shown to be satisfactory within the limits of this

constant speed investigation. The problems encountered, particularly concerning saturation, indicate that further work into the effect of non-sinusoidal supplies on motor parameters may be beneficial. For instance, how current is redistributed with frequency in closed rotor slots and how saturation dependent parameters vary with frequency. The motor simulation employed herein, using simple solutions to these problems, showed good agreement with experimental results. The complete drive model which utilises these two models was also shown to give reasonable agreement between theoretical and experimental results.

Several conclusions can be drawn from the comparison of PWM switching strategies, based on system %, carried out in the second part of this thesis. The PWM strategies realisable using analogue control circuitry are shown to perform well, in spite of their lack of sophistication. In particular, naturally sampled modulation compares well with digitally-generated strategies over the complete range of output frequencies. The digitally-generated PWM switching strategies are shown to be superior to the analogue-generated strategies with distortion minimisation representing the optimum strategy at most operating points. The digital strategies are, however, difficult to implement both because of the complexity of control circuitry required, and because of the difficulties in the derivation of waveform switching angles.

From the comparison it may also be seen that, for all PWM strategies, an optimum number of waveform switching angles always exists which maximises system efficiency. This suggests that careful consideration must be paid to the operational switching frequencies of inverters so that excessive losses are not produced.

One important fact to emerge from this study is the insensitivity of the digital strategies to individual harmonics and to the sequence of the harmonics. Distortion minimisation, in particular, pays no direct attention to individual harmonics other than by a simple $\left(\frac{V_n}{n} \right)$ weighting. A distortion minimisation strategy should therefore be investigated which includes suitable weighting factors for the more detrimental low order harmonics, as well as the negative sequence harmonics. Such a study should ideally be extensive to allow optimum weighting factors and their dependence on inverter and motor design to be investigated.

This study has been concerned solely with system efficiency, which although of major importance, may need to be considered along with other performance criteria. Some form of penalty function might be introduced to allow for these criteria, the size of the penalty being dependent on the importance of the added criteria.

The investigations in this thesis could also be extended to include other types of inverter, to include other drive components, such as the dc source, and to enable alternative switching devices, such as bipolar transistors, to be considered.

CHAPTER SEVEN

REFERENCES

1. GREEN, R.M., and BOYS, J.T.: "Inverter AC-drive Efficiency", Proc. IEE pt.B, 1982, 129, (2), pp 75-81.
2. MURPHY, J.M.D.: "Thyristor Control of AC Motors", (Pergamon Press, Oxford, 1973), Chapter 9.
3. WILLIAMS, F.C., LAITHWAITE, E.R. and EASTHAM, J.F.: "Development and Design of Spherical Induction Motors", Proc. IEE, 1959, 106(A), pp 471-484.
4. WILLIAMS, F.C., LAITHWAITE, E.R., EASTHAM, J.F. and FARRER, W.: "The Logmotor - A Cylindrical Brushless Variable Speed Induction Motor", Proc. IEE, 1961, 108(A), pp 91-99.
5. STARR, B.G. and van LOON, J.C.F.: "LSI Circuit for AC Motor Speed Control", Mullard Technical Publication, no. M82-0015.
6. DE BUCK, F.G.G.: "Design Adaptation of Inverter-supplied Induction Motors", Electric Power Applications, 1978, 1, (2), pp 54-60.
7. GARG, O.P. and SAXENA, R.B.: "Performance of Inverter Fed Induction Motor with Various System Parameters", J. Inst Eng. (India) Elec. Eng. Div., 1977, 58, (EL1), pp 45-50.
8. AVADHANLU, T.V. and SAXENA, R.B.: "Performance Evaluation and Redesign Aspects of Variable Speed Inverter Fed Induction Motor", Proc. ICEM, Pt. 2, 1978, Paper E3/2.
9. TSIVITSE, P.J. and KLINGSHIRN, E.A.: "Optimum Voltage and Frequency for Polyphase Induction Motors Operating with Variable Frequency Power Supplies", IEEE Trans. on IGA, 1971, IGA-7, (4), pp 480-487.
10. MURPHY, J.M.D. and HONSINGER, V.B.: "Efficiency Optimization of Inverter Fed Induction Motor Drives", IEEE-IAS, 1982 Annual Meeting Conference Record, pp 544-552.

11. BRADFORD, M.: "Improving Drive Efficiency by Electronic Enhancement", 1st European Conf. on Drives/Controllers, Leeds, 1982, pp 145-149.
12. MURPHY, J.M.D. and EGAN, M.G.: "An Analysis of Induction Motor Performance with Optimum PWM Waveforms", Proc. ICEM Pt.2, 1980, pp 642-655.
13. CASTEEL, J.B. and HOFT, R.G.: "Optimum PWM Waveforms of a Microprocessor Controlled Inverter", IEEE 1978 Power Electronics Specialists Conf., pp 243-250.
14. POLLMAN, A.: "Comparison of PWM Modulation Techniques", Proc. Conf. on Microelectronics in Power Electronics and Electrical Drives, 1982, Darmstadt, pp 231-236.
15. KLINGSHIRN, E.A. and JORDAN, H.E.: "Polyphase Induction Motor Performance and Losses on Non-sinusoidal Voltage Sources", IEEE Trans. on PAS, 1968, PAS-87, (3), pp 624-631.
16. HO, H.H.: "Improved Logic Model for Thyristor", Proc. IEE, 1973, 121, (5), pp 345-347.
17. HOLTZ, J. and WURM, H.P.: "A Dynamic Model for the Simulation of the Switching Properties of Thyristors", Proc. ICEM, 1980, PE7/3, pp 1152-1164.
18. CORNICK, J.A.F. and RAMSBOTTOM, M.J.: "Behaviour of Thyristors when Turned On by Gate Current", Proc. IEE, 1976, 123, (12), pp 1365-1367.
19. REVANKAR, G.N. and MAHAJAN, S.A.: "Digital Simulation for Mode Identification in Thyristor Circuits", Proc. IEE, 1973, 120, (2), pp 269-272.
20. BROWNE, T.G. and HOFT, R.G.: "Digital Simulation of Switching Transients in Thyristors", Conf. Record of IAS Annual Meeting, 1973, pp 401-412.
21. WILLIAMS, B.W.: "State-space Thyristor Computer Model", Proc. IEE, 1977, 124, (9), pp 743-746.

22. GHANI, S.N.: "Low Frequency Switching Circuit Model of a Thyristor", Computer Aided Design, 1979, 11, (5), pp 281-288.
23. KUTMAN, T.: "A Method of Digital Computation for SCR Cicuits", IEEE Trans. on IECI, 1974, IECI-21, (2), pp 80-83.
24. MELLIT, B. and RASHID, M.H.: "Analysis of DC Chopper Circuits by Computer Based Piecewise-Linear Technique", Proc. IEE, 1974, 121, (3), pp 173-178.
25. BECK, M.O.: "Efficiency and Performance of DC Chopper Circuits", PhD Thesis, University of Birmingham, 1975.
26. McMURRAY, W.: "Thyristor Commutation in DC Chopper - A Comparative Study", IEEE Trans. on Ind. Appl., 1978, IA-14, (6), pp 547-558.
27. HTSUI, J.S.C. and SHEPHERD, W.: "Method of Digital Computation of Thyristor Switching Circuits", Proc. IEE, 1971, 118, (8), pp 993-998.
28. REVANKAR, G.N. et al: "Computer Analysis of SCR Circuits", IEEE Trans. on IECI, 1975, IECI-22, (1), pp 48-55.
29. REVANKAR, G.N.: "Topolgical Approach to Thyristor Circuit Analysis", Proc. IEE, 1973, 120, (11), pp 1403-1406.
30. WILLIAMS, B.W.: "Complete State-Space Digital Computer Simulation of Chopper Fed DC Motors", IEEE Trans. on IECI, 1978, IECI-25, (3), pp 255-260.
31. LINDSAY, J.F.: "Measurement Problems in Determining the Efficiency of Thyristor-Supplied Motor Drives", IEEE Trans. on Ind. Appl., 1979, IA-15, (1), pp 8-13.
32. GOLDEN, F.B.: "Measure SCR Switching Losses The Easy Way", IEEE. Trans. on IECI, 1970, IECI-17, (4), pp 241-247.
33. TANI, T. et al: "Measuring System for Dynamic Characteristics of Semiconductor Switching Elements and Switching Loss of Thyristors", IEE Trans. on Ind. Appl., 1975, IA-11, (6), pp 720-727.

34. MATOUKA, M.F.: "A Wide-Range Digital Power/Energy Meter for Systems with Non-sinusoidal Waveforms", IEEE Trans. on Ind.Elect., 1982, IE-29, (1), pp 18-31.
35. PRENDERGAST, E.J. and JACKSON, R.D.: "Microcomputer-based Power Semiconductor Circuit Waveform Analyser", Proc. IEE, Pt. B, 1980, 127, (6), pp 363-367.
36. RAMSHAW, R.S.: "Power Electronics" (Chapman and Hall, London, 1973).
37. DEWAN, S.B. and STRAUGHEN, A.: "Power Semiconductor Circuits", (John Wiley and Sons Inc., Toronto, 1975).
38. LANDER, C.W.: "Power Electronics" (McGraw-Hill, Maidenhead, 1981).
39. ADKINS, B., and HARLEY, R.G.: "The General Theory of Alternating Current Machines", (Chapman and Hall, London, 1975).
40. O'KELLY, D., and SIMMONS, S.: "Introduction to Generalised Electrical Machine Theory", (McGraw-Hill, London 1968).
41. JORDAN, H.E.: "Digital Computer Analysis of Induction Machines in Dynamic Systems", IEEE Trans. on PAS, 1967, PAS-86, (6), pp 722-728.
42. DE SARKAR, A.K. and BERG, G.J.: "Digital Simulation of Three-Phase Induction Motors", IEEE Trans. on PAS, 1970, PAS-89, (6), pp 1031-1037.
43. BOWES, S.R. and CLEMENTS, R.R.: "Digital Computer Simulation of Variable Speed PWM Inverter Machine Drives", 1983, Proc. IEE, Pt.B, 130, (3), pp 149-160.
44. AL-NIMMA, D.A.B. and WILLIAMS, S.: "Modelling a Variable Frequency Induction Motor Drive", Electric Power Applications, 2, (4), pp 132-134.
45. HARASHIMA, F.: "On the Operating Characteristics of Induction Machines Fed by Thyristor Inverters", Report no SER-150, University of Japan, 1974.

46. WILLIAMSON, S., and EASTHAM, J.F.: "A Program Package for the Calculation of the Performance of an Induction Motor, Supplied from a Bridge Type Inverter", Report prepared for KGEL Ltd, Reading at Department of Engineering, Aberdeen University, October 1976.
47. BOWLER, P., and COUTO, C.: "Small Machines Operating on PWM Waveforms", IEE Small Machines Conf., London, September, 1981.
48. BUDIG, P-K. et al: "Theoretische Voraubestimmung des Betrieb-suerhaltens stromrichtergepeister Asynchronmaschinen", Elektrie, 1982, 36, (H.10), pp 507-510.
49. GÖL, Ö: "Modelling of Inverter/Induction Machine Drives", Proc. of ICEM, Brussels, 1980, (PE2/3), pp 670-677.
50. ALGER, P.L.: "Induction Machines", (Gordon and Breach, New York, 1970).
51. VEINOTT, C.G.: "Theory and Design of Small Motors", (McGraw-Hill, New York, 1959).
52. SAY, M.G.: "The Performance and Design of Alternating Current Machines", (Pitman Paperbacks, 1968).
53. BIRCH, T.S., and BUTLER, O.I.: "Permeance of Closed Slot Bridges and its Effect on Induction-Motor-Current Computations", Proc. IEE, 1971, 118, (1), pp 169-172.
54. BUTLER, O.I., and BIRCH, T.S.: "Comparison of Alternative Skew-Effect Parameters of Cage Induction Motors", Proc. IEE, 1971, 118, (7), pp 879-883.
55. WILLIAMSON, S. and SMITH, A.C.: "Field Analysis for Rotating Induction Machines and its Relationship to the Equivalent Circuit Method", Proc. IEE, Pt.B, 1980, 127,(2), pp 83-90.

56. SEN, P.C., and GUPTA, S.O.: "Modulation Strategies of Three Phase PWM Inverters: Analysis and Comparative Study", Can. Elec. Eng.J., 1979, 4, (2), pp 13-20.
57. BOWES, S.R., and CLEMENTS, R.R.: "Computer-aided Design of PWM Inverter Systems", Proc. IEE (B), 1982, 129, (1), pp 1-17.
58. PATEL, H.S. and HOFT, R.G.: "Generalised Techniques of Harmonic Elimination and Voltage Control in Thyristor Inverters: Part1 - Harmonic Elimination", IEEE Trans. on Ind .Appl., 1973, IA-9, (3), pp 310-317.
59. BUJA, G.S. and INDRI, G.B.: "Optimal Pulsewidth Modulation for Feeding AC Motors", IEEE Trans. on Ind. Appl., 1977, IA-13, (1), pp 38-44.
60. POLLACK, J.J.: "Advanced Pulsewidth Modulated Inverter Techniques", IEEE Trans. on Ind. Appl., 1972, IA-8, (2), pp 145-154.
61. SCHONUNG, A. and STEMMLER, H.: "Static Frequency Changers with Subharmonic Control in Conjunction with Reversible Variable Speed AC Drives", Brown Boveri Rev., 1964, 51, pp 555-577.
62. BUJA, G.S.: "Optimum Output Waveforms in PWM Inverters", IEEE Trans. on Ind. Appl., 1980, IA-16, (6), pp 830-836.
63. POLLMANN, A.: "A Digital Pulse Width Modulator Employing Advanced Modulation Techniques", 1982 IEEE Power Electronics Specialist's Conf. Proc., pp 116-121.
64. MURPHY, J.M.D., and EGAN, M.G.: "A Comparison of PWM Strategies for Inverter-fed Induction Motors", IEEE-IAS Ann. Gen. Meeting Proc., 1982, pp 569-573.
65. National Algorithms Group, Oxford, Fortran Subroutine Library, Mark 7, December 1978.
66. RABINOWITZ, P.: "Numerical Methods for Non-linear Algebraic Equations", (Gordon and Breach, 1970).

67. POLLMANN, A.: Personal Communication, Institut für Regelungstechnik, Technische Universität, Braunschweig.
68. LIWSCHITZ-GARIK, M.M.: "Computation of Skin Effect in Bars of Squirrel Cage Rotors", Trans. AIEE, 1955, 74, pp 768-771.
69. WILLIAMSON, S.: Unpublished results, Imperial College of Science and Technology, London.

CHAPTER EIGHT

8.1 Fourier Analysis of a Generalised 3-level Waveform

The generalised three level waveform shown in Fig. 8.1 can be Fourier analysed and represented as an infinite series of time-harmonics of the form,

$$v(\omega t) = \sum_{n=1}^{\infty} [V_{sn} \sin(n\omega t) + V_{cn} \cos(n\omega t)] \quad (8.1)$$

where

$$V_{sn} = \frac{1}{\pi} \int_0^{2\pi} v(\omega t) \sin(n\omega t) d(\omega t) \quad (8.2)$$

and

$$V_{cn} = \frac{1}{\pi} \int_0^{2\pi} v(\omega t) \cos(n\omega t) d(\omega t) \quad (8.3)$$

The waveform in Fig. 8.1 consists of a series of constant voltage periods, therefore the integrations in Equations 8.2 and 8.3 may be segregated into a series of (M+1) integrations over the constant voltage regions. Equation 8.2 therefore becomes

$$V_{sn} = \frac{1}{\pi} \sum_{k=1}^{M+1} \int_{\alpha_{k-1}}^{\alpha_k} v(\omega t) \sin(n\omega t) d(\omega t) \quad (8.4)$$

where $\alpha_0 = 0^\circ$ and $\alpha_{M+1} = 360^\circ$.

Evaluating the integral,

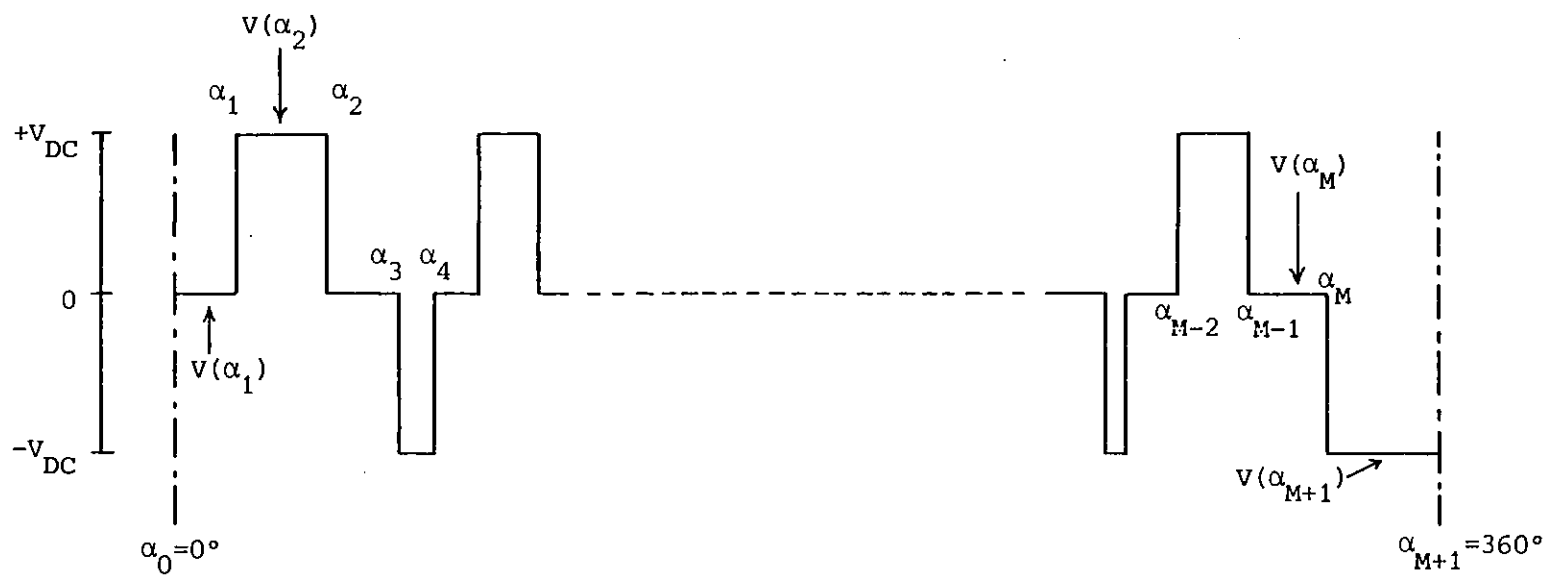


Fig. 8.1 Generalised representation of a 3-level waveform

$$v_{sn} = \frac{1}{\pi} \sum_{k=1}^{M+1} \left[\frac{v(\alpha_{k-1})}{n} \cos(n\alpha_{k-1}) - \frac{v(\alpha_k)}{n} \cos(n\alpha_k) \right] \quad (8.5)$$

For the period α_{k-1} to α_k , the value of the constant voltage level is given by $v(\alpha_k)$. Therefore,

$$v_{sn} = \frac{1}{n\pi} \sum_{k=1}^{M+1} v(\alpha_k) \{ \cos(n\alpha_{k-1}) - \cos(n\alpha_k) \} \quad (8.6)$$

Similarly,

$$v_{cn} = \frac{1}{n\pi} \sum_{k=1}^{M+1} v(\alpha_k) \{ \sin(n\alpha_k) - \sin(n\alpha_{k-1}) \} \quad (8.7)$$

Equation 8.1 may be more conveniently expressed as

$$v(\omega t) = \sum_{n=1}^{\infty} \hat{V}_n \cos(n\omega t + \theta_n) \quad (8.8)$$

where

$$\hat{V}_n = \sqrt{v_{sn}^2 + v_{cn}^2} \quad (8.9)$$

and

$$\theta_n = -\tan^{-1} \left(\frac{v_{sn}}{v_{cn}} \right) \quad (8.10)$$

8.2 Derivation of Parameters for Rotor Slot Top Leakage Calculations

The derivation of parameters used in the calculation of the test motor rotor leakage inductances (section 3.3.7) is presented below.

For a typical element, as shown in Fig. 3.10, the magnetic potential at the left hand side of the strip

$$A_n = A_{n-1} + H_N \delta x \quad (8.11)$$

where A_{n-1} is the magnetic potential at the right hand side of the strip and H_N is the average m.m.f. drop across the strip

$$H_N = \frac{1}{2}(H_n + H_{n-1}) \quad (8.12)$$

The average potential of the N^{th} section is given by

$$A_N = \frac{1}{2}(A_n + A_{n-1}) \quad (8.13)$$

For a slot m.m.f., A_S , the magnetic potential at the top of the slot centre line is $\frac{1}{2} A_S$.

The stator potential is also $\frac{1}{2} A_S$, because there is no m.m.f. drop across the airgap at the slot centre line. The slot m.m.f. enclosed by a flux line at a height y above the semi-circle centre line is

$$A_S \left(\frac{a_y}{a_S} \right) \quad (8.14)$$

where a_S is the area of the slot and a_y is the area of the slot below the flux line. The magnetic potential on the slot centre line at this point is therefore

$$\frac{1}{2} A_S \left(\frac{a_y}{a_S} \right) \quad (8.15)$$

The average potential of the N^{th} strip on the slot centre line is denoted by A_{SN} . The m.m.f.'s across the airgap and the slot top for the N^{th} section are respectively

$$F_{\text{GN}} = (A_{\text{N}} - \frac{1}{2}A_{\text{S}}) \quad (8.16)$$

$$F_{\text{SN}} = A_{\text{N}} - A_{\text{SN}} \quad (8.17)$$

The airgap and slot top fluxes are calculated as

$$\phi_{\text{GN}} = \lambda_{\text{GN}} F_{\text{GN}} w' \quad (8.18)$$

$$\phi_{\text{SN}} = \lambda_{\text{SN}} F_{\text{SN}} w' \quad (8.19)$$

where λ_{GN} and λ_{SN} are the airgap and slot top permeances

$$\lambda_{\text{GN}} = \frac{\mu_0 \delta x}{g} \quad (8.20)$$

$$\lambda_{\text{SN}} = \frac{\mu_0 \delta y}{(x + \frac{1}{2}\delta x)} \quad (8.21)$$

8.3 Calculation of PWM Strategy Switching Angles

8.3.1 Duty Ratio Modulation: The simplest PWM switching strategy is duty ratio modulation (56,60) which produces a load phase voltage of the type shown in Fig. 8.2. This waveform comprises identical pulses evenly spaced within the quasi-square outline (shown dashed in Fig. 8.2). The inverter phase gating information, presented here in the form of the inverter line voltage, which is required to create the load phase

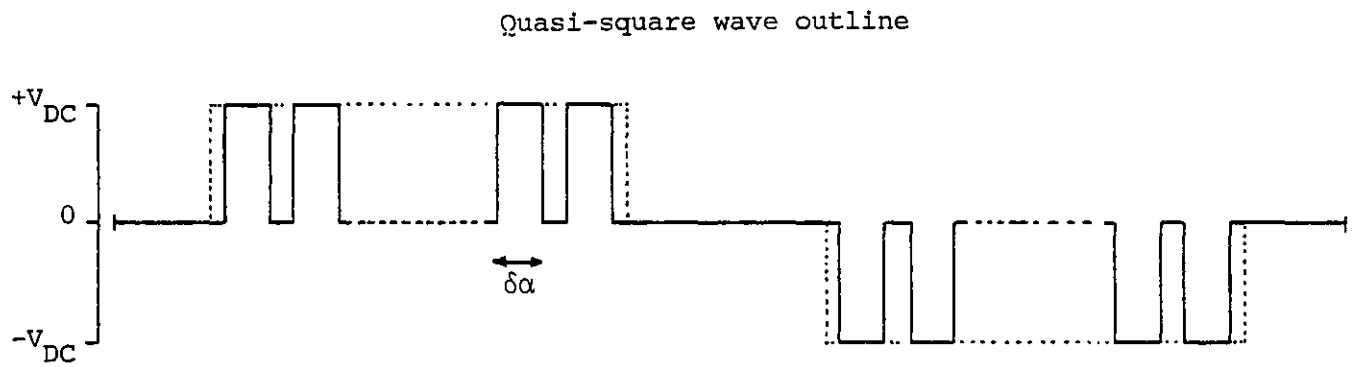


Fig. 8.2 Load phase voltage waveform produced by Duty Ratio Modulation

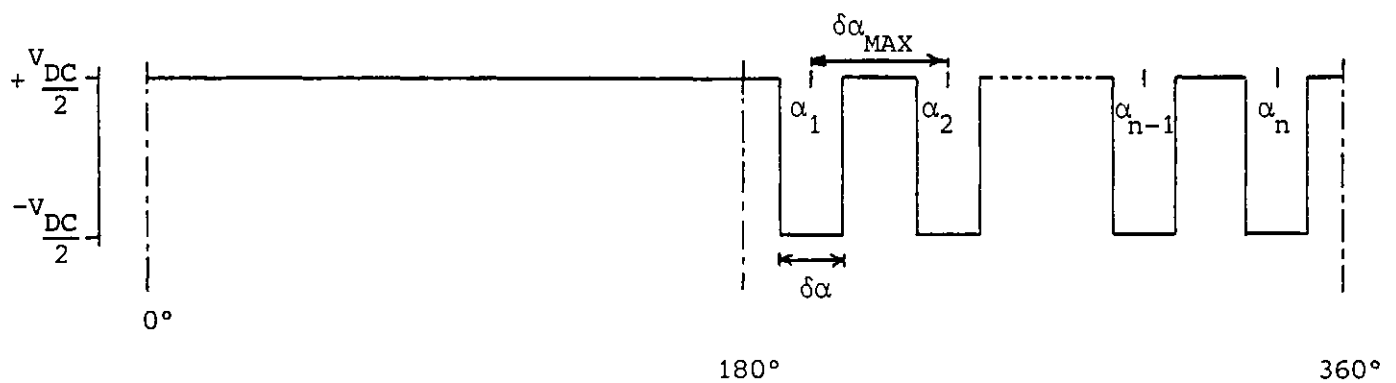


Fig. 8.3 Inverter line voltage produced by Duty Ratio Modulation

voltage is illustrated by a typical example in Fig. 8.3.

The switching angles for the waveform shown in Fig. 8.3 may be calculated directly. The centres of the pulses are given by,

$$\alpha_k = 180 + \left\{ (2k-1) \left[\frac{180}{2n} \right] \right\} \quad k = 1, 2, \dots, n \quad (8.22)$$

where n is the number of pulses per cycle. The width of the pulses is calculated as,

$$\delta\alpha = \left[\frac{\sqrt{2} V_{ph} \pi}{4\sqrt{3} V_{dc}} \right] \left[\frac{180}{n} \right] \quad (8.23)$$

where V_{ph} is the required fundamental rms load phase voltage. $\delta\alpha$ has a maximum value of $\delta\alpha_{MAX} = \left[\frac{180}{n} \right]$.

Major harmonics will be present in the load phase voltage around multiples of the pulse number, n , the largest of which, are at exact multiples of n . Triplen harmonics in an inverter line voltage are not present in the load phase voltage of a three phase system. Therefore, the number of pulses per cycle should be a multiple of three to reduce the harmonic content of the load phase voltage.

8.3.2 Naturally Sampled Modulation: The switching angles for naturally sampled modulation (57) are determined by the intersections of a reference, or modulating, sine wave with a reference, or carrier, wave. This is illustrated by a typical example in Fig. 8.4. The switching angles cannot be calculated directly because of the transcendental nature of the equations defining the two waveforms. Therefore, a numerical solution has to be employed.

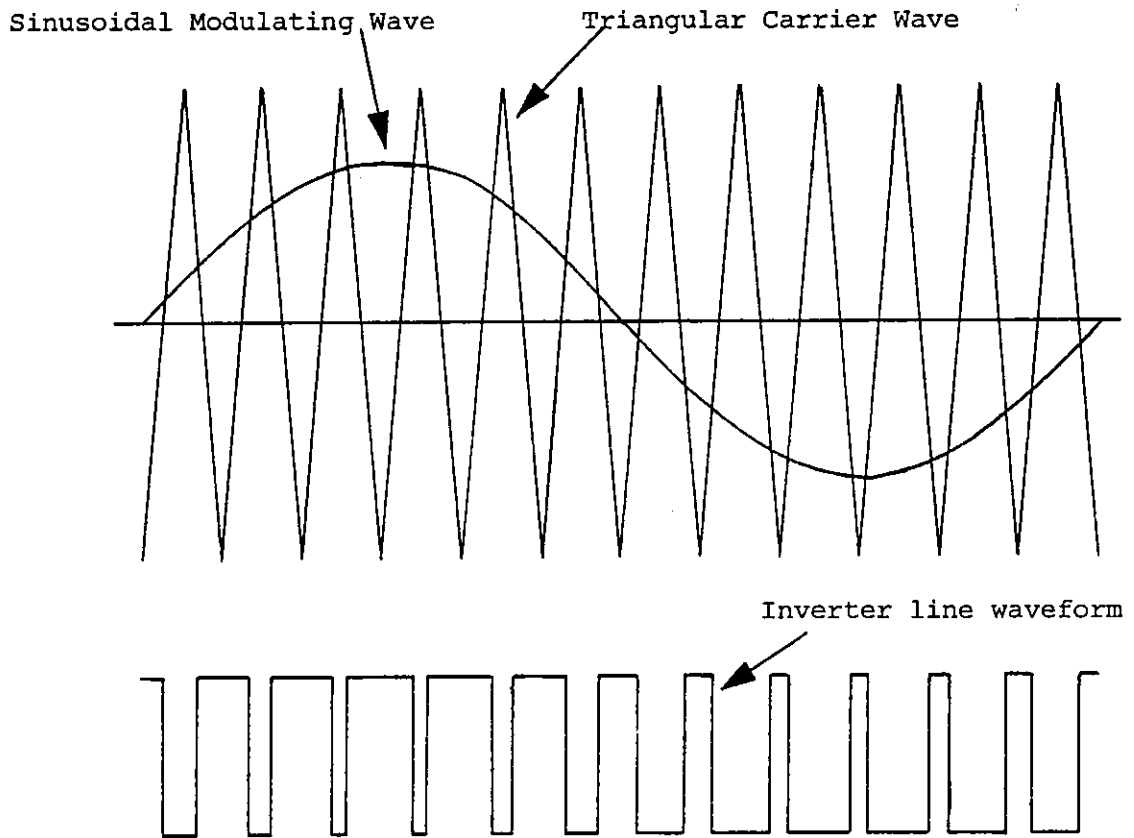


Fig. 8.4 Determination of the line waveform switching angles for Naturally Sampled Modulation

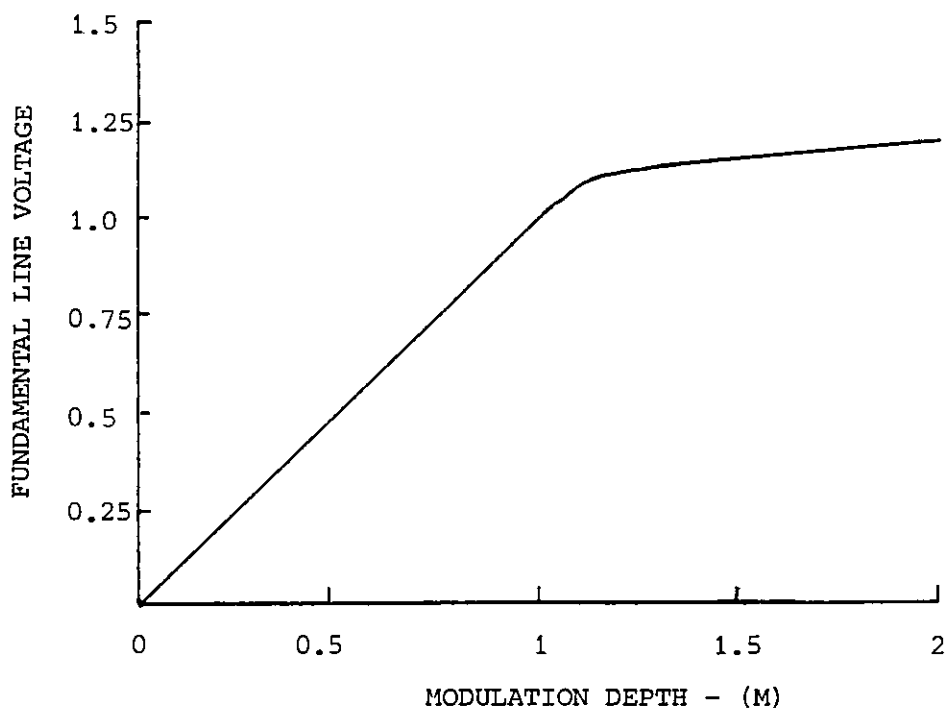


Fig. 8.5 Relationship between fundamental line voltage and modulation depth M

Assuming a triangular wave of unity amplitude, the equation of the modulating sine wave, in terms of the waveform angle ψ , is

$$y = M \sin \psi \quad (8.24)$$

where M is the modulation depth of the sine wave. The triangular wave cannot be described using a single equation and it is most conveniently expressed as a set of equations describing the individual waveform upstrokes and downstrokes. For a frequency ratio R between the carrier and modulating waves, the equation describing the j^{th} upstroke is,

$$y = 1 - 4j + \frac{2R\psi}{\pi} \quad , j = 1, 2 \dots R \quad (8.25)$$

and for the j^{th} downstroke,

$$y = 4j - 3 - \frac{2R\psi}{\pi} \quad , j = 1, 2 \dots R \quad (8.26)$$

The $2R$ inverter line waveform switching angles are given by the solution of,

$$\left. \begin{aligned} M \sin \psi &= 1 - 4j + \frac{2R\psi}{\pi} \\ M \sin \psi &= 4j - 3 - \frac{2R\psi}{\pi} \end{aligned} \right\} j = 1, 2 \dots R \quad (8.27)$$

The above equations may be solved using Newton-Raphson iteration or bisection, over the interval of $(\frac{\pi}{R})$ relevant to the equation being considered. In this study, a NAG Fortran subroutine CO5AAF (65) was used.

Control of the fundamental voltage is achieved by varying the

modulation depth M of the sine wave. The value for M which corresponds to the required inverter line fundamental voltage cannot be calculated directly. An iterative procedure, in conjunction with a characteristic relating fundamental voltage to modulation depth (Fig. 8.5) must be employed.

The frequency ratio R should be a multiple of three to avoid excessive harmonics in the load phase voltage, according to the reasoning in section 8.3.1.

8.3.3 Harmonic Elimination: Patel and Hoft (58), described a PWM switching strategy which eliminates selected harmonics in the load phase voltage. The inverter line voltage, shown as a generalised waveform in Fig. 8.6, is constrained to have quarter and half-wave symmetry, thereby eliminating all even harmonics. Triplens harmonics, although present in the line voltage, do not appear in the phase voltage of the three phase system. Therefore, only harmonics of order $6k \pm 1$ have to be considered.

For $(m+1)$ switching angles per quarter cycle in the inverter line voltage, m harmonics may be eliminated and the fundamental voltage controlled. The generalised waveform (Fig. 8.6) can be represented by a Fourier Series (58),

$$v(\omega t) = \sum_{n=1}^{\infty} a_n \sin(n\omega t) + b_n \cos(n\omega t) \quad (8.28)$$

where

$$a_n = \frac{2V_{dc}}{n\pi} \left[1 + 2 \sum_{k=1}^M (-1)^k \cos(n\alpha_k) \right] \quad (8.29)$$

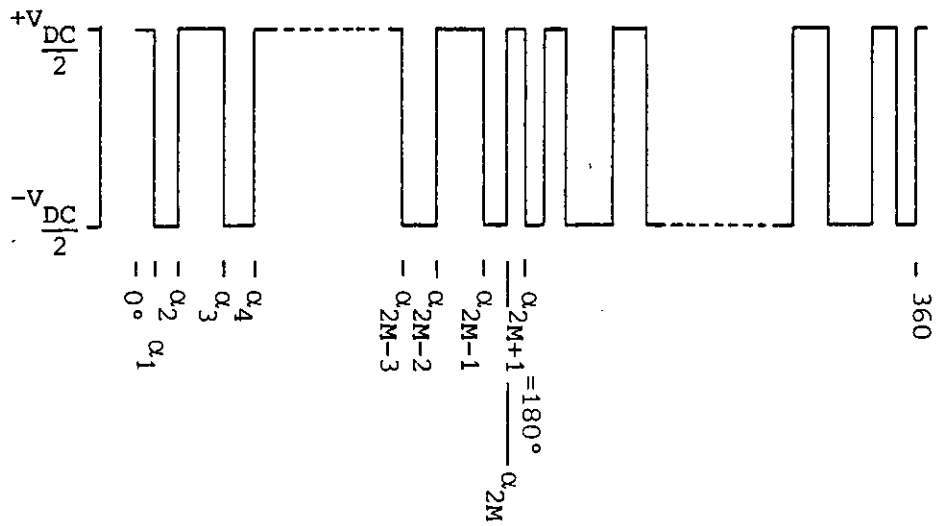


Fig. 8.6 Generalised representation of a 2-level line waveform with 1/4 and 1/2 wave symmetry

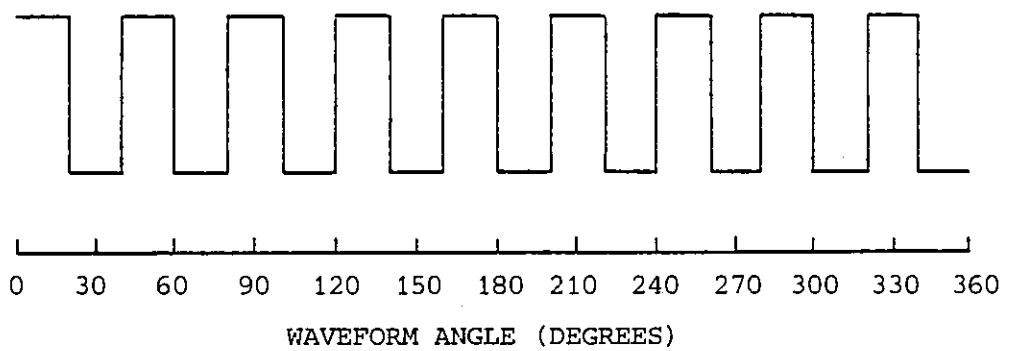


Fig. 8.7 Construction of an inverter line waveform with zero fundamental voltage using a higher frequency waveform

M = number of switching angles per $1/4$ cycle

$b_n = 0$ due to the symmetrical properties of the waveform

The required fundamental rms phase voltage is given by,

$$v_{ph} = \frac{2\sqrt{3} V_{dc}}{\sqrt{2} \pi} \left[1 + 2 \sum_{k=1}^M (-1)^k \cos(\alpha_k) \right] \quad (8.30)$$

The n^{th} harmonic is eliminated by equating a_n to zero, which simplifies from Equation 8.29, to

$$a_n = 1 + 2 \sum_{k=1}^M (-1)^k \cos(n\alpha_k) = 0 \quad (8.31)$$

To eliminate m harmonics ($n_1 \dots n_m$) with fundamental control, the following simultaneous equations have to be solved for the switching angles α :

$$\left. \begin{aligned} f_1(\alpha) &= \frac{2\sqrt{3} V_{dc}}{\sqrt{2} \pi} \left[1 + 2 \sum_{k=1}^{m+1} (-1)^k \cos(\alpha_k) \right] = v_{ph} \\ f_2(\alpha) &= 1 + 2 \sum_{k=1}^{m+1} (-1)^k \cos(n_1 \alpha_k) = 0 \\ &\quad \vdots \\ f_{m+1}(\alpha) &= 1 + 2 \sum_{k=1}^{m+1} (-1)^k \cos(n_m \alpha_k) = 0 \end{aligned} \right\} \quad (8.32)$$

These simultaneous equations are non-linear and transcendental, and are only soluble using numerical techniques. A NAG Fortran subroutine CO5NAF(65) which utilises Powell's hybrid method (66) was used in this study. A Fortran listing of Powell's method may be found in reference 66.

Powell's hybrid method requires an initial guess for the switching

angles to start an iterative procedure combining the Newton and steepest descent methods. Convergence is only guaranteed for initial switching angles which are close to the solution. An incorrect initial guess may cause convergence to a solution which is not physically realisable, for instance, switching angles which lie outside the 0-90° quadrant or angles which do not satisfy

$$0 < \alpha_1 < \alpha_2 < \dots < \alpha_{m+1} < \frac{\pi}{2} \quad (8.33)$$

A procedure for calculating initial angles which guarantee convergence has been developed by Pollmann (67). An inverter line waveform with zero fundamental voltage can be constructed from a number of identical higher frequency waveforms as depicted in Fig. 8.7. If the number of higher frequency waveforms used is a multiple of three, the line voltage will consist solely of triplens harmonics. The (m+1) switching angles describing this construction represent an exact solution for the elimination of m harmonics for a fundamental voltage of zero. The angles for a fundamental voltage, other than zero, are obtained by slowly increasing the fundamental voltage from zero, until the required voltage is reached. The calculated switching angles for one fundamental voltage are used as the initial guess for the next voltage to be considered. In this way, a characteristic of the type shown in Fig. 8.8 may be calculated. The number of possible "zero fundamental" waveform constructions increases with the number of switching angles and because of the transcendental nature of the equations (Equations 8.32) more than one solution may be possible for a particular fundamental voltage. The different solutions obtained will have varying harmonic profiles, therefore a distortion factor which indicates the overall harmonic content of the waveform is calculated. The solution with the lowest distortion factor is adopted.

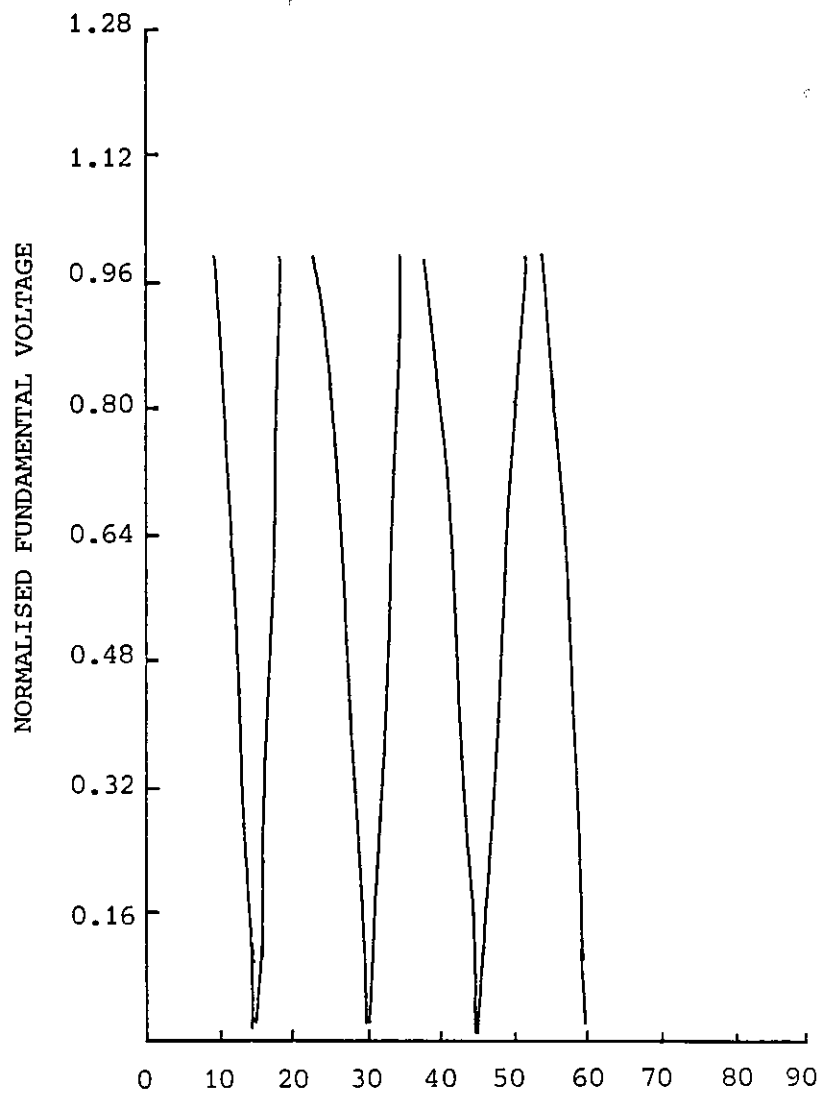


Fig. 8.8 Characteristic relating the inverter line fundamental voltage to the waveform switching angles

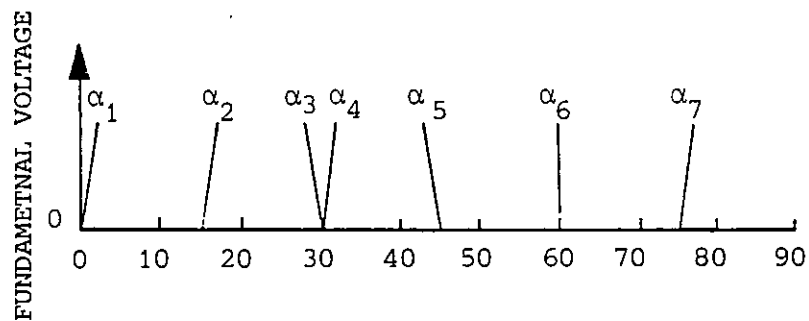


Fig. 8.9 Example of the first "zero fundamental" construction method

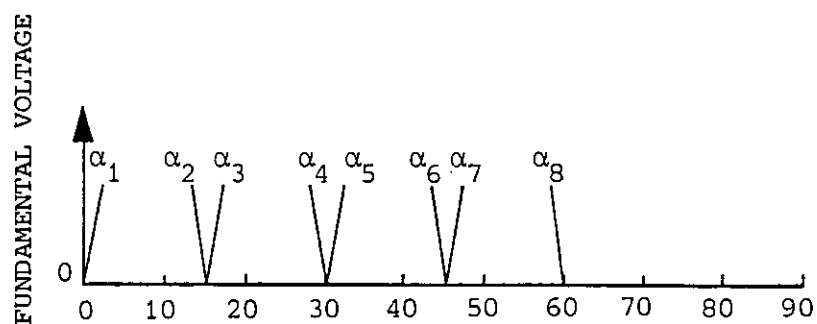


Fig. 8.10 Example of the second "zero fundamental" construction method

The distortion factor σ is ideally given by

$$\sigma = \sum_{n=1}^{\infty} \left(\frac{V_n}{n} \right)^2 \quad (8.34)$$

however in this study it was approximated by

$$\sigma = \sum_{n=1}^{300} \left(\frac{V_n}{n} \right)^2 \quad (8.35)$$

For the comparisons, described in Chapter 5, solutions with the smallest distortion factor were adopted for up to 8 angles per quarter cycle. Above 8 angles the number of possible solutions became impractically large to calculate, therefore, only the two "zero fundamental" constructions described below were used. A more detailed description of the possible constructions is given by Pollmann (67).

Before the construction methods are described, the concept of a "double-point" must be introduced. A "double-point" is a point where two switching angles coincide, i.e. where a pulse of zero width exists. Although this is not a practical proposition, it is a useful assumption when determining the zero fundamental constructions.

The first method of construction has switching angles at $(30-\alpha)$, $(30+\alpha)$, 60 and $(90-\alpha)$ degrees for an even number of switching angles per quarter cycle. For an odd number of angles there is also a switching point at zero degrees. The remaining angles are evenly spaced as "double points" between $(30-\alpha)$ and $(30+\alpha)$. The variable α is given by

$$\alpha = 30 - \left(\frac{60}{k} \right) \quad (8.36)$$

where

$$k = \frac{(M-4)}{2} + 3 \quad \text{for an even number of angles/ } \frac{1}{4} \text{ cycle-M ...} \quad (8.37)$$

$$k = \frac{(M-5)}{2} + 3 \quad \text{for an odd number of angles/ } \frac{1}{4} \text{ cycle-M} \quad (8.38)$$

The second construction method has a switching angle at 60° for an odd number of angles per quarter cycle and also an angle at zero degrees for an even number. The remaining angles are again evenly distributed as "double-points" between 0° and 60°.

Examples of these two constructions are presented in Figs. 8.9 and 8.10 respectively.

8.3.4 Distortion Minimisation

The most commonly referenced minimisation PWM strategy is that proposed by Buja and Indri (59), in which the switching angles are calculated to minimise a distortion factor σ . The distortion factor represents the total harmonic distortion in the inverter line current which is calculated for a purely inductive load as,

$$\sum_{n=1}^{\infty} i_n = \sqrt{\sum_{n=1}^{\infty} \left[\frac{\sqrt{3} \hat{V}_n}{n\omega_0 L} \right]^2} \quad (8.39)$$

The distortion factor σ , to be minimised, is obtained by simplifying Equation 8.39,

$$\sigma = \sqrt{\sum_{n=1}^{\infty} \left(\frac{\hat{V}_n}{n} \right)^2} \quad (8.40)$$

The switching angles are again restrained to the first quarter cycle of a waveform with quarter and half wave symmetry (see section 8.3.3 and Fig. 8.6). Equation 8.40 can be calculated exactly by numerically evaluating Equation 20 in reference 59, where

$$\sigma = \frac{2}{V_{dc}} \sqrt{\frac{1}{2\pi} \int_{[2\pi]} \left\{ \int_{\pi/3}^{\alpha} \left[v(\alpha) - v\left(\alpha - \frac{2\pi}{3}\right) \right] d\alpha \right\}^2 d\alpha - \frac{2V_1^2}{V_{dc}^2}} \quad (8.41)$$

The minimisation of Equation 8.41 has to be constrained according to:

equality constraints : $V_1 = \text{required line voltage}$

inequality constraints: $\alpha_n > \alpha_{n-1} ; n = 2, M$

range constraint : $0 < \alpha_n < 90 ; n = 1, M$

The constrained minimisation of Equation 8.41 was attempted using a number of minimisation algorithms, particularly those in the NAG library (65), but difficulties were encountered with convergence of the solution. This problem could not be overcome and so an alternative approach was adopted.

Equation 8.40 is expressed as an infinite sum of squares, which may be approximated by a finite series

$$\sigma' = \sqrt{\sum_{n=1}^{241} \left(\frac{\hat{V}_n}{n} \right)^2} \quad (8.42)$$

The 241st harmonic was chosen as the upper limit because of computation time considerations. The harmonic voltages \hat{V}_n are calculated using the method described in section 8.1. Because the distortion factor σ' is

expressed as a sum of squares, it may be minimised using a specialised routine, such as the NAG subroutine E04FCF used in this study. The constraints were achieved by including extra terms to those in Equation 8.42.

The equality constraint was considered by inclusion of the term,

$$g_1 = \left[\frac{V_1(\text{required})}{V_1(\text{calculated})} \right] - 1 \quad (8.43)$$

which will tend to zero as the calculated fundamental voltage approaches the required value.

The inequality constraints were enhanced by inclusion of the criterion of minimum pulse width, α_{\min} (section 4.4). The inequality constraints become,

$$\alpha_n > \alpha_{n-1} + \alpha_{\min} \quad (8.44)$$

A set of $M+1$ terms were therefore included as follows:

$$\left. \begin{aligned} f_n &= 0 && \text{if } \alpha_n - \alpha_{n-1} \geq \alpha_{\min} \\ &= \left[\frac{\alpha_{n-1} + \alpha_{\min}}{\alpha_n} \right] - 1 && \text{if } \alpha_n - \alpha_{n-1} < \alpha_{\min} \end{aligned} \right\} \quad (8.45)$$

for $n = 2, 3 \dots M$

f_1 and f_{M+1} are treated as special cases because of the waveform symmetry about 0 and 90 degrees. where the minimum pulse width between α_1 and 0° , and α_M and 90° , is $\left[\frac{\alpha_{\min}}{2} \right]$

$$\left. \begin{aligned} f_1 &= 0 && \text{if } \alpha_1 \geq (\alpha_{\min}/2) \\ &= \frac{(\alpha_{\min}/2)}{\alpha_1} - 1 && \text{if } \alpha_1 < (\alpha_{\min}/2) \end{aligned} \right\} \quad (8.46)$$

$$\left. \begin{aligned} f_{M+1} &= 0 && \text{if } 90-\alpha_M \geq (\alpha_{\min}/2) \\ &= \frac{(\alpha_{\min}/2)+\alpha_M}{90} && \text{if } 90-\alpha_M < (\alpha_{\min}/2) \end{aligned} \right\} \quad (8.47)$$

The range constraint was implemented by forcing the switching angles to lie between 0 and 90 degrees. Problems were encountered with this because the angles dealt with, by the NAG subroutine, could not be varied. Therefore, the angles calculated by the NAG subroutine were left unchanged, however the distortion factor σ' , and the constraints, were calculated using angles which were transformed to lie within the specified range.

To summarise, the terms considered in the sum of squares minimisation were

$$\begin{aligned} &\text{minimise } \sum_{j=1}^{82+M} (X_j)^2 \quad \text{where} \\ X_1 \text{ to } X_{80} &= \left[\frac{\hat{v}_n}{n} \right] \quad \text{for } n = 6k \pm 1, k = 1, 40 \\ X_{81} &= g_1 \\ X_{82} \text{ to } X_{82+M} &= f_k \quad \text{for } k = 1, M+1 \end{aligned}$$

Using NAG routine E04FCF, the sum of squares minimisation converged rapidly and reliably. The object of the minimisation procedure is to calculate the switching angles which yield the global minimum of the

distortion factor. However, because of the transcendental nature of the terms, there may be many minima. The initial guess for the switching angles dictates which local minimum is considered, and because there is not mathematical means of detecting a global minimum, an engineering solution has to be adopted. A series of initial guesses, described below, were used to calculate a series of local minima, the smallest of these representing the global minimum. This method is subject to error in that a global minimum may be missed, however in the author's opinion it represents the only practical solution to the problem.

The series of initial angles were chosen to cover all possible angle figurations. Initially, the switching angles are assumed to lie close to zero degrees, being evenly spaced by 2 degrees. A series of ten guesses are generated by moving the largest angle towards 90 degrees, the remaining angles being evenly spaced between zero and the largest angle. At this point the switching angles are evenly spread across the 90 degree range. A further 10 initial guesses are generated, in a similar manner, by advancing the least angle towards the largest angle (which lies at approximately 90 degrees) until the angles all lie close to 90 degrees.

A second series of switching angles is generated by firstly positioning the angles close to zero, and from there, moving the angles one at a time from the zero region to the region close to 90 degrees until the angles all lie close to 90 degrees.

8.4 Simulating the 30 kW Drive

In section 5.3.2 PWM switching strategies were compared for a 30 kW inverter/induction motor drive. The principle of system simulation is identical to that discussed in Chapters 2 to 4. However, the inverter

and motor models are discussed briefly, with differences between the 4 kW and 30 kW models being indicated.

8.4.1 Simulating the 30 kW Inverter: The 30 kW inverter has exactly the same circuit configuration as the 4 kW inverter discussed in Chapter 2, the only difference being that the circuit component values are different. These values, given in Table 8.1, were used to calculate a curve, of the type shown in Fig. 2.16, relating energy lost during commutation to the current commutated. The curve for the 30 kW inverter is shown in Fig. 8.11. No experimental verification was undertaken for the 30 kW inverter model.

8.4.2 Simulating the 30 kW Induction Motor: There are several differences between the 4 kW and 30 kW motor models which arise mainly because the 30 kW motor has open rotor slots, whereas the rotor slots in the 4 kW motor were closed. The 30 kW motor is a delta-connected, double layer, 10 pole, cage induction motor, the cage being constructed using copper bars. Details of the motor are given in Table 8.2. Calculation of the motor equivalent circuit parameters are identical to the methods presented in section 3.3, except for the rotor resistance and rotor leakage inductance. No saturation effects were present in the 30 kW motor.

8.4.2(i) Calculation of Rotor Resistance and Rotor Leakage Inductance:

The rotor slots in the 30 kW motor are open, therefore, calculation of the rotor slot bridge inductance is no longer applicable. Deep-bar effect, which was neglected in sections 3.3.6 and 3.3.7, must be included for this motor. The rotor resistance is calculated, as in Equation 3.21.

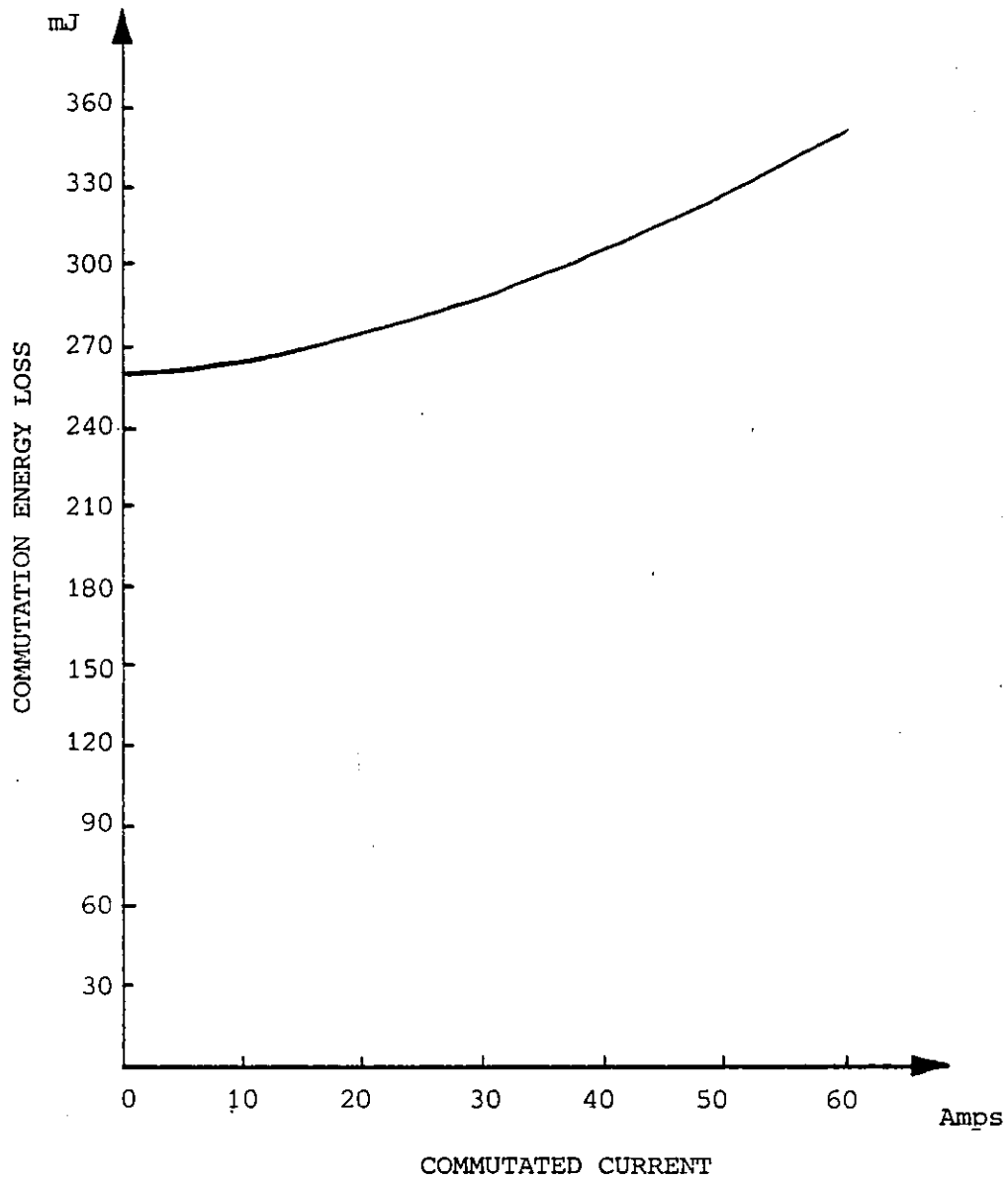


Fig. 8.11 Calculated characteristic relating commutation energy loss to the current being commutated, for the 30 kW Inverter

$$\left. \begin{array}{l} V_{TM} \\ V_{TA} \end{array} \right\} = 1.733 \text{ V}$$

$$\left. \begin{array}{l} V_{D1} \\ V_{D2} \\ V_{DF} \\ V_{DD} \end{array} \right\} = 0.82 \text{ V}$$

$$\left. \begin{array}{l} R_{TM} \\ R_{TA} \end{array} \right\} = 6.67 \times 10^{-3} \Omega$$

$$\left. \begin{array}{l} R_{D1} \\ R_{D2} \\ R_{DF} \\ R_{DD} \end{array} \right\} = 9.5 \times 10^{-3} \Omega$$

$$C = 13 \mu\text{F}$$

$$L_L = 36 \mu\text{F}$$

$$R_L = 0.03 \Omega$$

$$R_D = 5.6 \Omega$$

$$\left. \begin{array}{l} C_{SM} \\ C_{SA} \end{array} \right\} = 100 \text{ nF}$$

$$V_E = 810 \text{ V}$$

Table 8.1 Component values for the 30 kW inverter

Operating Line voltage	810 V
Rated Torque	500 Nm
No. of Poles	10
No. of Stator Slots	90
No. of Rotor Slots	80
No. of Turns/Phase	270
Stator Slot Mouth Width	2.79 mm
Stator Slot Constant	2.74
Rotor Slot Mouth Width	1.52 mm
Rotor Slot Depth	10.67 mm
Rotor Slot Constant	1.24
Resistivity of Rotor Bar	$1.77 \times 10^{-8} \Omega\text{-m}$
Rotor Skew (as a fraction of a rotor slot pitch)	0.889
Effective Machine Length	0.1994 m
Carter Corrected Airgap Length	0.65 mm
Mean Diameter of Airgap	298 mm

Table 8.2 Summary of 30 kW motor parameters

$$R_2 = R_{\text{bar}}^{\phi} + R_{\text{ring}} \quad (8.48)$$

and the rotor leakage inductance is given by

$$L_2 = L_{\text{SLOT}}^{\psi} + L_{2\text{DIFF}} \quad (8.49)$$

where $L_{2\text{DIFF}}$ is the rotor differential leakage inductance calculated as (55)

$$L_{2\text{DIFF}} = \frac{\mu_0 w' \pi d}{4g' N_R} \left\{ \text{cosec}^2 \left(\frac{p\pi}{N_R} \right) - \left(\frac{N_R}{p\pi} \right)^2 - \frac{2b_r}{3\lambda_r} \right\} \quad (8.50)$$

The variables ϕ and ψ are the relevant deep bar corrections given by Liwschitz-Garik, (68)

$$\phi = \frac{\delta}{2} \left[\frac{\sinh \delta + \sin \delta}{\cosh \delta - \cos \delta} \right] \quad (8.51)$$

$$\psi = \frac{3}{\delta} \left[\frac{\sinh \delta - \sin \delta}{\cosh \delta - \cos \delta} \right] \quad (8.52)$$

in which,

$$\delta = 1.975 \times 10^{-3} d \sqrt{\frac{f_{sn}}{\rho_b}} \sqrt{s_n} \quad (8.53)$$

where d = rotor slot depth (m)
 $f_{sn} = n^{\text{th}}$ time harmonic frequency (Hz)
 ρ_b = rotor bar resistivity ($\Omega\text{-m}$)
 $s_n = n^{\text{th}}$ harmonic slip

The equivalent circuit parameters calculated for the 30 kW motor are presented in Table 8.3. The method of utilising the equivalent circuit is similar to that for the 4 kW motor except that

- a) no iterative loops have to be executed to determine the magnetising, and rotor slot bridge leakage, inductances
- b) the rotor resistance and rotor leakage inductance must be calculated for each harmonic equivalent circuit because of the deep-bar effect.

The motor model was verified experimentally as part of another research project (69), and for brevity the results are not repeated here.

Stator Resistance, R_1	1.467 Ω
Stator Leakage Inductance, L_1	12.47 mH
Magnetising Inductance, L_m	294.7 mH
Rotor Slot Leakage Inductance, $L_{2\text{SLOT}}$	3.1071×10^{-7} H
Rotor Differential Leakage Inductance, $L_{2\text{DIFF}}$	2.8119×10^{-7} H
Rotor Bar Resistance, R_{bar}	1.066×10^{-4} Ω
Rotor End Ring Resistance, R_{ring}	3.89×10^{-5} Ω
Skew Leakage Inductance, L_{SKEW}	3.01 mH
Skew Factor, k_{SK}	0.9949
Equivalent Circuit Transformer Ratio, k_{WT}	10073.5

Table 8.3 Equivalent circuit parameters for the 30 kW motor